Novel Planar Microstrip and Dielectric Resonator Filters

by

Rui Zhang

A thesis
presented to the University of Waterloo
in fulfillment of the
thesis requirement for the degree of
Doctor of Philosophy
in
Electrical and Computer Engineering

Waterloo, Ontario, Canada, 2007

Author's Declaration

I hereby declare that I am the sole author of this thesis. This is a true copy of the thesis, including any required final revisions, as accepted by my examiners.

I understand that my thesis may be made electronically available to the public.

Abstract

Microwave filters possessing various forms are essential components in radar, satellite, and mobile communication systems. Increased demands for low-loss, miniature filters that can be mass produced at low cost have provided a significant challenge reinforcing the need for improving or even replacing the conventional microwave filters.

In recent years, the concept of Photonic/Electromagnetic Bandgap (PBG/EBG) structures has attracted the attention of the microwave engineering community. The main feature of PBG/EBG structures is the existence of a bandgap in the frequency spectrum of a propagating photonic/electromagnetic wave. The motivation for adopting EBG structures stems from their capability to eliminate unwanted wave propagations in various microwave devices.

This thesis investigates and proposes novel planar microstrip filters employing EBG structures in the form of slots etched on the ground plane. Such filters are not only compact, but also can improve the RF performance in both the passband and the stopband. This proposed concept is further extended to implement low-loss tunable lowpass filters, both digital and analogue, by integrating tuning elements directly into the slots. Transmission line circuit models are developed to design the proposed microstrip filters and tunable lowpass filters. To verify the concept and the validity of the developed circuit models, theoretical and experimental results are presented and carefully compared.

Currently, dielectric resonator (DR) filters have been widely employed in wireless and satellite communication systems. Over the past two decades, tremendous progress has been made to reduce the size, and enhance the in-band and out-of-band performance of DR filters. However, the current approaches for implementing DR filters are relatively expensive and hardly amenable to mass production. Cost reduction remains a key limiting factor that needs to be addressed now.

A new configuration of DR filters is presented in this thesis. The novel concept simplifies the assembly, integration, and alignment of DR filters, significantly reducing production time and costs. Not only is the design of the proposed multi-pole DR filters and diplexers examined, but also the fabrication technique. The experimental measurement results confirm the validity of the theoretical designs of the new filters, which makes this concept very attractive for further applications in both wireless and satellite communication.

Acknowledgements

After finishing writing the thesis, it is time now to thank all the people who have helped so much in the past, which makes this thesis possible and enjoyable for me.

First of all, I wish to express my sincere gratitude to my research supervisor, Professor Raafat R. Mansour, for providing me such a great opportunity to work with him. I couldn't thank him enough for his knowledgeable guidance, valuable suggestions and continuous encouragement throughout my Ph.D. study. His tremendous help is always around whenever I need. I am deeply grateful to the efforts, patience and enthusiasm that he shared with me along this entire process.

I would also like to thank all my committee members, Professor Abbas S. Omar, Professor Sujeet K. Chaudhuri, Professor Safieddin Safavi-Naeini, Professor Chris O'Donovan, and Professor Ming Yu, not only for reviewing the thesis but more importantly for their constructive criticisms and advices on the project through the years.

Many thanks shall be paid to all members of the CIRFE group at the University of Waterloo for their kindness and support. I am particularly in debt to Bill Jolley for his assist with filter assembly and measurement, to Louise Green for taking care of all the trivial matters, and to my officemates, Dong Yan and Mojgan Daneshmand, for their helpful discussions and suggestions.

I would like to thank the essential financial supports for my research project and living stipend from COM DEV and the University of Waterloo.

I am really thankful to my two former supervisors, Professor Da-Gang Fang and Professor Ke-Li Wu, for bringing me into the wonderful world of electromagnetics and making my study at Waterloo possible.

Last but not least, I am so grateful to my parents and brother back in China, for their love, understanding and support during my whole life, especially when I am thousands miles away from them for the last five years. Finally, my sincere gratefulness goes to my dearest friend, Mr. Nan Chen, who was so helpful in every single aspect of my life at waterloo, from small things such as proofreading word by word of all my publications and thesis, to big things including taking care of me whole heartedly.

Table of Contents

List of Figures

List of Tables

Chapter 1

Introduction

1.1 Motivation

Recently, the concept of Photonic/Electromagnetic Bandgap (PBG/EBG) structures has intrigued the microwave engineering community. For example, microstrip lines incorporating EBG structures on the ground plane, called microstrip EBG structures, have been proven to exhibit passband-stopband filter characteristics and a slow wave effect. These features have been used in bandstop or lowpass filter applications to eliminate unwanted frequencies and to miniaturize microstrip filter circuits.

However, there are still some problems in utilizing such structures. One of them is the conflict between the passband and the stopband characteristics in conventional EBG-based microstrip filters. An improved stopband performance can be achieved only at the expense of the passband performance and vice versa. Obviously, there is a need to find solutions that can lead to a better filter performance in both the passband and the stopband. To achieve such, this thesis explores the use of novel EBG structures with slots etched on the ground plane for the realization of miniature microstrip bandstop, lowpass and bandpass filters.

High performance RF tunable filters are needed in reconfigurable systems to facilitate the efficient utilization of the available frequency spectrum. Specially, they are in demand in

front-end receivers for the suppression of interference signals and the relaxation of oscillator phase noise and dynamic range requirements. Most of the work reported in the literature has focused on tunable bandpass filters, whose insertion loss is determined by the quality factor (Q) of the filter itself and the Q of the tuning element, whether it is a semiconductor, ferroelectric, ferromagnetic (YIG, ferrite) or Micro-Electro-Mechanical Systems (MEMS) device. Despite their relatively low insertion loss, YIG tunable filters are bulky. Also, there are semiconductor or MEMS tuning elements that are amenable to integration with planar resonators for the realization of miniature tunable bandpass filters. However, even with the use of high-Q MEMS tuning elements, the Q of this type of filter is limited by the Q of the planar resonators.

Tunable lowpass filters are useful in applications that require the suppression of out-of-band interference signals. The thesis proposes the integration of MEMS switches and semiconductor varactors in the slots etched on the ground plane to create digital and analogue tunable lowpass filters. The advantages are convincing: the ease of integration and application of a DC bias voltage, and a low-loss performance.

Due to their superior characteristics of a high Q and miniaturization, dielectric resonator (DR) filters are the most preferred design among all known types of filters. However, the demands have increased for low-loss DR filters that are compact, and capable of being manufactured in a large quantity at a reasonably low cost. Particularly in wireless communication applications, there is a need to find a solution to replace low-cost coaxial filters which exhibit only a low Q with low-cost DR filters that offer a high Q. The thesis describes the realization of the novel low-cost DR filters and diplexers fabricated by using high-dielectric-constant ceramic substrates.

The thesis is built around three objectives.

1) To develop EBG-based miniature microstrip bandstop, lowpass and bandpass filters with an improved passband and stopband performance.

2) To develop EBG-based tunable lowpass filters with a low loss, wide tuning range, and compact size with both digital and analogue tuning capability.

3) To develop low-cost DR filters and diplexers implemented from high-K ceramic substrates, with a simplified assembly and integration.

1.2 Organization of the Thesis

Following this introduction, Chapter 2 provides a review of various EBG-based microstrip filters, DR filters and multiplexers, emphasizing their design and fabrication.

In Chapter 3, several novel planar microstrip filters with EBG structures in the form of slots etched on the ground plane are presented. Various slot configurations have been studied, and transmission line circuit models are developed and utilized in filter designs. The proposed EBG-based microstrip filters with compact size and superior RF performance include bandstop filters, lowpass filters and bandpass filters. The application of EBG-based lowpass filters in the suppression of spurious modes is also demonstrated.

Chapter 4 extends the concept of etching slots on the ground plane to implement low-loss tunable lowpass filters by integrating tuning elements into the slots of the EBG-based microstrip lowpass filters developed in Chapter 3. MEMS switches are used on the slots to realize digital tunable lowpass filters. An analogue tunability is achieved by assembling semiconductor varactors into the slots. The transmission line circuit models are employed in all the designs. The RF performance and the tuning ability of the tunable lowpass filters are presented by both simulated and measured data. Moreover, the realization of an ultra-wideband tunable lowpass filter, by combining MEMS switches and varactors, is proposed.

In Chapter 5, a novel DR configuration is proposed. Several DR filters using the proposed DR configuration are designed and demonstrated. The spurious performance of the DR filters is investigated and improved by further modifying the filter designs. A unique triplet structure, based on the proposed concept, is introduced to provide a new approach to

implement nonadjacent couplings for the realization of asymmetric filtering characteristics. After the fabrication technique and measured performance are presented, the concept of the new DR configuration has been extended to implement diplexers.

Lastly, a brief summary of the contributions regarding the presented work and suggestions for future research work conclude the thesis.

Chapter 2

Background Information

2.1 Introduction

EBG structures are periodic dielectric or metallic structures that can effectively prevent the propagation of electromagnetic waves in certain directions at certain frequencies. The idea is to localize an electromagnetic wave by the presence of periodically positioned scatterings, whose periodicity is almost or equal to a particular wavelength so that the electromagnetic wave with the frequency within the bandgap is stuck inside the material without any further propagation. There are various shapes and forms of EBG structures, reported in the literature [1, 2]. A summary of the reported work on microstrip EBG structures in the area of micro/millimetre-waves is first given, followed by a brief review of tunable lowpass filters.

Another research topic related to this thesis is DR filters/diplexers/multiplexers. DR filters have been widely used in communication systems due to their superior characteristics of a high Q, low loss, and miniaturization. Different types of conventional DR filters that are currently used in mobiles and satellites are introduced in the following sections. DR diplexers/multiplexers that are realized by combining several DR filters with a multi-port junction, are also discussed. It is hoped that a clear and current understanding of the progress

of studies on EBG structures and DR filters is achieved with the review, to guide and evaluate the investigation described in this thesis.

2.2 Microstrip EBG Structures

Microstrip EBG structures are microstrip devices, incorporating periodic structures either on the substrate or on the ground plane.

2.2.1 EBG Structures from Periodic Dielectric Substrate Drilling

Among the proposed and demonstrated EBG structures, is a periodic array of dielectric inclusions with a dielectric constant different from that of the host dielectric substrate (e.g., an array of air holes drilled through a dielectric substrate [3, 4]), as displayed in Fig. 2.1. This type of EBG structures requires the painstaking work of drilling through the substrate. In addition, this EBG structure is not easy to model and analyze.

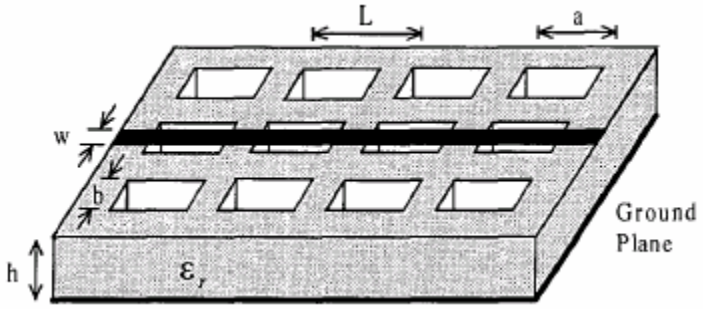

Fig. 2.1 EBG structure from periodic dielectric substrate drilling [4].

2.2.2 EBG Structures from Periodic Ground Plane Etching

Another method is developed to implement EBG structures by etching periodic patterns on the ground plane as shown in Fig. 2.2 (a) [5]. Such EBG structures have the advantages of low cost and easy fabrication, since they are compatible with standard planar circuit technology for microwave/millimetre-wave applications.

Microstrip transmission lines incorporating EBG structures, exhibit the passband-stopband characteristic, depicted in Fig. 2.2 (b). This feature provides an effective method to reject unwanted frequencies and to reduce the physical size of the microstrip circuits. Several variations of this structure have been reported in the literature [6-8]. The majority consist of a two-dimensional periodic array of holes etched on the ground plane. The holes vary in shape from simple rectangular or circular shapes to more complicated shapes. In addition, the arrangement of the holes varies from square-lattice or triangle-lattice to other possible lattices. Also, the shape and size of these holes have a considerable impact on the passband and stopband characteristics of the microstrip EBG structures.

It can be seen from Fig. 2.2 (b) that the microstrip EBG structure exhibits a lowpass characteristic with a stopband whose centre frequency is determined by the periodicity of the EBG lattice. Since the periodicity must be a half-wavelength at the stopband frequency, the applications of this structure are limited because of its relatively large size.

2.2.3 Uniplanar-Compact EBG Structures

Over the past few years, several papers have been published on the development of compact EBG structures. Yang et al. have proposed a compact EBG structure, namely, the Uniplanar-Compact (UC)-EBG structures [9]. It consists of a two-dimensional square pattern. Each element consists of a metal pad and four connecting narrow branches to form a distributed *LC* network, as illustrated in Fig. 2.3. Due to the slow-wave effect generated by this unique structure, the periodicity of the EBG lattice is only $0.1\lambda_0$ at the stopband frequency, resulting in a considerably compact structure [9]. This UC-EBG structure can be

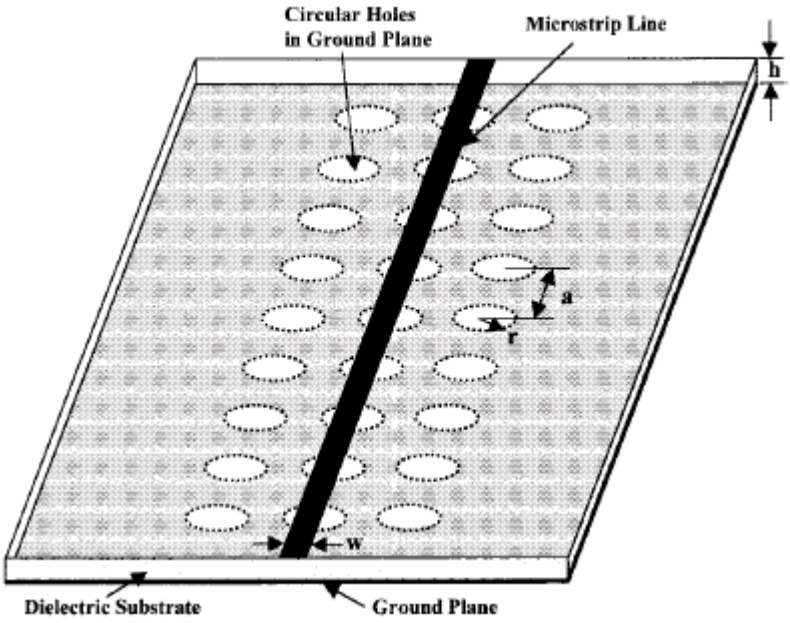

(a)

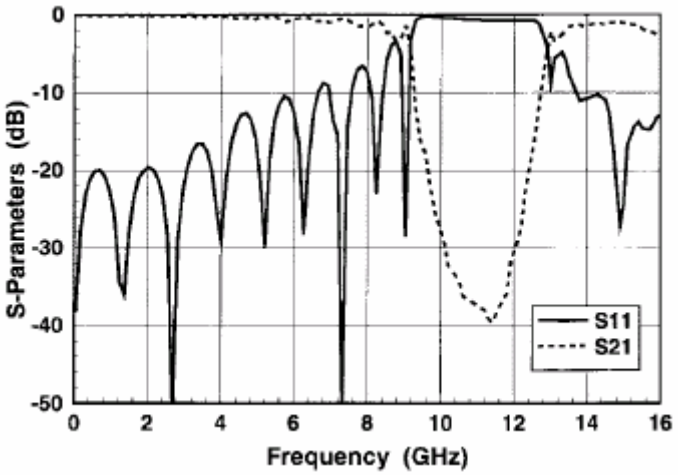

(b)

Fig. 2.2 EBG structure from periodic ground plane etching [5]: (a) configuration and (b) frequency responses.

built by implementing standard planar fabrication techniques without any modifications. The virtues of moderate impedance, low-loss, and uniplanar features make the UC-EBG structure a very promising candidate as a slow-wave transmission line.

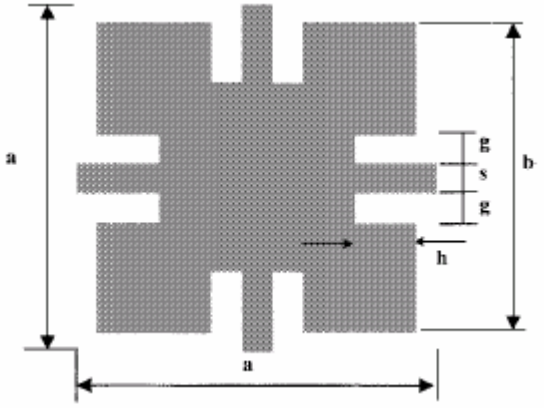

Fig. 2.3 UC-EBG element [9].

Most microstrip filters exhibit higher order harmonics as spurious passbands, which tend to deteriorate the performance of the overall RF system. Often, extra filters are required to suppress the spurious modes, and as a result, the insertion loss is increased in the passband. Compact microstrip filters with intrinsic spurious rejection can be constructed by employing the UC-EBG structure [9]. The wide and deep stopband, generated by the UC-EBG structure is applied to suppress the spurious passbands at higher harmonics. Extra filters are not required since the stopband is intrinsic. Furthermore, the slow-wave effect reduces the physical length of the filter. Fig. 2.4 shows the schematic of a compact parallel-coupled microstrip filter, where the UC-EBG structure is on the ground plane. Fig. 2.5 denotes the measured results of the compact parallel-coupled bandpass filter on a UC-EBG substrate. For comparison, the RF performance of a conventional microstrip bandpass filter is also plotted. As seen, the isolations of the conventional filter are -10dB and -5dB at 12GHz and 17GHz, respectively, whereas the filter on a UC-EBG ground exibits a 30-40dB suppression of the spurious transmissions.

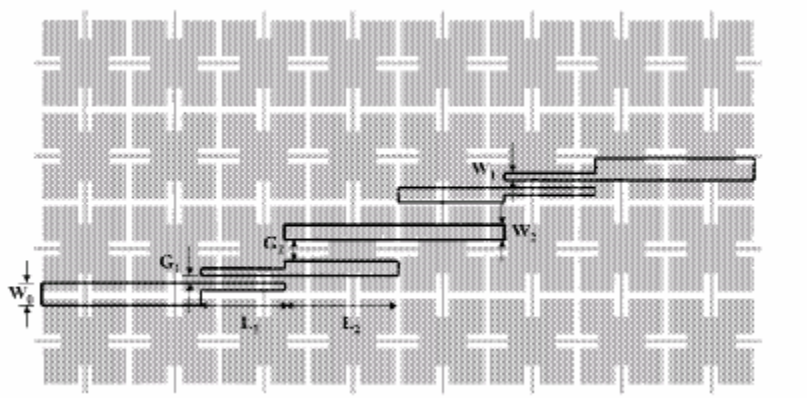

Fig. 2.4 Compact parallel-coupled BPF on the UC-EBG substrate [9].

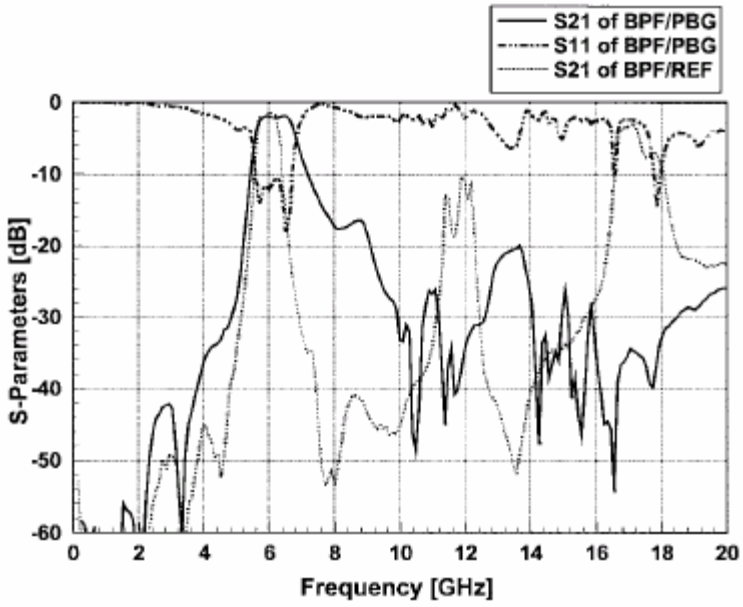

Fig. 2.5 Measured *S*-parameters of the fabricated EBG-based bandpass filter; S_{21} of the same bandpass filter without EBG structures is shown for comparison [9].

2.2.4 Multilayer EBG Structures

To construct a multilayer EBG structure, EBG patterns etched on the ground plane of a single layer uniplanar circuit are stacked, resulting in much wider stopbands than those of the monolayer UC-EBG. Caloz et al. have introduced a novel two-layer biperiodic PBG microstrip structure of stacked UC-EBG plates with different periodicities [10]. Fig. 2.6 provides a schematic of a two-layer EBG structure. The two layers results in a configuration with an effective periodicity of $2a$, leading to the realization of a compact EBG structure.

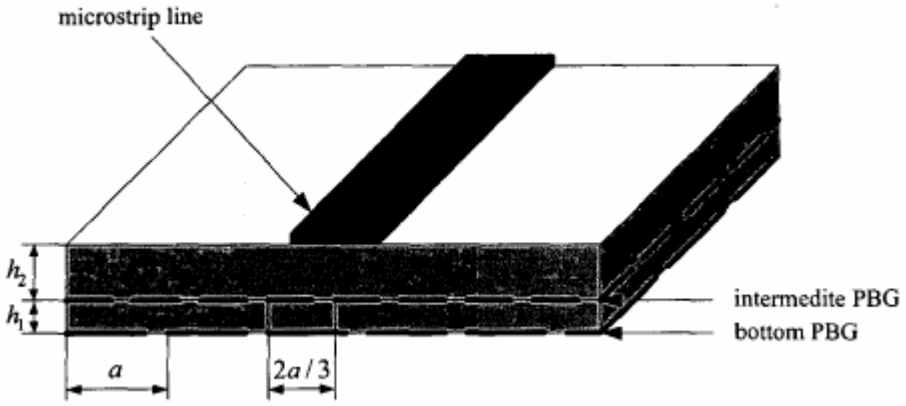

Fig. 2.6 Schematic of the two-layer EBG structure [10].

2.2.5 Defected Ground Structures

Many passive and active microwave and millimetre-wave devices with EBG structures have been developed to eliminate the higher harmonics and to achieve circuit miniaturization. Due to the complexity of the modeling, it is not easy to incorporate EBG structures into the design of the microwave and millimetre-wave components. There are too many design parameters, affecting the properties of the bandgap, including the number of lattices, lattice shapes, lattice spacing, pattern shapes and pattern sizes.

Investigations on the Defected Ground Structure (DGS) have been reported with various configurations in microwave/millimetre-wave frequency-band applications. The DGSs with periodic or nonperiodic patterns provide a rejection band in certain frequency ranges due to the increment of the effective inductance of a transmission line. This rejection property of the DGSs can be employed in many circuits such as planar antennas, filters, power-amplifiers and power dividers [11-14]. A new DGS, integrated with a microstrip line, has been proposed by Kim et al. [15]. The proposed DGS unit in Fig. 2.7 provides the stopband property in some frequency bands with one or more unit lattices.

The disturbance of the current distribution on the ground plane, caused by the etched defect, changes the characteristics of a transmission line in line capacitance and inductance. The proposed DGS which includes narrow and widely etched areas on the metallic ground plane increases the effective capacitance and inductance of a transmission line. The use of DGSs in lowpass filter designs allows the realization of high impedance inductance with a relatively large conductor width. This, in turn, helps to improve the power handling capability of the lowpass filter [11].

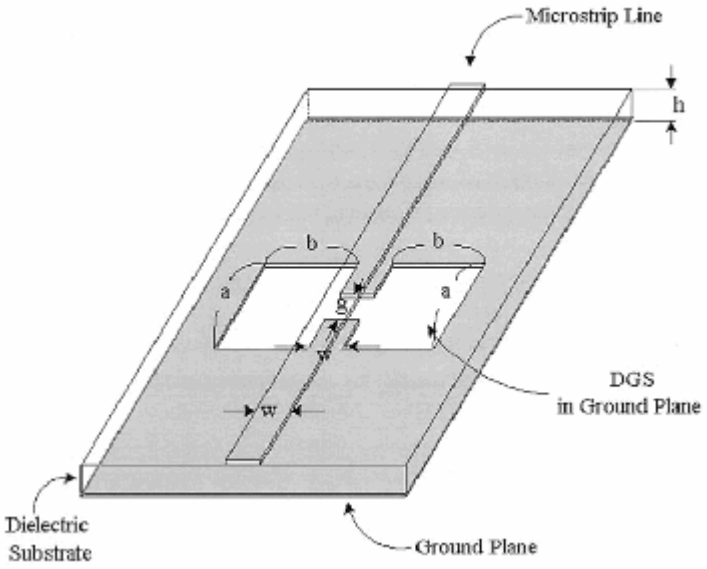

Fig. 2.7 3-D view of the DGS unit section [15].

Zhu et al. have exploited a DGS, by etching rectangular apertures on the ground plane of a Parallel-Coupled Microstrip Line (PCML) for the effective enhancement of a tight frequency-dependent coupling [16]. The concept can be applied to design a compact wideband microstrip bandpass filter such as the one in Fig. 2.8.

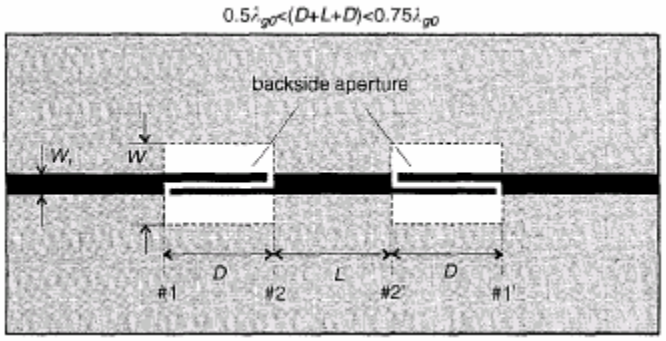

Fig. 2.8 Schematic of the proposed multi-pole bandpass filter [16].

2.2.6 Perforations in the Transmission Lines

Since the ground plane is perforated, the substrate needs to be suspended. The circuits are not supported by a metal base for mechanical robustness. Perforation on the transmission line, itself, is a potential solution to this problem [17].

According to the transmission line theory, the propagation constant of a lossless line is $\beta = \omega_0 \sqrt{LC}$, where ω_0 is the angular frequency, and C and L are the distributed shunt capacitance and series inductance per unit length, respectively. It is indicated that slow-wave (large β) can be obtained by increasing C and L. Consequently, it is possible to form an EBG structure on the transmission line, if C and L are not increased continuously but periodically [18]. Xue et al. have proposed two one-dimensional (1-D) microstrip EBG cells, as shown in Fig. 2.9 [18]. The cells are a segment of a microstrip line with some metals removed. The narrow connecting lines increase the value of the series inductance. Gaps across the width of

the line result in the increment of the shunt capacitance. By cascading these cells, an EBG microstrip line is constructed to present a remarkable slow-wave and stop-band performance, similar to other EBG structures with ground perforations. Fig. 2.10 displays the simulated and measured *S*-parameters of the EBG transmission lines by using six EBG cells shown in Fig. 2.9 (b).

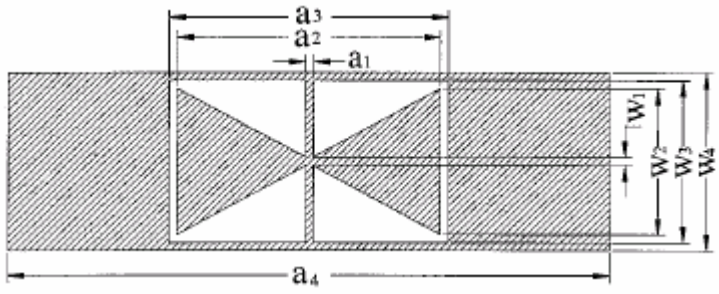

(a)

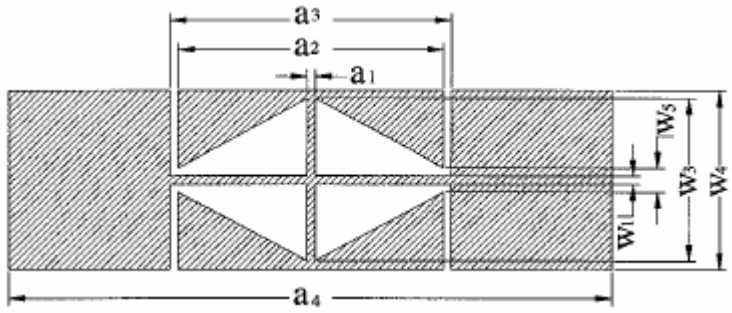

(b)

Fig. 2.9 1-D microstrip EBG cells [18]: (a) EBG cell 1 and (b) EBG cell 2.

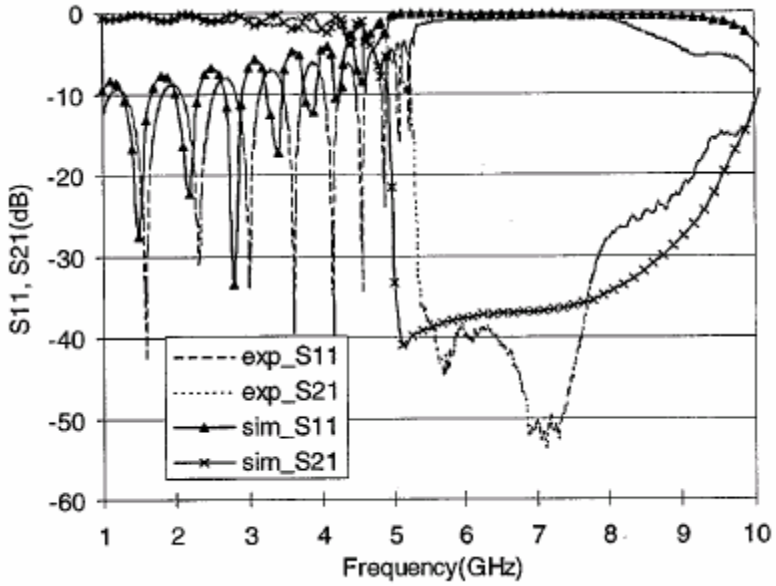

Fig. 2.10 Simulated and measured *S*-parameters of the proposed EBG transmission line using six EBG cells shown in Fig. 2.9 (b) [18].

For conventional EBG structures, the microstrip line must be carefully oriented on the substrate. In the case of perforated transmission lines, the dependence of the location and orientation of the microstrip line on the propagation constant is completely eliminated. The perforated transmission line structure will have many potential applications in microstrip circuits.

2.2.7 Analysis of EBG Structures

Several commercial full-wave EM softwares such as Ansoft Ensemble, Ansoft HFSS, Zeland IE3D**,** Sonnet, Microwave Studio, and Microwave Office are available for the design of EBG-based microwave circuits. In addition, there have been many successful numerical studies. To model bulky EBG structures, a number of algorithms such as the Plane Wave expansion Method (PWM), the Transfer Matrix Method (TMM), the Effective Index Method (EIM), the Coupled-Mode Theory (CMT), the Bloch Waves Method (BWM), the Scattering Matrix Method (SMM), and Leaky Mode Propagation (LMP) method have been proposed [19].

For photonic-crystal based waveguide structures, standard numerical techniques such as finite-difference and Finite-Element Method (FEM) are usually applied for investigating the modal and dispersion characteristics of the waveguide.

The RF characteristics of EBG structures are determined by many parameters, including the number of lattices, lattice shapes and lattice spacing. As a result, the use of full-wave EM simulators becomes very time-consuming, when complicated EBG structures are analyzed and designed. Thus, circuit analysis is a very useful tool for simulation and design purposes.

Typically, a lumped-element equivalent circuit model is employed in the initial design [11, 12, 20]. The equivalent circuit parameters of the circuit are extracted by using a combination of the transmission line theory and the full wave analysis. The transmission characteristics of an EBG structure can be easily found by any circuit simulator such as HPADS. The design, based on the equivalent circuit, has proven to be sufficient enough for the initial design. The resultant equivalent circuit and parameters for the EBG structures can be directly adapted to the design of a practical circuit.

2.3 Tunable Lowpass Filters

In general, tuning capability can be achieved by incorporating tuning elements such as tunable inductors/capacitors into lowpass filters or by using the tunable thin-film technique.

2.3.1 MEMS Tunable Lowpass Filters

Recently, a number of MEMS-based tunable lowpass filters have been reported [21-23]. In particular, MEMS switches or MEMS varactors are the main tuning elements utilized in such types of tunable filters. Fig. 2.11 is a photograph of the fabricated tunable lowpass filter [21]. Fig. 2.12 demonstrates the simulated and the measured *S*-parameters of the filter in Fig. 2.11. This tunable filter can operate at only two discrete frequencies.

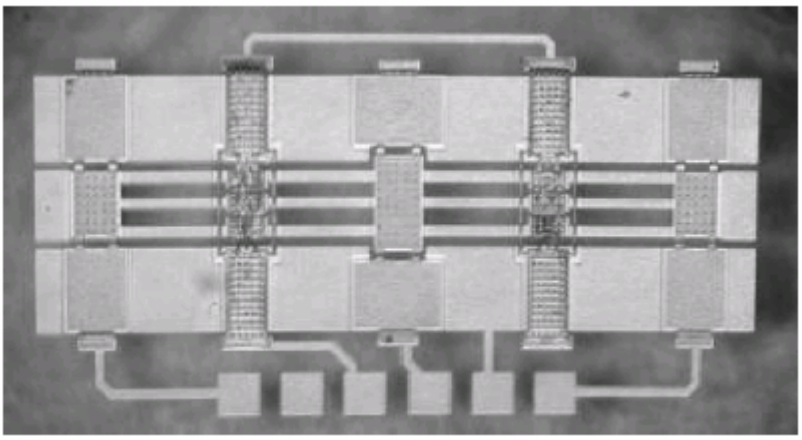

Fig. 2.11 Photograph of the fabricated tunable lowpass filter (Chip size = 0.9mm × 1.7mm) [21].

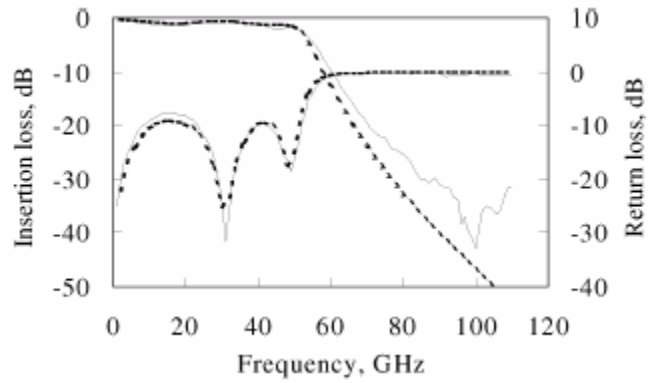

(a)

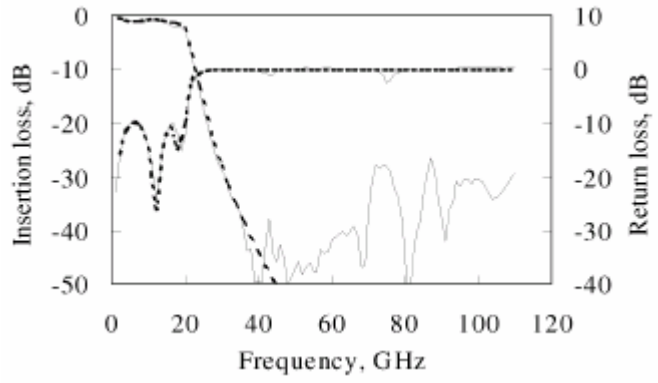

(b)

Fig. 2.12 Simulated and measured *S*-parameters of (a) wide-band state and (b) narrow-band state of the lowpass filter (the dots are the simulation results and the lines are the measurement results, respectively) [21].

2.3.2 BST Tunable Lowpass Filters

Another way to implement tunable lowpass filters is to use ferroelectric materials as the substrate. The relative dielectric constant of the ferroelectric films can be changed with the applied electric field, varying the capacitance or inductance in the circuits. Barium-Strontium-Titanate (BST) is the one of the most popular ferroelectric films being studied. Fig. 2.13 is a schematic of parallel-plate BST capacitors [24]. The tuning capability of the tunable lowpass filters, constructed by the BST capacitors, is shown in Fig. 2.14 [24]. This filter has an insertion loss of approximately 2dB, and a return loss of better than 7dB in the passband.

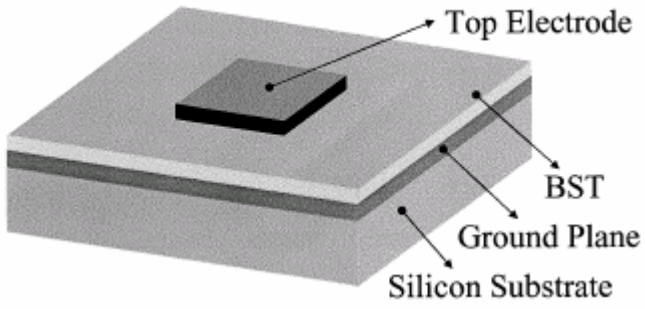

Fig. 2.13 Schematic of the parallel-plate BST capacitors [24].

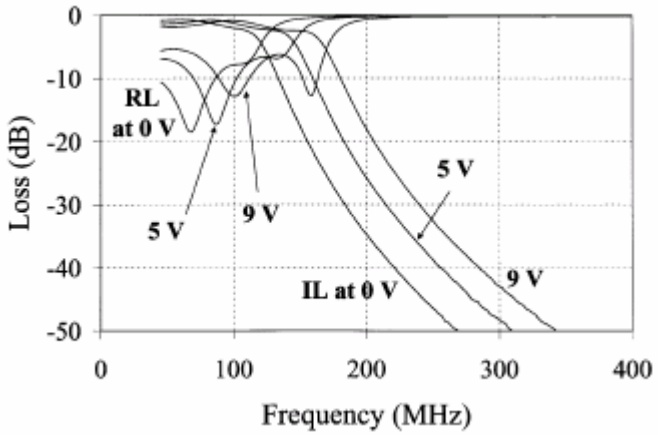

Fig. 2.14 Insertion and return losses of the fifth-order LPF with a change in the DC-bias voltage [24].

2.4 Dielectric Resonator Filters

Microwave filters and diplexers/multiplexers are essential components in radar, satellite, and mobile communication systems to discriminate between wanted and unwanted signal frequencies. Typically, they are narrow-band bandpass devices with stringent specifications for passband insertion loss, stopband rejection, power handling, and physical size. Their practical realization varies depending on the applications. Metallic waveguide filters consist of hollow cavities with rectangular, quadratic or circular cross-sections. Typically such filters are adopted for low insertion-loss applications due to their typical high Q-factor (up to 10,000), although the configuration is considerably large and unfavorable for connecting with planar circuit components. On the contrary, planar filters are clearly the most convenient to fabricate and eliminate bulky waveguides in a majority of microwave systems. Their low Q-factor (up to 500) allows only a moderate performance, excluding those filters from the more demanding applications in modern communication systems. Microwave filters with both a compact size and high-Q performance are intensively desired.

A high Q-factor is achievable only with low-loss DR filters or superconductor filters. Although the latter can attain a Q-factor as high as 100,000, DR filters are capable of providing a Q-factor of more than 20,000. The relative dielectric constant of the materials for constructing DR filters is a number substantially larger than unity (i.e., 20-90). The primary advantage in usage of dielectrics is to miniaturize the filter sizes. The size of DR filters is considerably smaller than the size of waveguide filters operating at the same frequency. Furthermore, these DR filters are employed to replace waveguide filters in applications such as satellite communication systems where planar filters cannot be used because of their inherently high losses.

2.4.1 Dielectric Materials

Primarily, the loss of a DR filter is determined by the loss tangent of the dielectric material used to construct the DR filter as well as the conductor loss of the metallic enclosure outside the filter. If the dielectric resonators are physically remote from the walls of the

metallic enclosure, then the electromagnetic energy storage is largely confined to the interior of the resonators. As a result, the dielectric losses become dominant. The Q-factor relates a resonator's capacity for energy storage with its energy dissipation through heat. Thus, the less the dielectric losses, the higher the Q-factor is. Moreover, the high dielectric constant of the dielectric materials results in a dramatic reduction in wavelength, compared with free space. Consequently, an unloaded Q-factor (Q_u) of up to 50,000 can be obtained in a reasonable volume. This is impossible for metallic waveguide filters.

Over the past decade, the advances in dielectric materials have made it possible to combine a high Q-factor, high dielectric constant, and small temperature drift in materials suitable for use at microwave frequencies. High Q-factor dielectric materials with a dielectric constant ranging from 20 to 90 are now commercially available from various manufacturers. According to the classical dispersion characteristics of dielectric materials, the dielectric loss increases with frequency f while relative dielectric constant ε_r remains unchanged. Therefore, the product of Q and f describes the basic properties of each dielectric material. Table 2.1 summarizes the characteristics of the representative dielectric materials currently available [25]. These materials not only have high-Q values but also high dielectric constants. Moreover, they have a good temperature coefficient.

Table 2.1 High-Q dielectric materials [25].

Materials	ε_r	Q	τ_f (ppm/°C)	f (GHz)
$MgTiO_3$-$CaTiO_3$	21	8000	0	7
$Ba(Mg,Ta)O_3$	25	16000	3	10
$Ba(Mg,Ta)O_3$	25	35000	4	10
$Ba(Sn,Mg,Ta)O_3$	25	20000	0	10
$Ba(Mg,Ta)O_3$-$Ba(Zn,Ta)O_3$	27	15000	0	10
$Ba(Zn,Nb)O_3$-$Ba(Zn,Ta)O_3$	30	14000	0	12
$Ba(Zr,Zn,Ta)O_3$	30	10000	0	10
$(Ca,Sr,Ba)ZrO_3$	30	4000	5	11
BaO-TiO_2-WO_3	37	8800	2	6
$(Zr,Sa)TiO_4$	38	7000	0	7
$Ba_2Ti_9O_{20}$	40	8000	2	4
$Sr(Zn,Nb)O_3$-$SrTiO_3$	43	5000	-5 ~ +5	5
BaO-Sm_2O_3-$5TiO_2$	77	4000	15	2
BaO-PbO-Nd_2O_3-TiO_2	90	5000	0	1
TiO_2	104	40000 (Qf)	+460	-
$CaTiO_3$	180	7000 (Qf)	+910	-
$SrTiO_3$	304	3300 (Qf)	+1700	-

2.4.2 Dielectric Resonator Filters and Diplexers/Multiplexers

Various types of DR filters and diplexers/multiplexers have been adopted in microwave communication systems.

2.4.2.1 Configurations of Dielectric Resonators

DRs are the basic building block of DR filters. Fields inside a resonator store energy at the resonant frequency where the equal storage of electric and magnetic energies occurs. Fig. 2.15 is a sketch of a commonly used dielectric resonator structure [26]. To prevent losses due to radiation, the entire device is enclosed in a shielding of metal, most often aluminum or copper. Usually, the shape of a dielectric resonator is a short, solid cylinder, but can also be cubic, spherical, and tubular shapes.

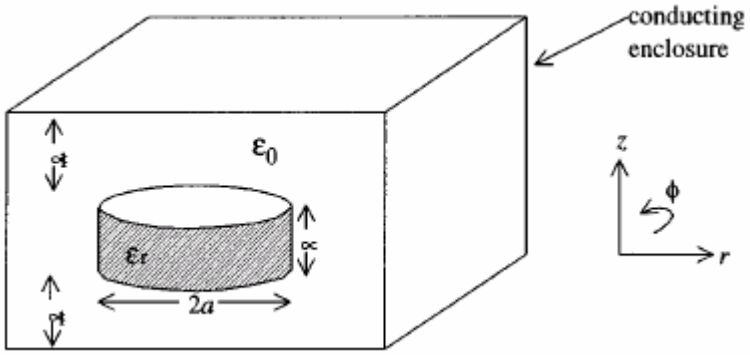

Fig. 2.15 Commonly used DR structure [26].

At the resonant frequency, most of the electromagnetic energy is stored within the dielectric, since the DR is remote from the enclosure. The resonant frequency of the structure is largely controlled by the dimensions and dielectric constant of the dielectric material. The *Q*-factor of the DR is dominated by the loss tangent of the dielectric. By assuming that the lateral surface of the DR behaves as an ideal magnetic wall, the resonant frequency and field pattern are approximately calculated. In other words, there is a zero tangential magnetic component on the curved surface of the DR.

2.4.2.2 Resonant Modes of Dielectric Resonators

Like all resonant cavities, there are many possible operating modes which can be excited in DRs. These modes are divided into three categories: Transverse Electric (TE), Transverse Magnetic (TM), and Hybrid Electromagnetic (HEM) modes. Fig. 2.16 displays the electromagnetic field distributions for these modes in a cylindrical DR [26]. A typical DR mode chart is shown in Fig. 2.17 [26]. Comprehensive studies of modes in DRs, including the mode chart for the cylindrical resonator, are published by Rebsch [27], Courtney [28], Kobayashi [29], Zaki and Atia [30], and others [31].

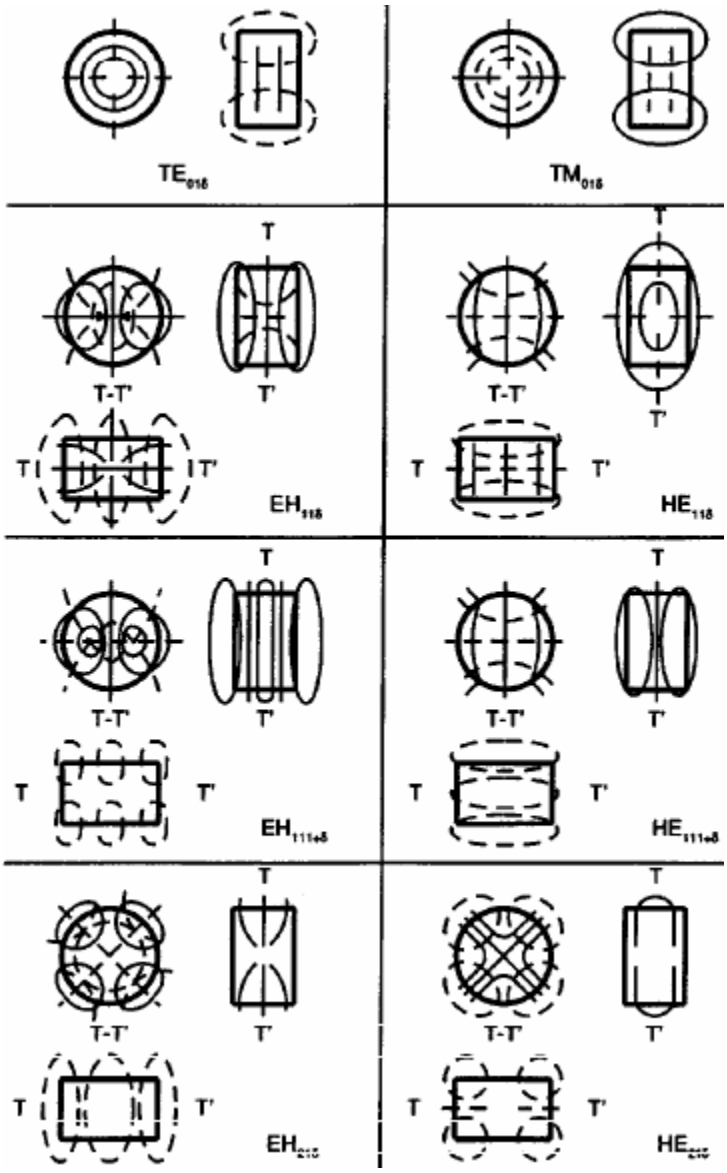

Fig. 2.16 DR modes [26].

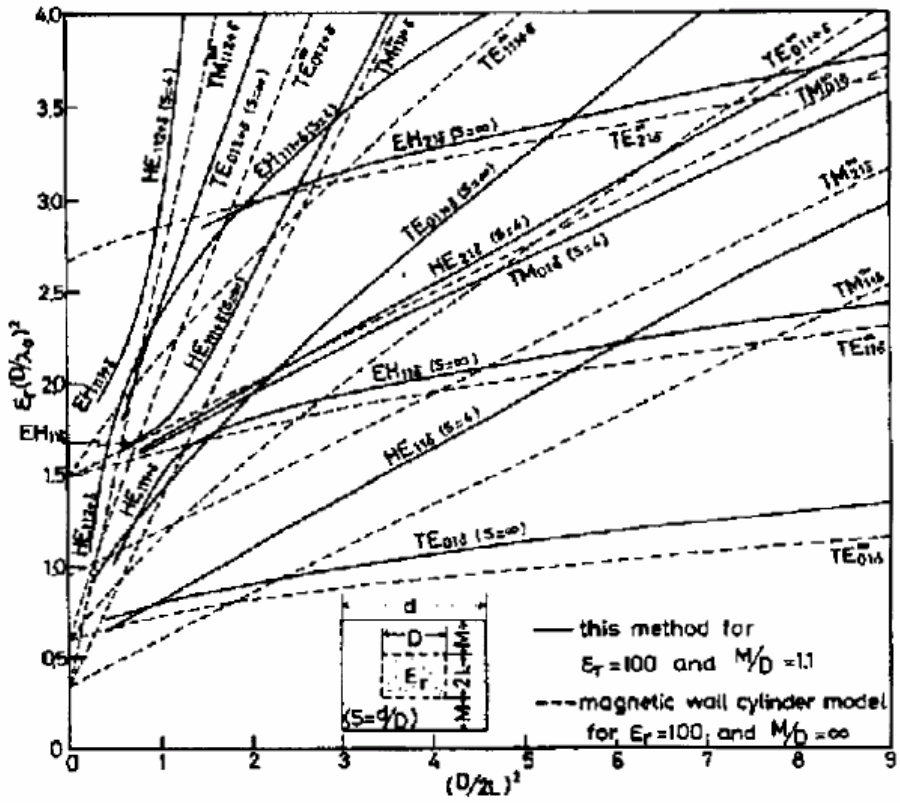

Fig. 2.17 DR mode chart [26].

The operating modes have an impact on the filter size, unloaded Q, and spurious performance. A proper mode should be selected for a particular application. A commonly-used resonant mode in cylindrical dielectric resonators, sketched in Fig. 2.15, is denoted the TE_{01} mode, whose electric field lines are circles concentric with the axis of the cylinder. When the relative dielectric constant is approximately 40, more than 95% of the stored electric energy of the TE_{01} mode, as well as a large portion of the stored magnetic energy (typically over 60%), are confined within the cylinder. The remaining energy is distributed in the air around the resonator, decaying rapidly with distance away from the resonator surface. The dielectric resonators operating in the single TE_{01} and TM_{01} modes exhibit especially high-Q performance at microwave frequencies. However, for certain applications such as for a dual-mode filter, the HEM_{11} mode has definite advantages. Dual-mode DR filters offer roughly a 30% volume saving in comparison with single-mode DR filters.

2.4.2.3 Various Types of Dielectric Resonator Filters and Diplexers/Multiplexers

DR filters play an important role in mobile and satellite communications. A typical DR filter consists of a number of dielectric resonators, mounted inside cavities machined in a metallic enclosure. The probes are used to couple the input and output electromagnetic energy, whereas the irises are used to provide the required coupling between the resonators. The DR filters that are most commonly used in microwave systems can be divided into two configurations: individual dielectric resonators that are loaded coaxially in a metallic enclosure, or individual resonators that are mounted in a planar configuration.

Since the end of the 1960s, great progress has been achieved in DR filter technology. Cohn et. al. have performed the first extensive theoretical and experimental evaluation of the dielectric resonator [32]. The first practical DR filter was reported at the 1975 IEEE MTT-S International Microwave Symposium, Palo Alto, CA. Fig. 2.18 shows the schematic structure of this 6.9GHz filter [33].

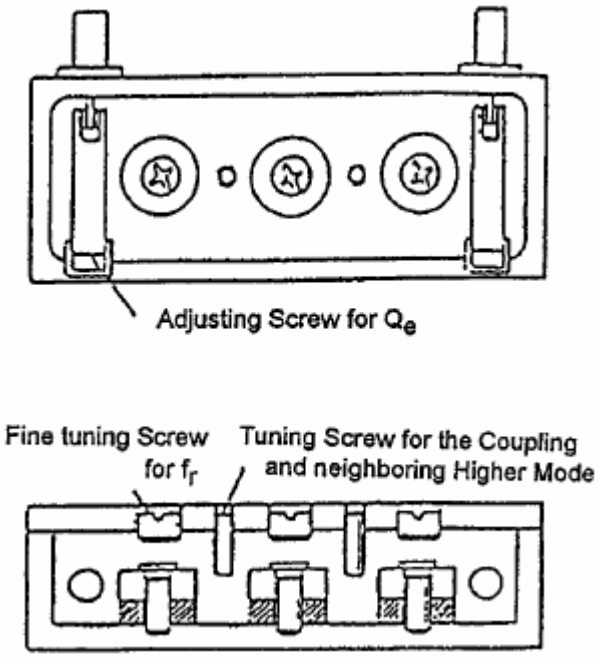

Fig. 2.18 Structure of the 6.9GHz DR filter [33].

The ratio of the fundamental resonant frequency to the first spurious HE_{11} mode resonance is typically 1:1.3, which can be improved to 1:1.5 by inserting a hole in the centre of the dielectric resonator [26]. Since more magnetic energy than electric energy leaks from DRs, resonators are coupled magnetically via irises in the filter body. A typical TE_{01} multi-pole DR filter for cellular base-station applications is illustrated in Fig. 2.19 [26].

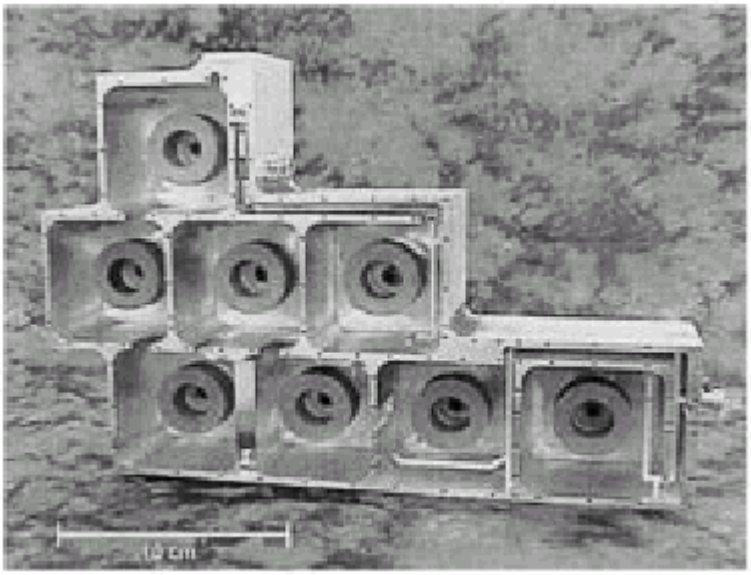

Fig. 2.19 TE_{01} DR filter for cellular base-station applications [26].

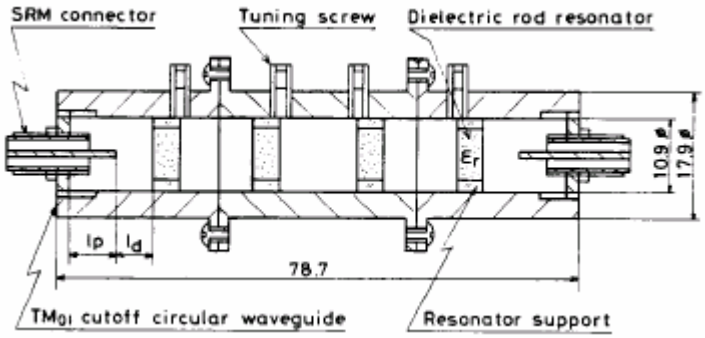

Fig. 2.20 Configuration of a TM mode DR filter [34].

An alternative structure consists of ground dielectric rods operating in the single TM_{01} mode. This structure is larger, but simpler. A compact DR filter of this type with good spurious characteristics can be constructed by placing a high-Q TM_{01} dielectric rod resonator coaxially in a TM_{01} cutoff circular waveguide, as detailed in Fig. 2.20 [34].

Even with a dielectric constant of 45, a typical 900MHz resonator occupies a cavity size of $8 \times 8 \times 5$ cm. Thus, size-reduction techniques are of crucial. The first significant technique was the dual-mode DR filter, reported by Fiedziuszko in 1982 [35], configured Fig. 2.21. In this case, the HE_{11} dual-mode is chosen. The coupling between resonators are via cruciform irises in the filter body, enabling the resonances in each cavity to be coupled to the resonances in the adjacent cavities. These devices are now routinely used in mobile and satellite communications applications due to their low loss, smaller volume and less mass than classical fundamental mode realizations. Subsequently, this work has been extended by Zaki [36], Kobayashi [37], and Guillon [38].

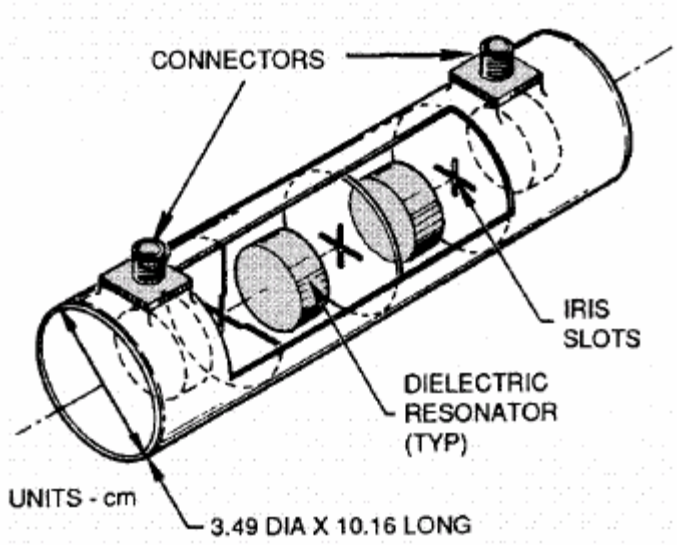

Fig. 2.21 Dual-mode DR filter configuration [35].

A further size-reduction is accomplished by using DR filters, operating in triple, quadruple, or even higher modes. Fig. 2.22 presents a 2GHz quadruple-mode DR filter [39]. This compact size filter has a potential application in the W-CDMA communication system.

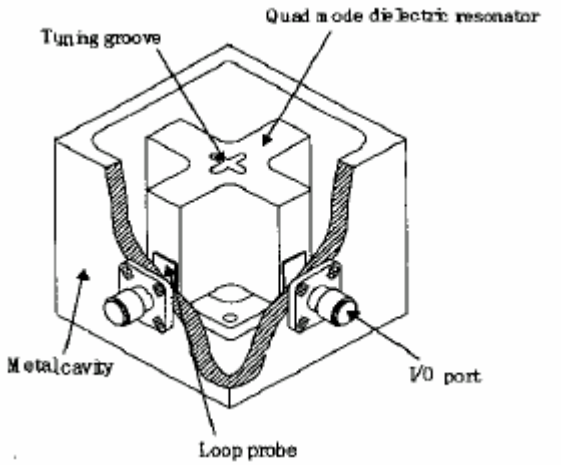

Fig. 2.22 Quadruple-mode DR filter configuration [39].

Although multimode DR filters have many advantages, they also have a major disadvantage, inferior out-of-band spurious characteristics. Usually, an additional lowpass filter is needed to eliminate the unwanted modes, increasing the size, insertion loss, complexity and cost of the filter. Significant effort has been put into improving the spurious performance of DR filters, especially dual-mode filters. A paper has reported the application of a combination of the TE_{01} mode and the HE_{11} dual-mode ring dielectric resonators in an elliptic function filter, as shown in Fig. 2.23 [40]. The filter has some single TE_{01} mode dielectric resonators and some HE_{11} dual-mode resonators. The structure achieves a good spurious performance.

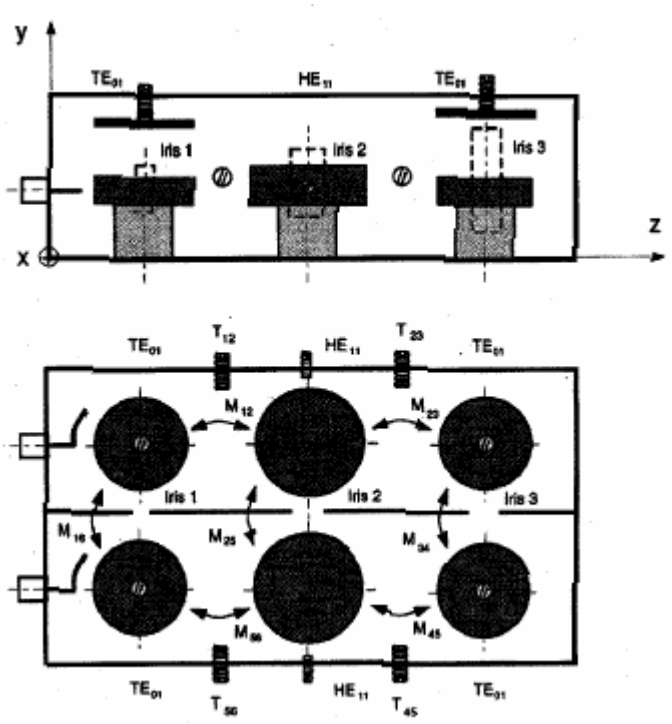

Fig. 2.23 Structure of the 6-pole mixed-mode DR filter [40].

Higher dielectric constants are desirable to reduce the size of the filters. If the dielectric resonator in a dual-mode filter is replaced by a perfect electric conductor; that is, increasing the relative dielectric constant of the resonator to approach infinity, significant miniaturization can be achieved, and high-quality filters can be realized. Additionally, in applications of using superconductors, filters with extremely low insertion losses can be achieved. The resonator operating in the HE_{11} mode has a much higher unloaded Q, and an easier realization of an elliptic-function response than that of the metallic ring resonator in a cavity operating in the quasi-TEM mode. Fig. 2.24 and Fig. 2.25 display the field distributions of the conductor-loaded resonator reported in [41] and the configuration of the conductor-loaded cavity filter [41], respectively.

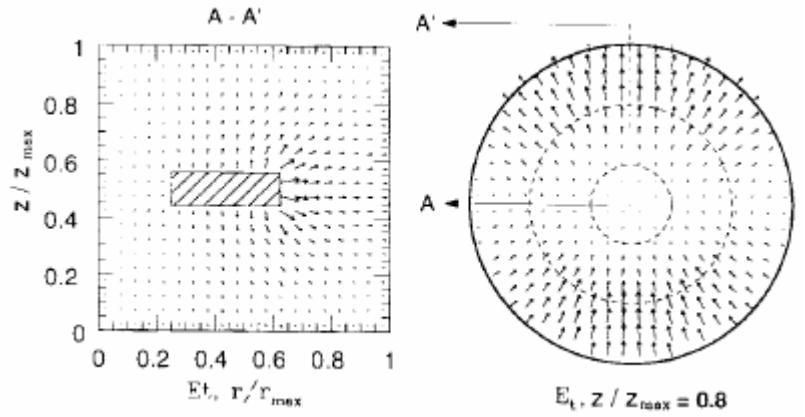

(a)

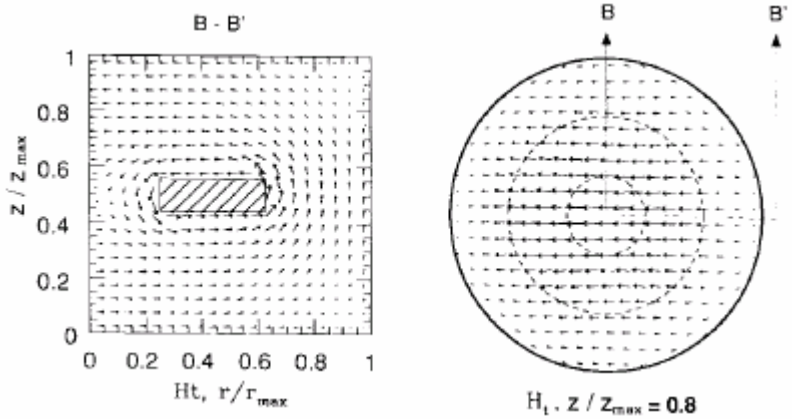

(b)

Fig. 2.24 Typical HE_{11} mode field distributions of the conductor-loaded resonator [41]: (a) electric-field distribution and (b) magnetic-field distribution.

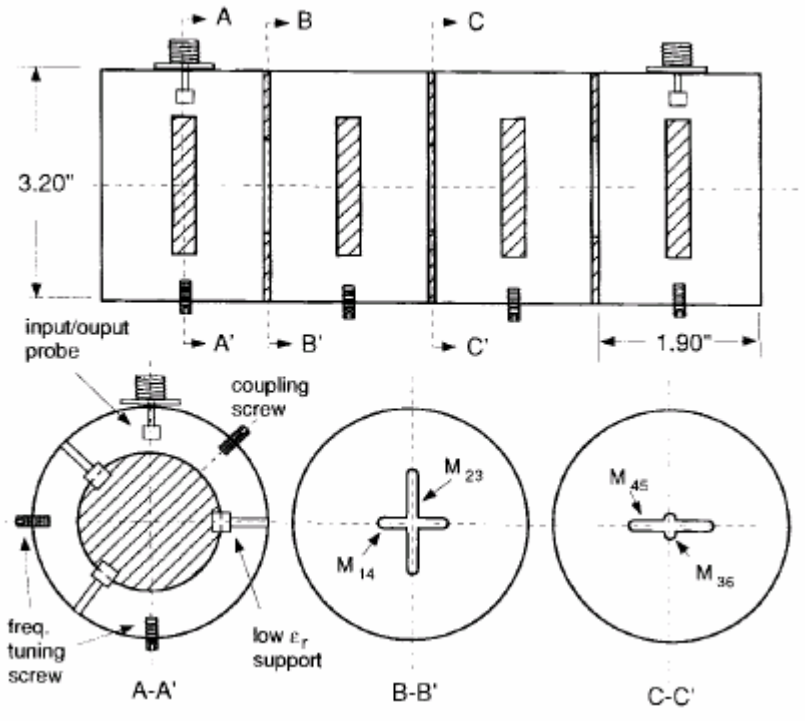

Fig. 2.25 Configuration of the eight-pole conductor-loaded cavity filter [41].

Based on this concept, similarly, a filter is developed by using one or two conductor-loaded cavities, combined with dielectric loaded cavities [42], or combining two conductor-loaded resonators of different sizes [43]. Low loss, simple structure, and a good spurious performance are the resultant advantages.

It is also possible to trade off some of the Q_u of the HE_{11} resonator for more size-reduction by modifying the geometry. By positioning the DRs on the base of a metallic housing, the HE_{11} mode is lowered in frequency and becomes the fundamental mode. A conducting disc can then be placed on top of the DR. The conductor loading on both ends prevents any tangential electric-field at the top and bottom of the DR. A good simple model for this structure is the TM_{110} mode, as in ferrite circulators. A typical dual-mode resonator of this type achieves a Q_u value of 6300 at 900MHz in a 6.5 × 6.5 × 4 cm cavity. Typically, devices of the type in Fig. 2.26 [44] occupy 50% of the volume of an equivalent coaxial filter.

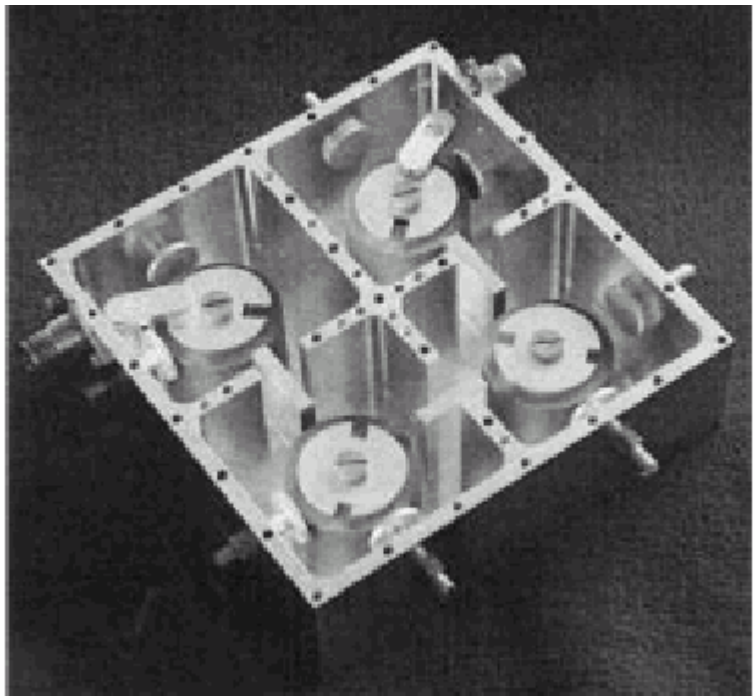

Fig. 2.26 Conductor-loaded dual-mode DR filter configuration [44].

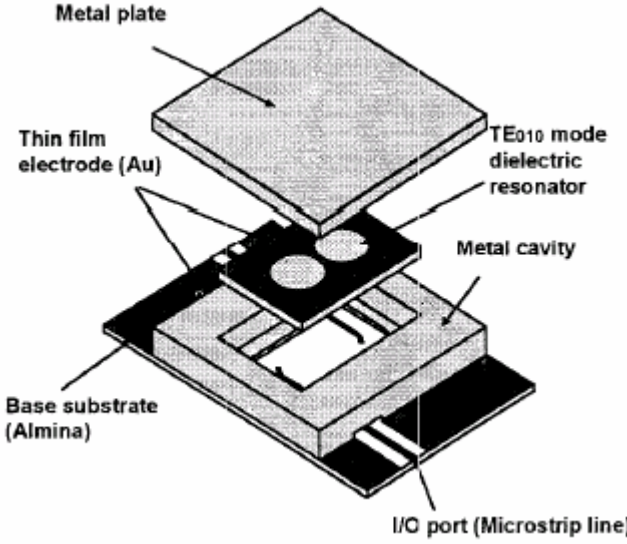

Fig. 2.27 Configuration of the V-band planar type DR filter fabricated in ceramic substrate [45].

For an easier connection to MMICs, MICs circuits, a TE_{010} mode DR filter, fabricated in a ceramic substrate, is introduced in Fig. 2.27 [45]. The filter consists of a dielectric substrate between two metal plates, and the upper and lower surfaces of the substrate are metallized. Thin-film electrodes on the both sides of the substrate have hollow circular patches of the same diameter, containing the electromagnetic field. The input and output ports are connected to the microstrip lines. To fabricate the filter with a high precision, the photolithography technique is utilized.

For most communication applications, many filters must be multiplexed in order to combine the signals from, or split signals to, several channels. Typical multiplexing techniques include hybrid-splitters, circulator dropping networks, and direct combination. Hybrids or splitters offer the advantage of simple design and excellent symmetry at the expense of a greatly increased insertion loss. This type of multiplexing is definitely inadequate for communication systems which require a low loss to improve the noise figure, or those have significant RF power requirements. For many years, circulator networks have been applied in low power, channelizing functions for satellite input multiplexers due to their inherently good isolation of multiple channels and relatively low loss, compared with those of a hybrid. However, this means that each channel must include at least one extra circulator, increasing the size, weight, insertion loss, and cost. A direct combination, using a RF component such as a waveguide or coaxial junction, provides the advantages of minimal weight increase, low loss, and low cost. In this case, all the channels must be tuned simultaneously. Several combiners are available, including coaxial/coaxial and coaxial/waveguide.

Typically, the filters used for diplexers consist of metal waveguides because of their low loss and high isolation, but they are quite bulky. A DR filter is another good candidate for achieving diplexers due to the advantages of a low loss, high Q, and small size. This type of diplexer comprises two DR filters (channels) connected to a three-port junction which is either a waveguide or a coaxial structure. In 1997, the DR diplexer for marine satellite systems, an isolation between transmitter (Tx) and receiver (Rx) ports of over 90dB, was proposed [46].

Fiedziuszko [35] has proposed microwave bandpass filters that employing DRs, operating in the dual-mode configuration with a coaxial interface. With the well-proven channel dropping scheme, such filters can be implemented to provide an input multiplexing network for the satellite payload. A three-channel C-band manifold-coupled multiplexer, including DR filters, has been demonstrated for a potential utilization in satellite output multiplexers [47]. Fig. 2.28 reflects this new multiplexer configuration which utilizes dual-mode and triple-mode DR filters, coupled to a ridged waveguide manifold. For ease of fabrication and for power handling capabilities, the dielectric resonators are planar-mounted. This design offers a significant size and weight reduction, while preserving the optimum electrical performance. Furthermore, the thermal design and subsequently measured data under high power in a vacuum has established the suitability of dielectric resonator output multiplexers for C-band satellite applications.

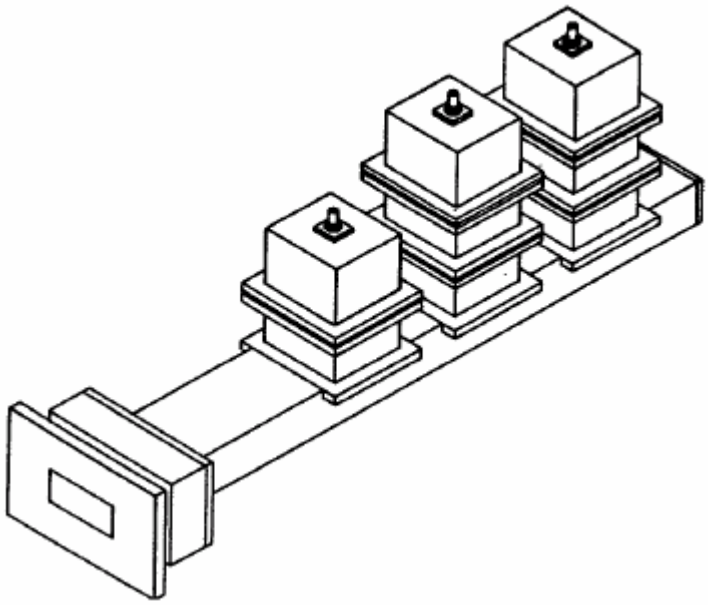

Fig. 2.28 Broadband dielectric resonator output multiplexer [47].

Fig. 2.29 presents another design of the HE_{11} mode dielectric resonator output multiplexer reported in [48].

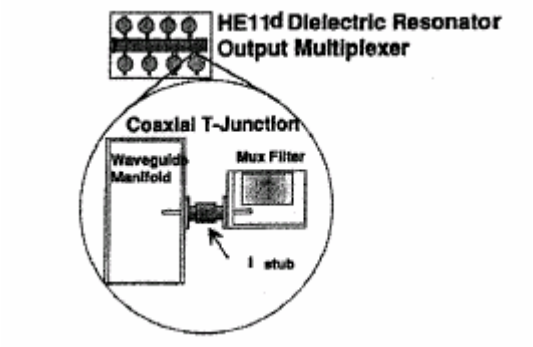

Fig. 2.29 Configuration of a dielectric resonator multiplexer [48].

Chapter 3

Modelling and Development of Novel EBG-Based Microstrip Filters

3.1 Introduction

Over the last decades, several attempts to control the propagation of electromagnetic waves through perforated ground planes have been described in the literature [1, 2]. Microstrip transmission lines with special perforation patterns (i.e., EBG structures) on the ground plane have attracted attention, because of their amenability to standard MIC fabrication techniques. For instance, UC-EBG structures [9, 20], and DGSs [11, 13], have been successfully applied in the construction of microwave filters and antennas.

Microstrip lines incorporating EBG structures on the ground plane (i.e., microstrip EBG structures) have exhibited a passband-stopband filter characteristic and a slow wave effect [2, 49]. These features can be used in bandstop or lowpass filter applications to eliminate unwanted frequencies and to reduce the physical size of microstrip circuits. The majority of such structures consist of a two-dimensional periodic array of holes etched on the ground plane. So far, several variations of microstrip EBG structures have been reported [6-8].

Despite the afore mentioned advantages and wide applications of microstrip EBG structures, there still remain some problems in utilizing such structures. In this chapter, these problems are addressed and solutions are suggested. Novel microstrip filter configurations, incorporating EBG structures, are proposed. These new EBG-based microstrip filters include bandstop filters, lowpass filters, and bandpass filters. All are compact with a good RF performance. The design of the proposed filters is based on a general synthesis method by using both an *RLC* lumped-element circuit model and a more accurate transmission line circuit model. An efficient (fast and accurate) analysis for the proposed EBG-based microstrip filters is demonstrated and compared with the EM simulation results to verify the concept, as well as the validity of the developed circuit models.

3.2 Problems of Conventional Microstrip EBG Structures

When an electromagnetic wave propagates through a periodic structure, there exist certain frequency bands, where the wave propagates unattenuated (under ideal situations when the losses caused by conductor or dielectric substrate are ignored), known as passbands. They are separated by other cutoff frequency bands, called forbidden bands (stopbands). The passband-stopband property can be employed to enhance the stopband characteristics of microwave filters.

Design considerations in evaluating the performance of a microstrip EBG structure include the bandwidth of the stopband, the rejection level in the stopband, and the return loss (ripples) in the passband. To obtain good performance from the microstrip EBG structure, a wide bandwidth, a deep rejection level and small passband ripples are necessary. However in conventional microstrip EBG structures, there is always a conflict between the stopband and the passband characteristics [5, 9]; that is, increasing the size of the etched hole or the number of holes produces a wider stop bandwidth and a better stopband rejection at the expense of the passband; reducing the size of the hole improves the return loss, but degrades the stopband characteristics. To achieve the best performance, this tradeoff situation requires factors such as the number and size of the etched holes to be carefully determined.

To make this problem easier to understand, four different microstrip EBG structures with rectangular holes etched on the ground plane, as shown in Fig. 3.1, are investigated. These four configurations have the same periodicity but different numbers and sizes of holes. The corresponding EM simulation results from Momentum [50] are graphed in Fig. 3.2.

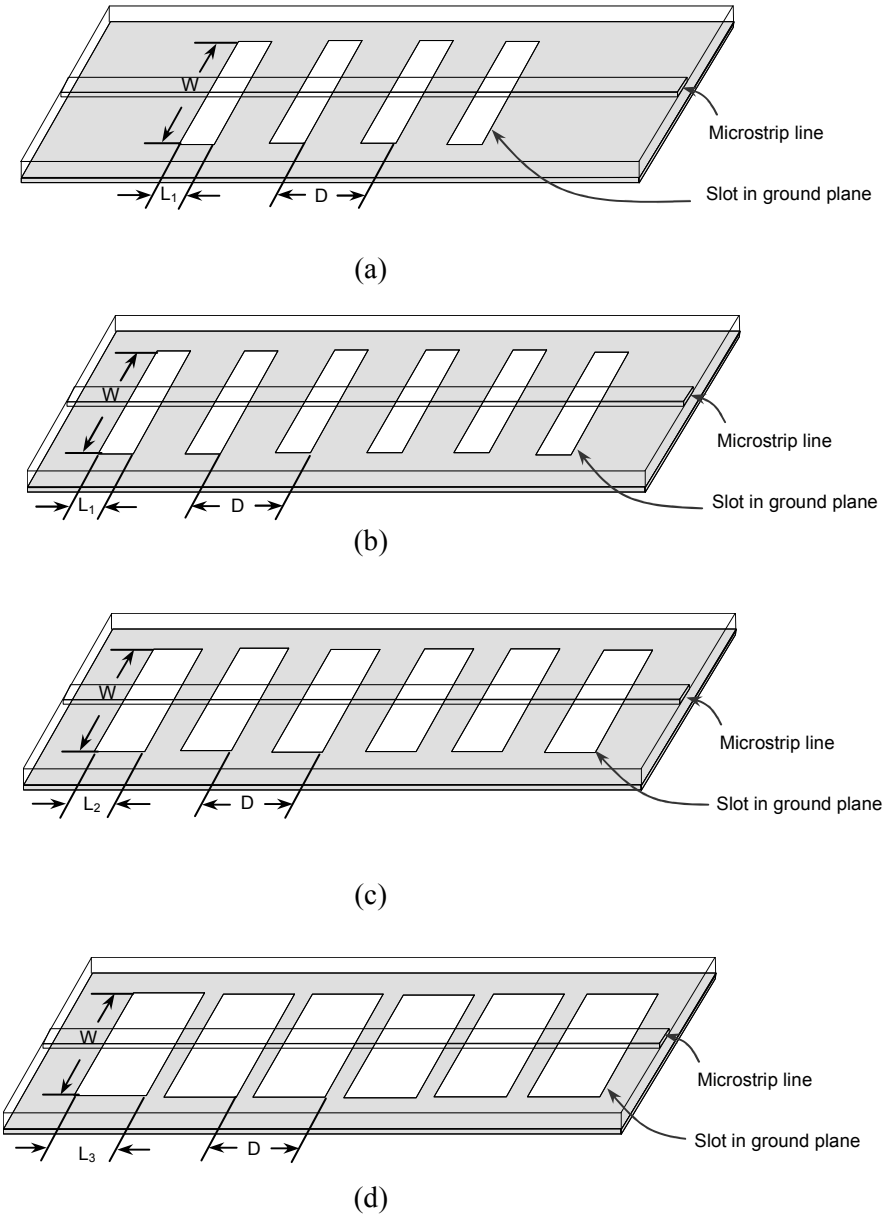

Fig. 3.1 Microstrip EBG structures with rectangular holes etched on the ground (0.635mm-thick substrate with a dielectric constant of 10.2); Periodicity: D = 3.9mm; Width of the holes: W = 3.0mm; Length of the holes: (a) L_1 = 0.75mm (4 holes), (b) L_1 = 0.75mm (6 holes), (c) L_2 = 1.5mm (6 holes), and (d) L_3 = 2.25mm (6 holes).

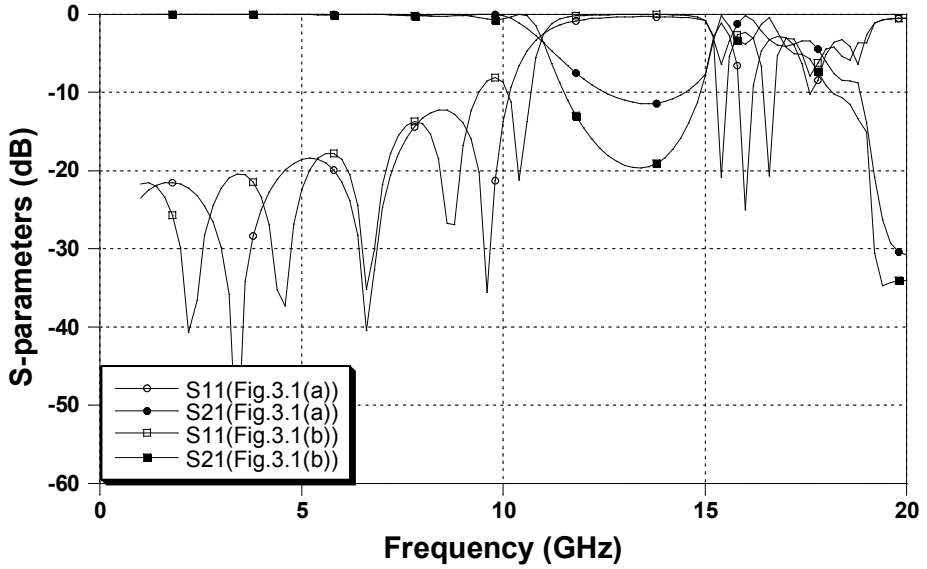

(a)

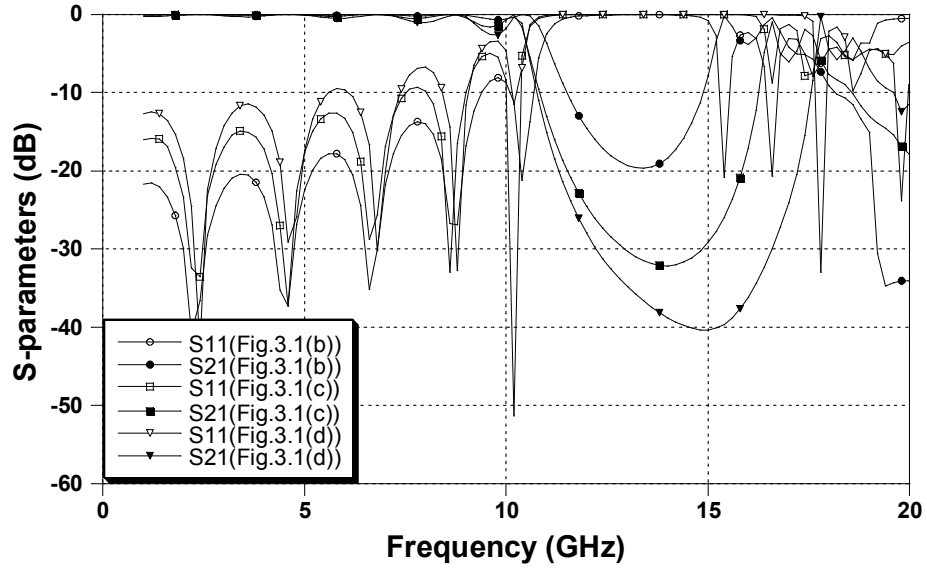

(b)

Fig. 3.2 Frequency responses of the microstrip EBG structures shown in Fig. 3.1: (a) comparison of the frequency responses of Fig. 3.1 (a) and Fig. 3.1 (b), and (b) comparison of the frequency responses of Fig.3.1 (b), Fig. 3.1 (c), and Fig. 3.1 (d).

It is evident from Fig. 3.2 (a) that increasing the number of the holes from 4 to 6 results in a better rejection level in the stopband. It is also observed from Fig. 3.2 (b) that increasing the size of the hole improves the stopband characteristics, but degrades the passband return loss.

The problem can be further demonstrated by carrying out a simple one-dimensional transmission line periodic structure analysis [51]. An equivalent network of a unit cell is a shunt normalized susceptance $\overline{B}$ with transmission lines (length = $d/2$, where d is the periodicity of the structure) on both sides as depicted in Fig. 3.3, where V_n and I_n are the total voltage and current amplitudes, respectively; that is, the sum of the contributions from the incident and reflected TEM waves at the terminal plane. The diagram illustrates the voltage-current relationships at the input and output of the n_{th} section in the cascaded periodic structure.

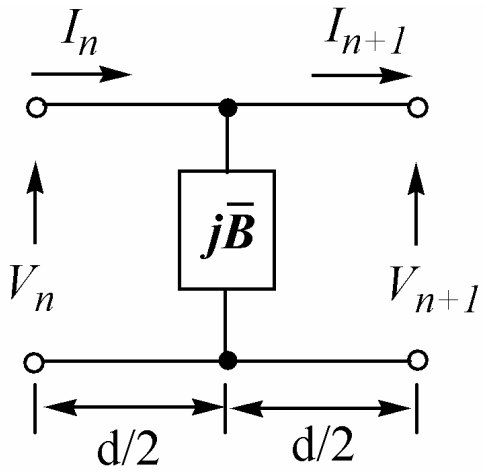

Fig. 3.3 Equivalent circuit for a unit cell of the microstrip EBG structure.

The transmission characteristics of the periodic structure are evaluated by determining the complex propagation constant $\gamma = \alpha + j\beta$ for the overall periodic structure. If the periodic structure is capable of supporting a propagating wave, then the voltage and current at the $(n+1)_{th}$ terminal should be exactly the same as the voltage and current at the n_{th} terminal, apart from a phase delay due to a finite propagation time. The propagation constant can then be obtained by solving the following characteristic equations [51]:

$$\left(\begin{bmatrix} A & B \\ C & D \end{bmatrix} - \begin{bmatrix} e^{\gamma d} & 0 \\ 0 & e^{\gamma d} \end{bmatrix}\right)\begin{bmatrix} V_{n+1} \\ I_{n+1} \end{bmatrix} = 0 \tag{3.1}$$

and

$$\begin{vmatrix} A - e^{\gamma d} & B \\ C & D - e^{\gamma d} \end{vmatrix} = AD - BC + e^{2\gamma d} - e^{\gamma d}(A + D) = 0\,, \tag{3.2}$$

where A, B, C, and D are the elements of the ABCD matrix of the unit section in Fig. 3.3. For the case where $\left|\frac{A+D}{2}\right| < 1$, $\gamma = j\beta$, and attenuation constant α is zero. Under such circumstances, the periodic structure works in the propagating mode, representing the passband of the periodic structure. The propagation constant is then given by

$$\cos \beta d = \frac{A + D}{2}\,. \tag{3.3}$$

For the case where $\left|\frac{A+D}{2}\right| > 1$, the periodic structure is an evanescent mode. In this case, $\beta = 0$, $\gamma = \alpha$, and the attenuation constant is given by

$$\cosh \alpha d = \begin{cases} -\dfrac{A + D}{2}, & \dfrac{A + D}{2} < -1 \\ \dfrac{A + D}{2}, & \dfrac{A + D}{2} > 1 \end{cases}\,. \tag{3.4}$$

Three configurations of the unit cell are reflected in Fig. 3.4. Width *W* of these unit cells is fixed while the lengths differ. The ABCD matrices of these unit cells are calculated by Momentum. The results obtained, for α, are exhibited in Fig. 3.5. It is evident that a wide stopband is obtained with the use of the large size unit cell. However, this considerably degrades the return loss in the passband.

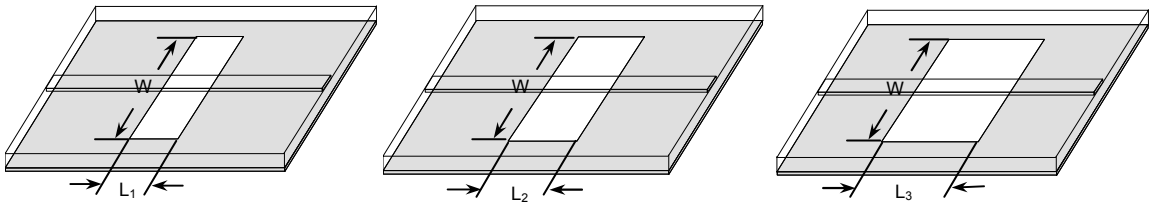

(a) (b) (c)

Fig. 3.4 Single units of the microstrip EBG structures with rectangular holes etched on the ground (0.635mm-thick substrate with a dielectric constant of 10.2): (a) L_1 = 0.75mm, (b) L_2 = 1.5mm, and (c) L_3 = 2.25mm.

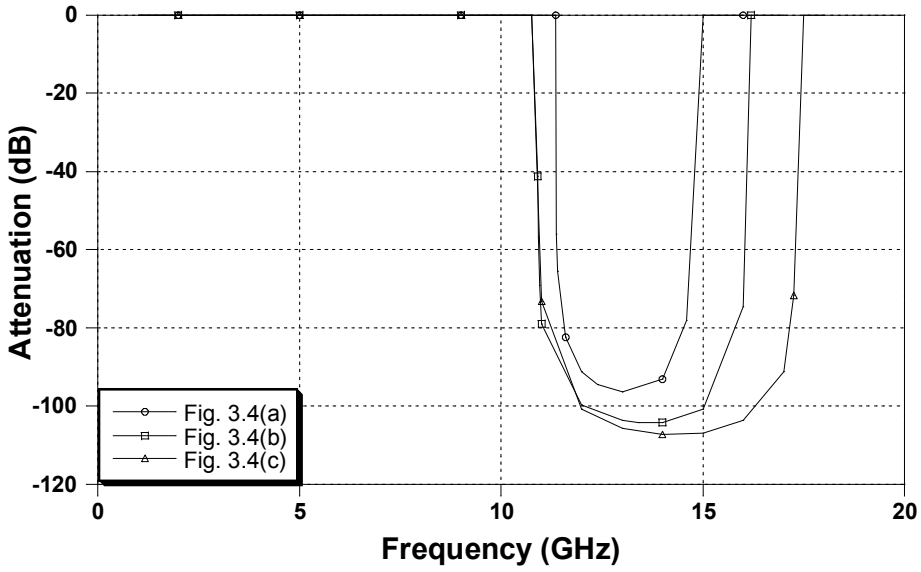

Fig. 3.5 Comparison of the attenuation constants corresponding to the structures in Fig. 3.4.

It is obvious from the previous discussion that the RF performance of microstrip EBG structures is determined by many factors, including the periodicity, and the number and size of the holes. The use of full-wave EM simulators can become very time-consuming, because the design of EBG structures is complicated. Therefore, a rigorous and efficient field analysis for EBG structures is critical.

3.3 EM Analysis of Microstrip EBG Structures

To analyze the microstrip EBG structures in Fig. 3.1, especially the ones with a large array of holes, commonly used EM analysis methods such as the Method of Moment (MoM), Finite Element Method (FEM), and the Finite Difference Time Domain (FDTD) method take considerable CPU-time. Therefore, it is proposed that the transverse resonance technique [52-54] and mode matching technique [55, 56] are applied for the EM analysis of EBG structures. The significant advantage of combining these two techniques is that there is neither the very time-consuming meshing nor the numerous unknown parameters to solve, as required by the MoM, FEM and FDTD.

For the typical microstrip EBG structure in Fig. 3.6, it can be simplified, with the use of the transverse resonance technique [54], to the two resonator structures illustrated in Fig. 3.7 (a) and (b). In other words, the analysis of the whole structure reduces to the analysis of two resonators, formed by using half the EBG structure with electric and magnetic wall terminations. Short circuit planes are inserted at some distance (L_e and L_m) away from the discontinuity for both resonators. Now the problem is to determine resonant length L_e and L_m at a specified frequency. These lengths are then used to compute the *S*-parameters of the entire structure.

For the two resonators shown in Fig. 3.7, if propagation in the *x*-direction is considered, the structure stacking in the *y*-*z* plane is regarded as a cascaded discontinuity (*N*-furcated waveguide junction) of several layers, as displayed in Fig. 3.8.

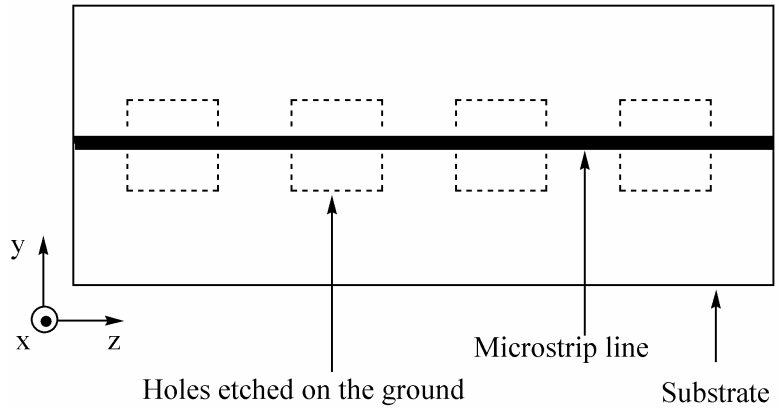

Fig. 3.6 Top view of a microstrip EBG structure.

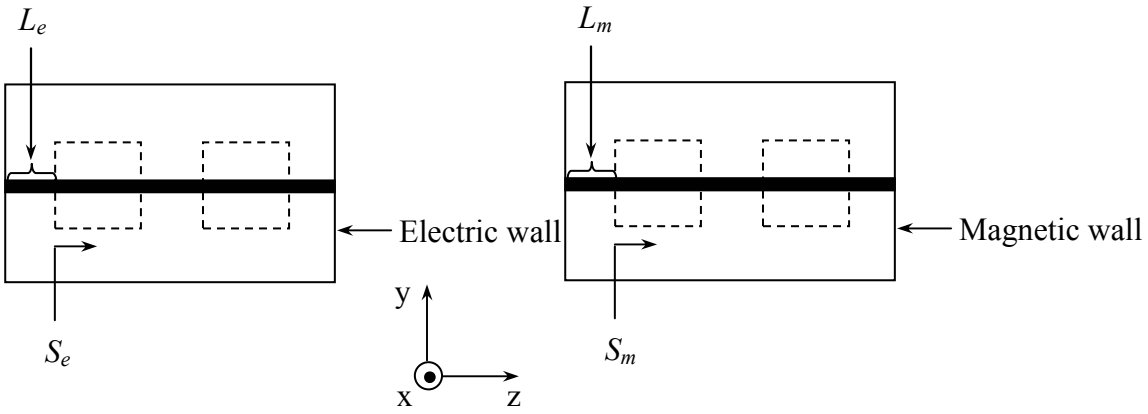

Fig. 3.7 Half structure of the microstrip EBG structure in Fig. 3.6: (a) with electric wall termination by inserting short circuit planes at some distance L_e and (b) with magnetic wall termination by inserting short circuit planes at some distance L_m.

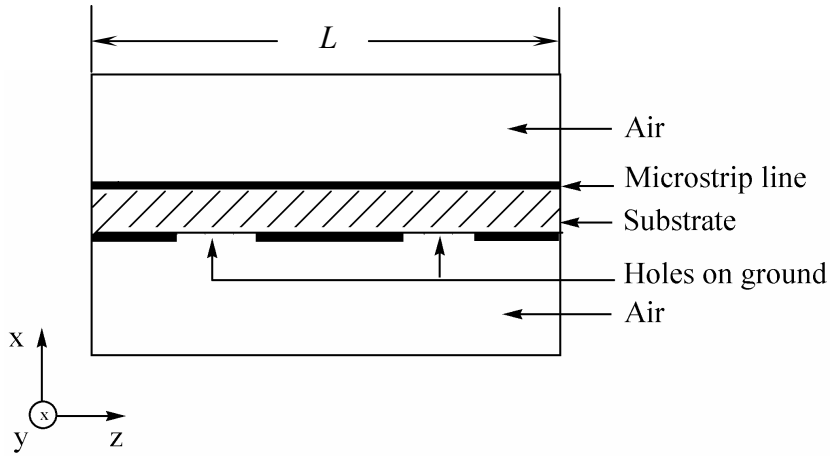

Fig. 3.8 Side view of the microstrip EBG structure (half) shown in Fig. 3.7.

The *S*-parameters of each of the discontinuities in Fig. 3.8 are determined by the mode matching technique [55]. The scattering at *N*-furcated parallel plate junction has been addressed in [56]. The analysis is extended here to deal with the scattering at the *N*-furcated waveguide junction. For example, for the discontinuity of the *N*-furcated rectangular waveguide junction, the cross-section view in the *x*-*y* plane is illustrated in Fig. 3.9.

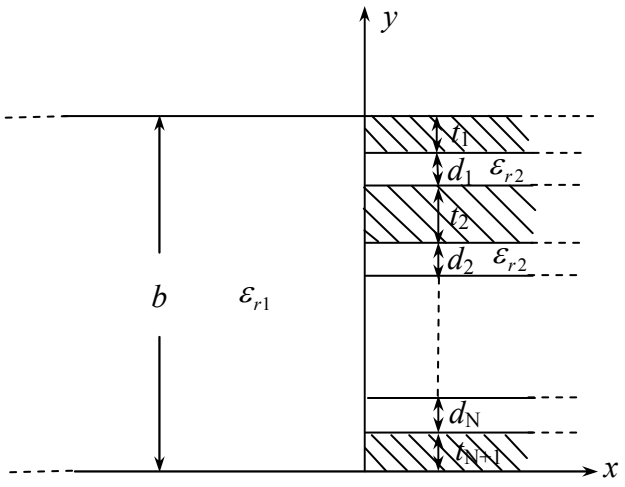

Fig. 3.9 Cross-section view in the *x*-*y* plane of the *N*-furcated rectangular waveguide junction.

The junction is composed of a normal rectangular waveguide (air/dielectric for $x < 0$) and an N-furcated waveguide (for $x > 0$). The junction fields are then readily expanded in complete sets of orthogonal TE and TM modes.

Let the transverse E-fields in the normal waveguide at junction plane $x = 0$ be given by the modal series expansion,

$$\vec{E}_0(z,y) = \sum_m A_{0p}\vec{e}_{0p}(z,y) = \overline{\overline{e}}_0^T \overline{A}_0 \,, \tag{3.5}$$

where modal vector field $\vec{e}_{0p} = \begin{cases} \cos\left(\dfrac{m\pi z}{L}\right)\cdot\cos\left(\dfrac{n\pi y}{b}\right) for TE \bmod es \\ \sin\left(\dfrac{m\pi z}{L}\right)\cdot\sin\left(\dfrac{n\pi y}{b}\right) for TM \bmod es \end{cases}$. p is the pth mode. L and b are defined in Fig. 3.8 and Fig. 3.9, respectively. The transverse E-fields in the N-furcated waveguide at junction plane $x = 0$ are expressed by the following expansion:

$$\vec{E}_i(z,y) = \sum_n A_{iq}\vec{e}_{iq}(z,y) = \overline{\overline{e}}_i^T \overline{A}_i \,, \tag{3.6}$$

where modal vector field $\vec{e}_{iq} = \begin{cases} \cos\left[\dfrac{m'\pi(z-z_i)}{L_i}\right]\cdot\cos\left[\dfrac{n'\pi(y-y_i)}{b_i}\right] for TE \bmod es \\ \sin\left[\dfrac{m'\pi(z-z_i)}{L_i}\right]\cdot\sin\left[\dfrac{n'\pi(y-y_i)}{b_i}\right] for TM \bmod es \end{cases}$. q is the qth mode and i is the ith hole. L_i and b_i are the dimensions of the ith hole in the z-direction and the y-direction, respectively.

At junction $x = 0$, the boundary conditions on the tangential E-field dictate that

$$\vec{E}_0(z,y) = \overline{\overline{e}}_0^T \overline{A}_0 = \begin{cases} 0 & over \quad t_1 \\ \vec{E}_1(z,y) = \overline{\overline{e}}_1^T \overline{A}_1 & over \quad d_1 \\ 0 & over \quad t_2 \\ \vdots & \\ \vec{E}_N(z,y) = \overline{\overline{e}}_N^T \overline{A}_N & over \quad d_N \\ 0 & over \quad t_{N+1} \end{cases} . \tag{3.7}$$

If Eq. (3.7) is multiplied by column matrix $\bar{\bar{e}}_0(z,y)$ due to the orthogonality of the modal fields, then the product is integrated over the area of the discontinuity on the *y*-*z* plane, leading to the following equation:

$$\overline{A}_0 = [H_{01} H_{02} \ldots H_{0N}] \begin{bmatrix} \overline{A}_1 \\ \overline{A}_2 \\ \vdots \\ \overline{A}_N \end{bmatrix} = H\overline{A} \,. \tag{3.8}$$

The matrices H_{0i}, $i = 1,2,\ldots,N$ are the E-field mode-matching matrices. The *pq*th elements of the matrices H_{0i} are given by

$$H_{oi,mn} = \frac{\int_S \vec{e}_{0p}(z,y) \cdot \vec{e}_{iq}(z,y) ds}{\int_S \vec{e}_{0p}(z,y) \cdot \vec{e}_{0p}(z,y) ds} \,. \tag{3.9}$$

The *S*-parameters of the *N*-furcated waveguide junction are obtained from the following equations [57]:

$$S_{22} = (P_B^T + H^T P_A^T H)^{-1} (P_B^T - H^T P_A^T H) \,, \tag{3.10a}$$

$$S_{12} = H(I + S_{22}) \,, \tag{3.10b}$$

$$S_{21} = 2(P_B^T + H^T P_A^T H)^{-1} H^T P_A^T \,, \tag{3.10c}$$

and

$$S_{11} = HS_{21} - I \,, \tag{3.10d}$$

where T denotes Hermitian transpose. P_A and P_B are the diagonal matrices whose diagonal elements are the powers, carried by the unit amplitude modes in the normal rectangular waveguide and the *N*-furcated waveguide. Good results are expected to be achieved by using

only one TE mode and one TM mode in each of the *N*-furcated waveguides, and *N* TE modes and *N* TM modes in the large waveguide.

The overall *S*-parameters of the discontinuities are then easily evaluated by the generalized scattering matrix technique. Then, resonance length (i.e., L_e and L_m) can be calculated from the *S*-parameters with the application of the transverse resonance technique; each of the lengths corresponds to a resonance frequency (f_e and f_m) through a determinant equation individually [54].

For the propagation in the *z*-direction, elements S_e and S_m (Fig. 4.8), associated with the dominant mode in the scattering matrices, are well represented by the following two equations, respectively:

$$S_e(1,1) = -e^{+j2\beta L_e} \tag{3.11a}$$

and

$$S_m(1,1) = -e^{+j2\beta L_m}, \tag{3.11b}$$

where β is the propagation constant of the dominant mode of the microstrip transmission line with EBG structures. The scattering elements of the dominant mode of the entire structure are then expressed as

$$S_{11}(1,1) = S_{22}(1,1) = \frac{1}{2}[S_m(1,1) + S_e(1,1)] \tag{3.12a}$$

and

$$S_{12}(1,1) = S_{21}(1,1) = \frac{1}{2}[S_m(1,1) - S_e(1,1)]. \tag{3.12b}$$

So far, the *S*-parameters are obtained theoretically by the transverse resonance technique and the mode matching method. The mode matching technique is well documented and covered in literatures. To demonstrate the proposed concept, HFSS [58] is used instead of the mode matching technique to calculate the *S*-parameters of the discontinuities seen in the *x*-

direction of Fig. 3.8. A lookup table is generated for frequencies versus L_e and L_m. Once L_e and L_m are obtained, the substitution in Eq. (3.11) and (3.12) provides the overall *S*-parameters of the microstrip EBG structures shown in Fig. 3.6. A comparison between the results of the proposed method and those obtained by using HFSS are provided in Fig. 3.10.

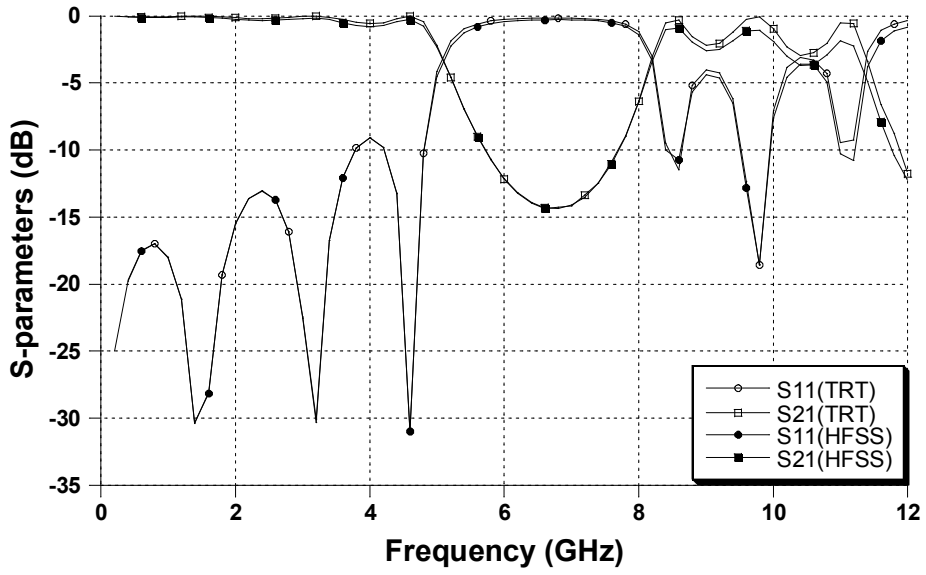

Fig. 3.10 Comparison of the *S*-parameters of the microstrip EBG structure shown in Fig. 3.6 by using transverse resonance technique and HFSS.

3.4 Proposed Microstrip EBG Structures

Although some efforts [7, 8, 59] have been reported to improve the passband-stopband performance of microstrip EBG structures, it is still difficult to achieve a microstrip EBG structure with a reasonable performance in both the passband and the stopband.

The stopband characteristics can be created alternatively by using slots etched on the ground plan. By an appropriate choice of the slot dimensions, the isolation level and the stopband bandwidth are controlled. Loading the slots with metal can greatly reduce their sizes. In this section, several metal-loaded slot configurations are proposed and theoretically investigated.

Fig. 3.11 is a schematic of a $50\,\Omega$ microstrip line, incorporating metal-loaded slots of various shapes, etched on the ground plane. All the slots possess the same length (L) of 60mils and width (W) of 240mils. A 25mil-thick substrate with a dielectric constant of 10.2 is selected for all the cases. These metal-loaded slots resemble multi-ridge waveguide and T-septa waveguide structures, which are known to have lower cutoff frequencies.

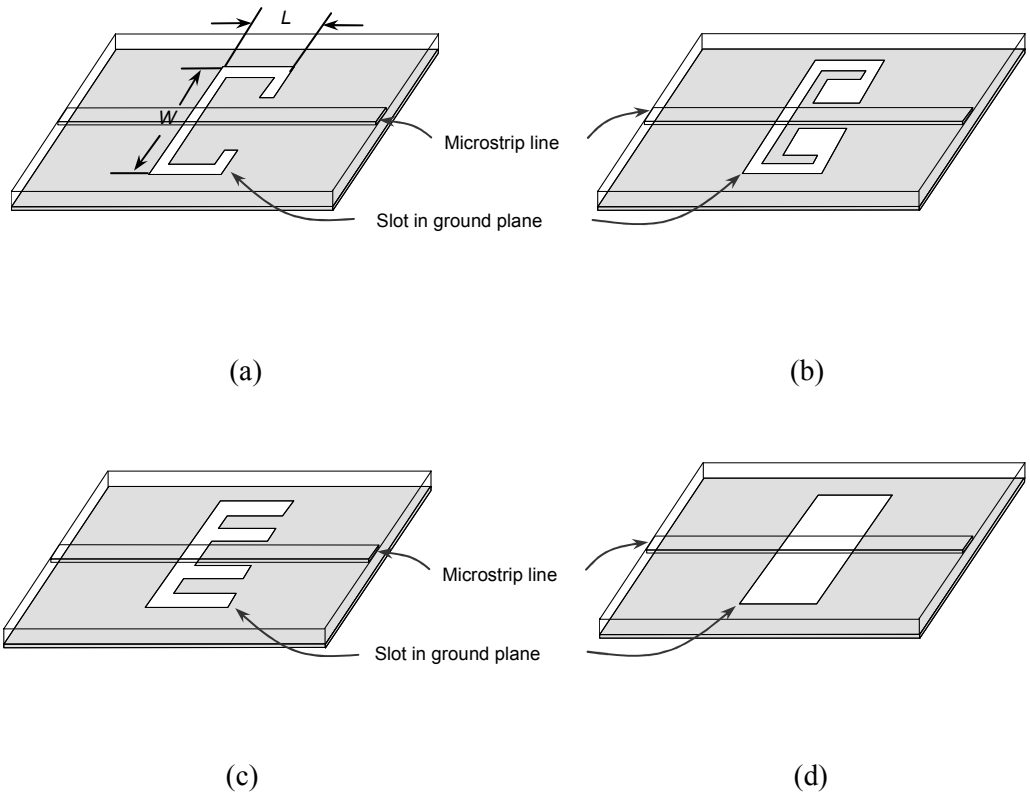

Fig. 3.11 Schematics of slots with various shapes etched on the ground plane: (a), (b), and (c) metal-loaded slots, and (d) rectangular slot.

Fig. 3.12 illustrates the corresponding EM simulation results of the four slot configurations of Fig. 3.11. All the results demonstrate cut-off frequencies and resonant frequencies which act as stopbands. The results clearly indicate that metal-loaded slots can shift the resonant frequency down by more than 50%. Such a shift in frequency can translate to a size reduction in the width of the slots. With the use of the resonant frequency of the rectangular slot as a reference, the width of the metal loaded slots is reduced to give the same resonant frequency. The results are given in Fig. 3.13. When they are compared with the result of the rectangular slot in Fig. 3.11 (d), the width of slots (a), (b), and (c) is reduced by 53%, 68%, and 45%, respectively. Additionally, metal-loaded slots present much steeper cutoff characteristics, which is desirable in filter design, shown in Fig. 3.12 and Fig. 3.13. It is also noticed that the metal-loaded slots with different shapes and dimensions lead to a different bandwidth in the stopband; that is, the rectangular slot in Fig. 3.11 (d) exhibits the largest bandwidth in the stopband, whereas the corrugated slot in Fig. 3.11 (c) and the folded slot in Fig. 3.11 (a) demonstrate smaller stopband bandwidths. The slot configurations in Fig. 3.11 (a) and Fig. 3.11 (c) are investigated to comprehend the effects of the slots' physical parameters on overall performance.

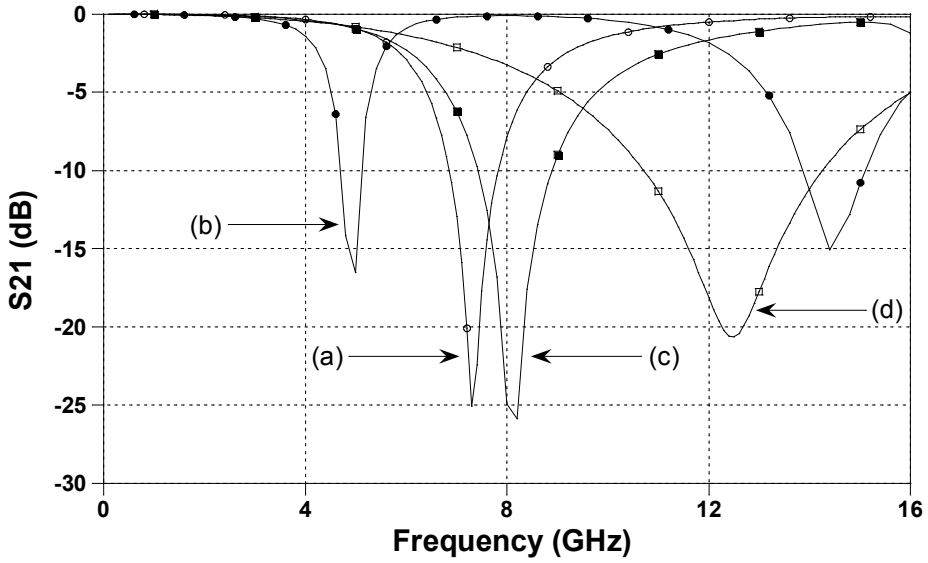

Fig. 3.12 Simulated *S*-parameters of the metal-loaded slots (a), (b), (c), and rectangular slot (d) in Fig. 3.11.

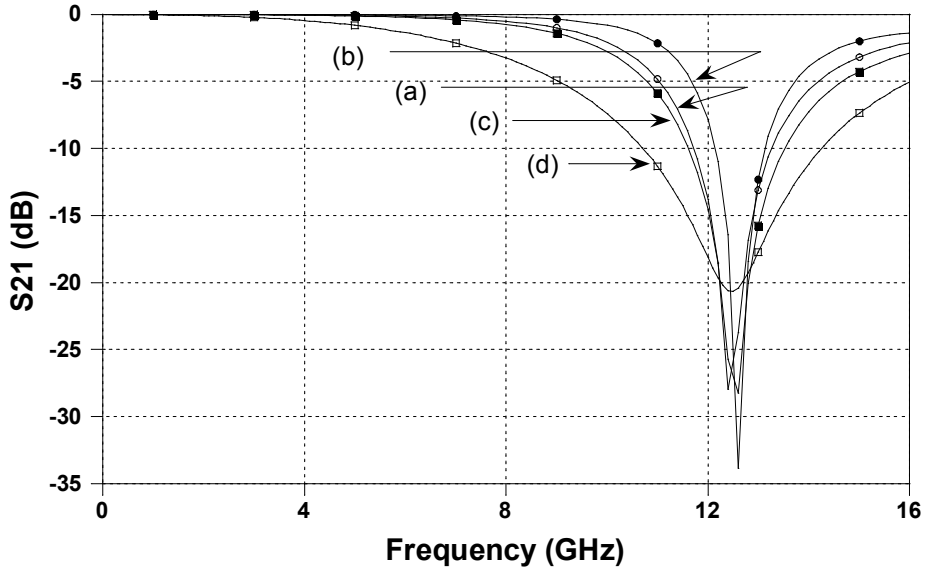

Fig. 3.13 Simulated *S*-parameters of the metal-loaded slots: (a) W = 112mils, (b) W = 76mils, (c) W = 134mils, and the rectangular slot (d) W = 240mils with the same resonant frequency.

3.4.1 Corrugated Slots

Fig. 3.14 displays a schematic of a 50 Ω microstrip line with a corrugated slot etched on the ground plane. The optimal position for the slot is found to be where its centre is located, immediately under the microstrip line. This position maximizes the interaction between the microstrip line and the slot. The comparative EM simulation results with the various physical dimensions of the slots are illustrated in Fig. 3.15. It is evident that increasing the slot width with a fixed slot length lowers the stopband frequency. On the contrary, increasing the slot length with a fixed slot width increases the stopband frequency and broadens the stopband. The performance of the corrugated slot configuration can be controlled and further improved by adjusting dimensions a and d of the corrugation.

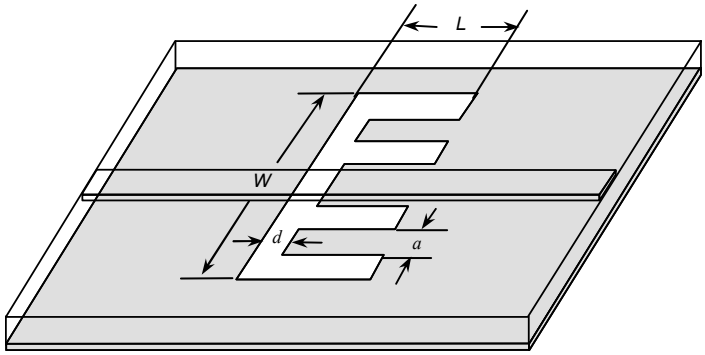

Fig. 3.14 Schematic of a corrugated slot etched on the ground plane.

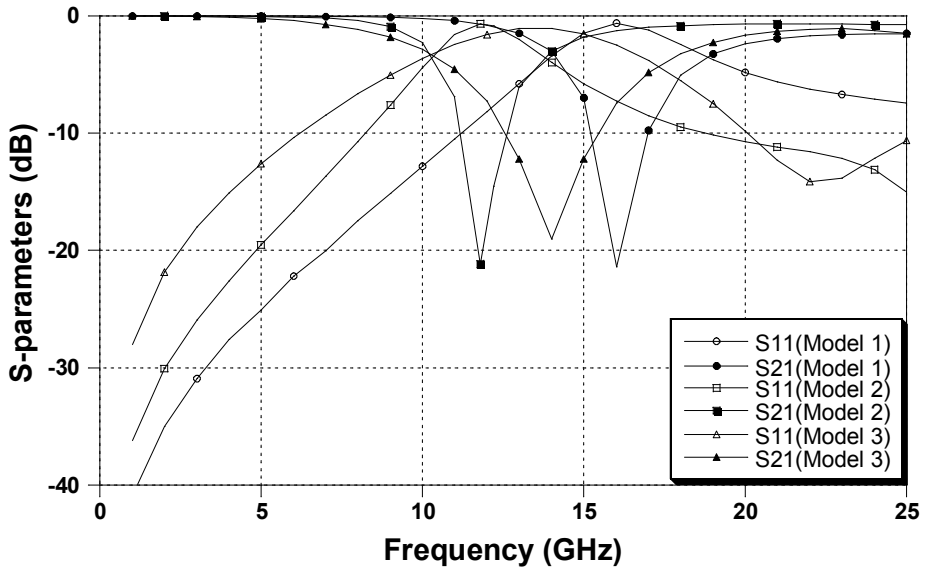

Fig. 3.15 Simulated *S*-parameters for different length *L* and width *W* of the corrugated slots (0.5mm-thick substrate with a dielectric constant of 24); Model 1: *L* = 0.2mm, *W* = 2.4mm; Model 2: *L* = 0.2mm, *W* = 3.4mm; Model 3: *L* = 1.0mm, *W* = 3.4mm.

3.4.2 Folded Slots with T-Shaped Metal-Loading

Fig. 3.16 provides a schematic of a $50\,\Omega$ microstrip line with a folded slot with a T-shaped metal-loading etched on the ground plane. The resonant frequency of the structure is determined by the two factors reflected in Fig. 3.16: gap distance g and area (i.e., $a \times b$) of the T-shaped metal-loading. The influence on the resonant frequency from the gap distance is investigated by varying the value of g (e.g., 60mils, 120mils, and 180mils) while keeping the area of the metal-loading a constant ($a \times b$ = 40mils × 220mils). EM simulation results in Fig. 3.17 indicate that the resonant frequency increases from 6.2GHz to 7.8GHz with a tuning range of 1.6GHz as the gap distance increases.

To study the effect of the metal-loading dimensions on the resonant frequency, $a \times b$ is varied with a fixed gap distance of 120mils. The corresponding EM simulation results in Fig. 3.18 indicate that the larger the area of the metal-loading, the lower the resonant frequency. The resonance in this case increases from 6.2GHz to 8.2GHz with a tuning range of 2GHz. Therefore, by choosing suitable dimensions of the folded slots, the performance of the microwave circuit, employing this kind of structure, is easily controlled.

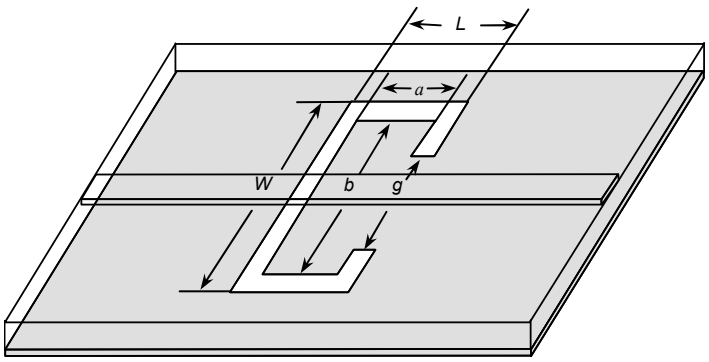

Fig. 3.16 Schematic of a folded slot with T-shaped metal-loading etched on the ground plane.

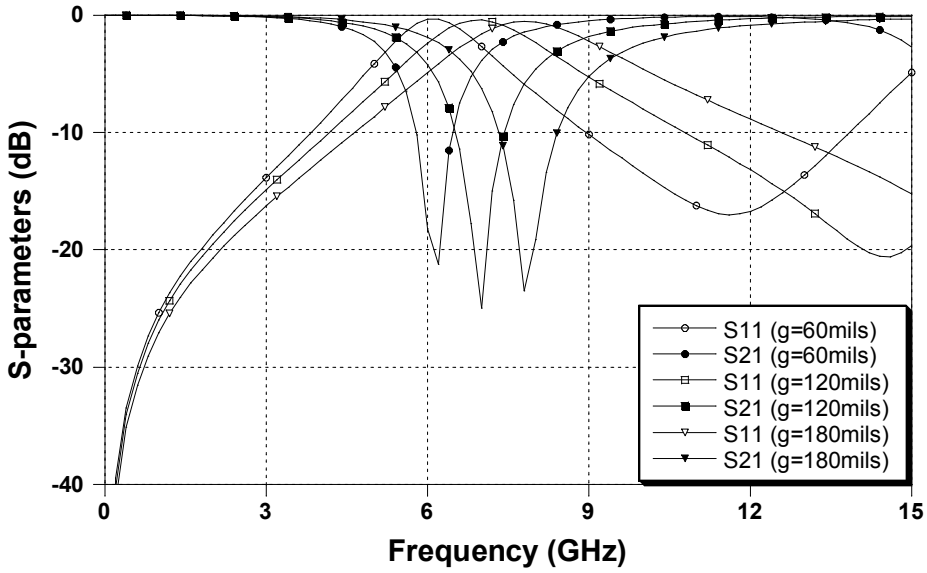

Fig. 3.17 Simulated *S*-parameters of the folded slot resonators; gap distance g is 60mils, 120mils, and 180mils, respectively; area of T-shaped metal-loading $a \times b$ is 40mils × 220mils for all cases.

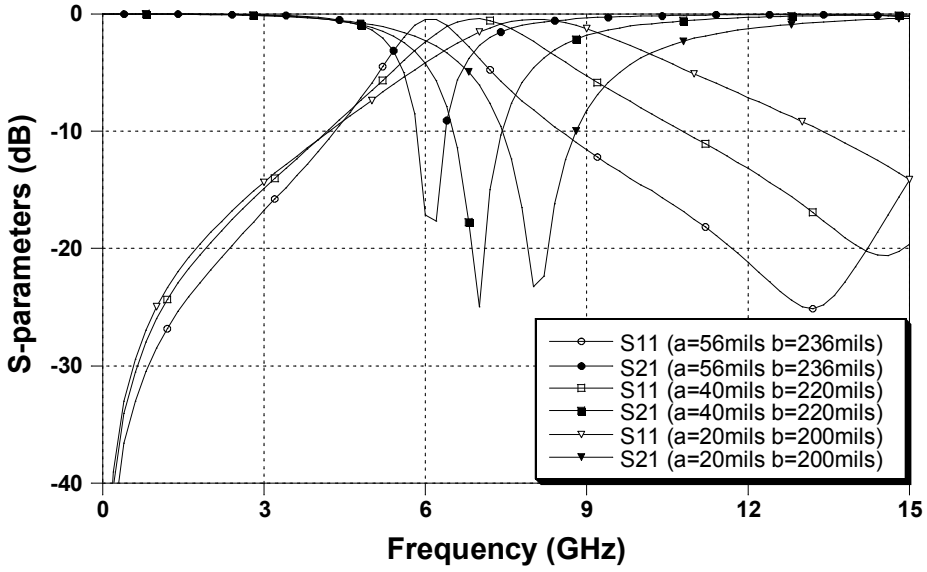

Fig. 3.18 Simulated *S*-parameters of the folded slot resonators; area of T-shaped metal-loading $a \times b$ is 56mils × 236mils, 40mils × 220mils, and 20mils × 200mils, respectively; gap distance g is 120mils for all cases.

3.5 Modelling of the Folded Slot Resonators with T-Shaped Metal-Loading

Although the EM simulations are rigorous and accurate, they require a substantial computational effort. To achieve a fast and accurate analysis of the proposed folded slot resonators, a simple and efficient model is developed.

3.5.1 Transmission Line Circuit Model

Consider the folded slot resonator in Fig. 3.16 as an example. A transmission line circuit model is developed, and the corresponding circuit diagram is illustrated in Fig. 3.19.

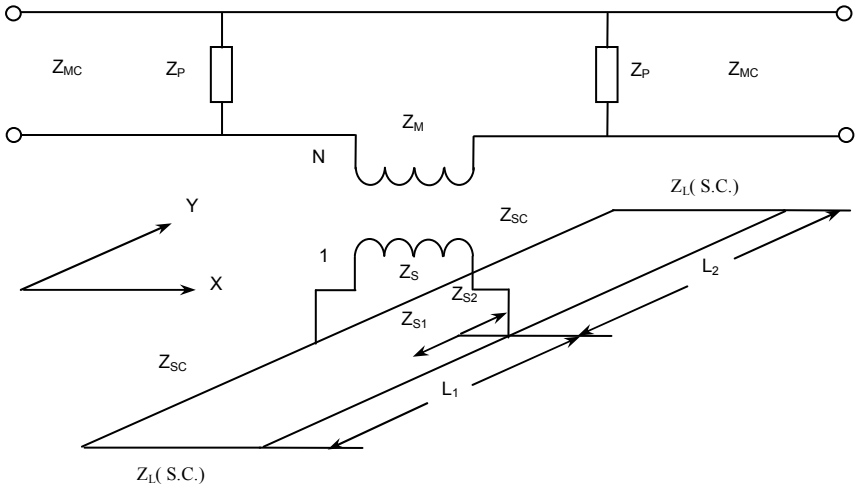

Fig. 3.19 Transmission line circuit model of the folded slot resonator shown in Fig. 3.16.

In this model, the folded slot is considered as two individual short-circuited slot lines underneath the microstrip line. The coupling between the microstrip line and the slot line is represented by a voltage transformer. Transformer ratio N is [60, 61]

$$N = \frac{V(h)}{V_0}, \tag{3.13}$$

where V_0 is the voltage across the slot, and h is the thickness of the dielectric substrate. $V(h)$ is calculated by

$$V(h) = -\int_{-L_C/2}^{L_C/2} E_x(h)dx\,, \tag{3.14}$$

where $E_x(h)$ is the electric field of the slot line on the dielectric surface on the opposite side, and L_C is the length of the coupling section of the microstrip to the slot line. Therefore [61, 62],

$$E_x(h) = -\frac{V_0}{L_C}\left\{\cos\left(\frac{2\pi h}{\lambda_0}u\right) - \cot(q_0)\sin\left(\frac{2\pi h}{\lambda_0}u\right)\right\}, \tag{3.15}$$

where

$$q_0 = \frac{2\pi h}{\lambda_0}u + \tan^{-1}\left(\frac{u}{v}\right), \tag{3.16}$$

$$u = \sqrt{\varepsilon_r - \left(\frac{\lambda_0}{\lambda_{sg}}\right)^2}\,, \tag{3.17}$$

and

$$v = \sqrt{\left(\frac{\lambda_0}{\lambda_{sg}}\right)^2 - 1}\,. \tag{3.18}$$

ε_r is the dielectric constant, λ_0 is the free-space wavelength, and λ_{sg} is the guided wavelength of the slot line. Once the characteristic impedance of slot line Z_{SC} and slot wavelength λ_{sg} are obtained from the closed-form expressions in [63], slot impedance Z_S at the input of the two short-circuited slot lines, with a length of L_1 and L_2, can be easily calculated to be $Z_S = Z_{S1} \,||\, Z_{S2}$, where

$$Z_{Si} = Z_{SC}\left.\frac{Z_L + jZ_{SC}\tan(\frac{2\pi}{\lambda_{sg}}\cdot L_i)}{Z_{SC} + jZ_L\tan(\frac{2\pi}{\lambda_{sg}}\cdot L_i)}\right|_{Z_L=0} \quad (i = 1,2). \tag{3.19}$$

Z_{S1} and Z_{S2} are the input impedance of the two slot lines in parallel, respectively, underneath the microstrip line. The impedance of the loading Z_L is zero, because the two slot lines are short circuited. The length of L_2 is equal to L_1 in Fig. 3.16, and the value of the series impedance Z_M in the π-equivalent circuit is

$$Z_M = N^2 Z_S . \tag{3.20}$$

It is noteworthy that shunt impedance Z_P of the π-network is infinity (i.e., open circuit) when the slot is perpendicular to the microstrip line [64]. The *S*-parameters of the slot resonators are obtained as a function of the physical dimensions, dielectric characteristics and frequencies. Fig. 3.20 graphs the simulation results of the folded slot resonator in Fig. 3.16, based on the previous model. The proposed model provides results that are in good agreement with those of the EM simulation which is also shown in Fig. 3.20. Therefore, the derived equivalent transmission line circuit model for the folded slot resonator is shown to be a direct and an efficient method for designing practical circuits.

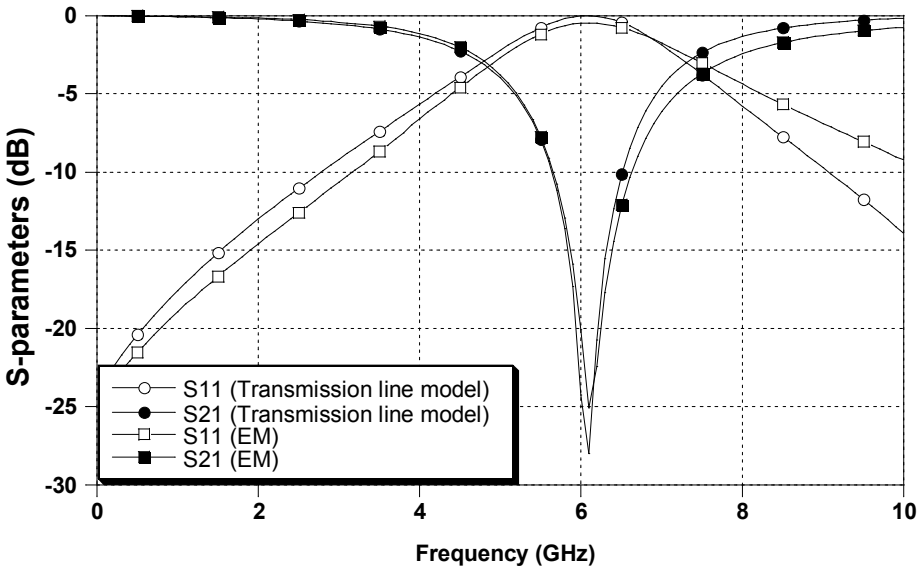

Fig. 3.20 Comparison of the *S*-parameters of the folded slot resonator shown in Fig. 3.16 from the transmission line circuit model (Fig. 3.19) and the EM simulation.

3.5.2 *RLC* Lumped-Element Circuit Model

It is also quite straightforward to think of using a *RLC* lumped-element circuit model to explain the observed resonance characteristic of the folded slot resonator in Fig. 3.16, since the *RLC* circuit is able to generate such a resonance [12]. The introduction of the *RLC* circuit for the analysis and simulation facilitates the synthesis of more complicated microwave circuits by using a lowpass prototype. The *RLC* lumped-element circuit model is displayed in Fig. 3.21, and is capable of representing the first and second resonance for the folded slot resonators of Fig. 3.16.

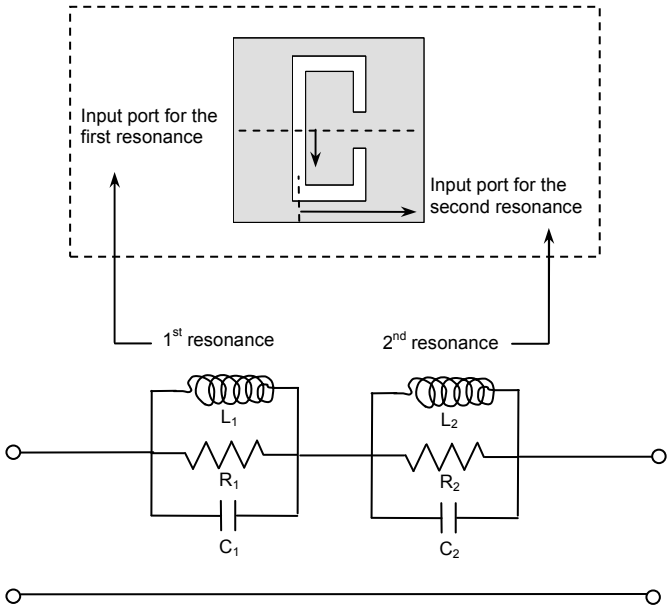

Fig. 3.21 *RLC* lumped-element circuit model of the folded slot resonator in Fig. 3.16.

The lumped-element parameters of the *RLC* circuit are extracted by using an optimization program [65] either from the simulation results of the proposed transmission line circuit model or EM simulator. *R*, *L*, and *C* are derived as [66]

$$R = 2Z_0 \left(\frac{1}{|S_{21}|} - 1\right)\Bigg|_{\omega=\omega_0}, \tag{3.21}$$

$$C = \frac{\sqrt{a^2(R+2Z_0)^2 - 4Z_0^2}}{2Z_0 R\sqrt{1-a^2}(\omega_2 - \omega_1)}, \tag{3.22}$$

and

$$L = (\omega_0^2 C)^{-1}, \tag{3.23}$$

where Z_0 is the characteristic impedance of the slot transmission line, ω_0 is the resonant angle frequency, and $S_{21} = a$ at $\omega = \omega_1 = \omega_2$. For the folded slot resonator in Fig. 3.16, the lumped-element parameters are computed as $R_1 = 3300\,\Omega$, $R_2 = 400\,\Omega$, $C_1 = 0.85$pF, $C_2 = 0.65$pF, $L_1 = 0.82$nH, and $L_2 = 0.154$nH. A comparison between the results of the *RLC* lumped-element circuit model in Fig. 3.21 and those of the EM Simulation is given in Fig. 3.22. A good correlation is observed up to 20GHz.

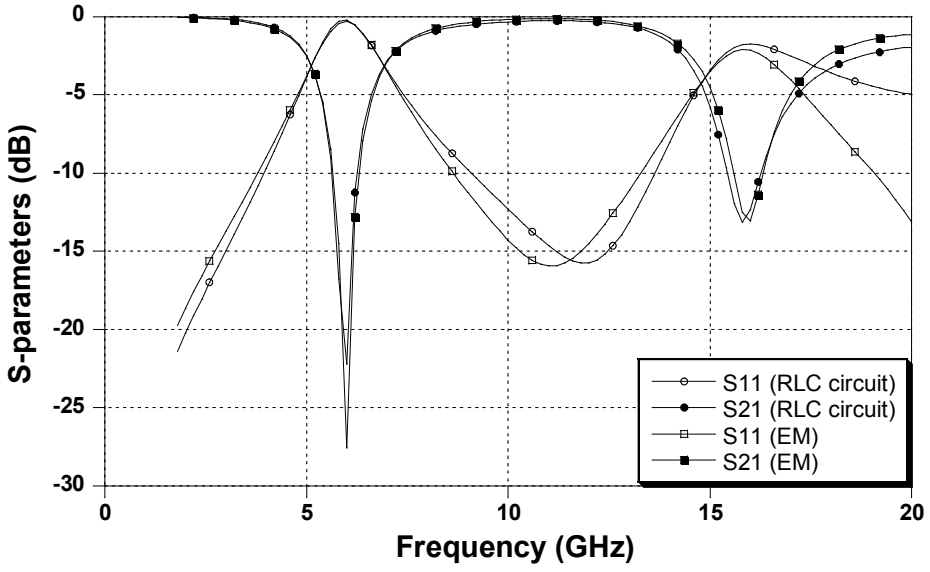

Fig. 3.22 Comparison of the *S*-parameters of the folded slot resonator shown in Fig. 3.16 from the *RLC* lumped-element circuit model (Fig. 3.21) and the EM simulation.

The stopband generated by a single slot is not broad enough to satisfy the practical requirements. One way to achieve this goal is to cascade a few slots that can create multiple stopbands. If these stopbands are close enough together, a wide stopband is obtained [67]. It is more flexible to use cascaded slot resonators than conventional periodic EBG structures, because the length and the width of the slots, and the distance between the two adjacent slots can easily vary, and well meet the design specifications.

3.6 Applications of the Folded Slot Resonators in Filter Designs

The proposed folded slot resonators can be used for implementing bandstop filters, lowpass filters, and bandpass filters.

3.6.1 Bandstop Filters

Higher order bandstop filters can be achieved by cascading a specific number of the folded slot resonators. The circuit models in Fig. 3.19 and 3.21 are applied to calculate the frequency characteristics for, not only one slot resonator, but also, several cascaded slot resonators. With the use of these models, the simulation time is significantly reduced, achieving the results that are in agreement with those of the EM analysis. A general synthesis approach is employed in bandstop filter designs.

A third-order microstrip bandstop filter with folded slot resonators is shown in Fig. 3.23. Three slot resonators, with the same or different dimensions, are spaced a quarter guided wavelength apart. Only the first resonance of each slot without any losses (i.e., no R shows up in Fig. 3.21) is taken into account for the synthesis. By using an admittance inverter for the quarter-wavelength microstrip line and shunt LCs to represent the three slot resonators respectively, an equivalent circuit for the third-order bandstop filter is obtained, as depicted in Fig. 3.24. Here Y_0 is the terminating admittance, and Y_u denotes the characteristic admittance of the inverter.

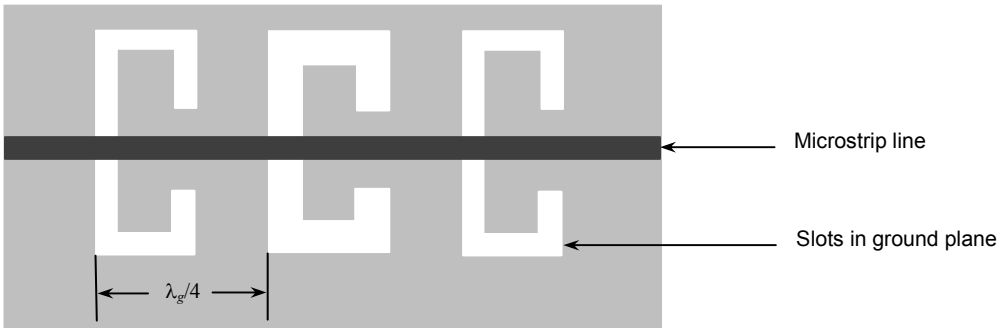

Fig. 3.23 Third-order microstrip bandstop filter using folded slot resonators (top view).

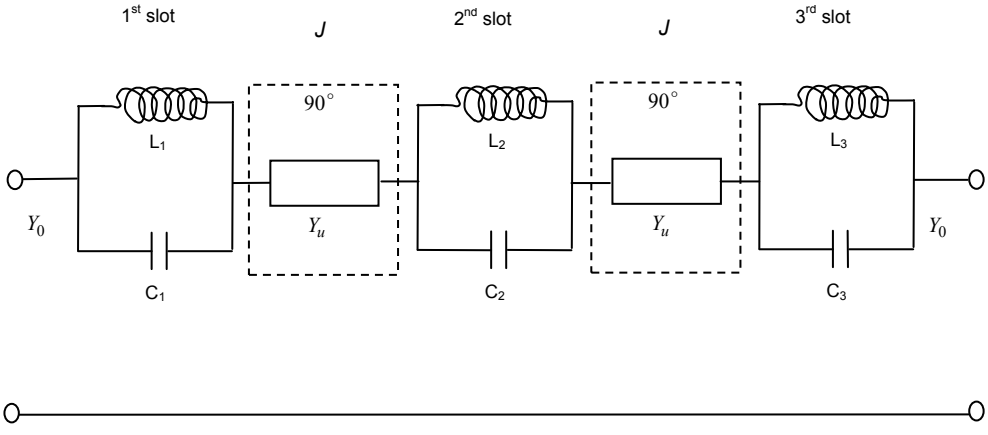

Fig. 3.24 Equivalent circuit of the third-order microstrip bandstop filter shown in Fig. 3.23.

All the circuit parameters are easily calculated in terms of lowpass prototype elements as follows [68]:

$$\left(\frac{Y_u}{Y_0}\right)^2 = \frac{1}{g_0 g_{N+1}}, \tag{3.24}$$

$$C_i = Y_0\left(\frac{Y_u}{Y_0}\right)^2 \frac{g_0}{g_i \Omega_c FBW \omega_0} \qquad i = 1 \text{ to } N, \tag{3.25}$$

and

$$L_i = (\omega_0^2 C_i)^{-1} \qquad i = 1 \text{ to } N, \tag{3.26}$$

where $N = 3$ in the case of the third-order filter, ω_0 is the resonant frequency of each slot resonator, $FBW = \frac{\omega_2 - \omega_1}{\omega_0}\Big|_{\omega_0 = \sqrt{\omega_1 \omega_2}}$ is the fractional bandwidth of the bandstop filter, and g_i are the element values of lowpass prototype. For example, in order to achieve a bandstop filter with a fractional bandwidth of 1.15 and resonant frequency of 6.9GHz, third-order lowpass Chebyshev prototype elements of $g_0 = g_4 = 1$, $g_1 = g_3 = 0.6292$, and $g_2 = 0.9703$ with a passband ripple level of 0.01dB, are used. The corresponding inductances L_i and capacitances C_i, in Fig. 3.24, are obtained from Eq. (3.24) to (3.26) as the following: $C_1 = C_3 = 0.632$pF, $L_1 = L_3 = 0.835$nH, $C_2 = 0.410$pF, and $L_2 = 1.287$nH.

The physical dimensions of the filter can be determined from these inductance and capacitance values, based on the proposed transmission line circuit model, demonstrated in Fig. 3.19. It is observed from the synthesis that the first and the third slot resonator should be identical, whereas the middle slot should possess the different dimensions. The conclusion from the observation is that the bandstop filters, based on conventional microstrip EBG structures can never attain the optimal design, since the EBG units must be identical to each other. Fig. 3.25 shows the simulated frequency responses of the designed filter. The synthesis results are in good agreement with the EM simulations for the designed bandstop filter are presented.

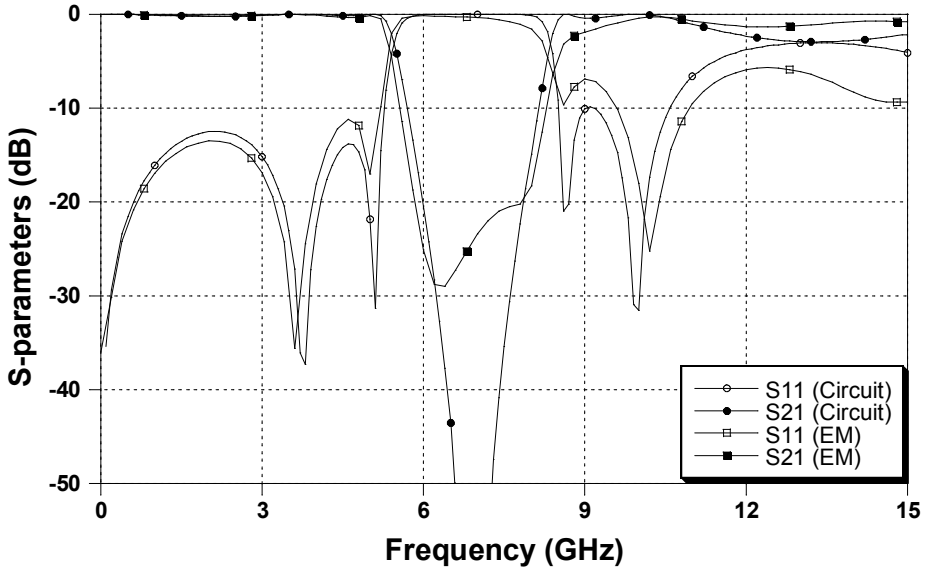

Fig. 3.25 Comparison of the *S*-parameters of the third-order microstrip bandstop filter using folded slot resonators shown in Fig. 3.23 from the equivalent circuit (Fig. 3.24) and the EM simulation.

3.6.2 Lowpass Filters

Since a single folded slot resonator presents both the cutoff (lowpass) and the resonance (bandstop) characteristic, microstrip lowpass filters can also be realized by cascading a specific number of such slot resonators. The stopband widens in relation to the increased number of slots, leading to a lowpass filter.

3.6.2.1 Designs of the Lowpass Filters

To compare, Fig. 3.26 represents three filter configurations, where one employs rectangular slots, and the other two employ folded slots. Non-uniform folded slots are used in one of these filters to optimize its passband-stopband characteristics. The EM simulation results for the isolation and the return loss of the three filters are signified in Fig. 3.27. It is

obvious that with the identical width (L) and the same periodicity (D), the microstrip filter with non-uniform folded slots presents the widest stopband of 5GHz, the lowest return loss at -18dB, and a lower cutoff frequency of 5.5GHz. Thus, the use of microstrip structures with non-uniform folded slots yields a compact design with an improved performance in both the passband and stopband.

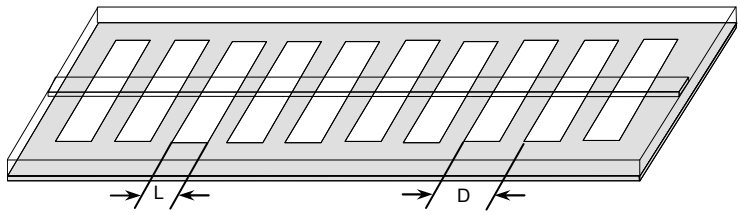

(a)

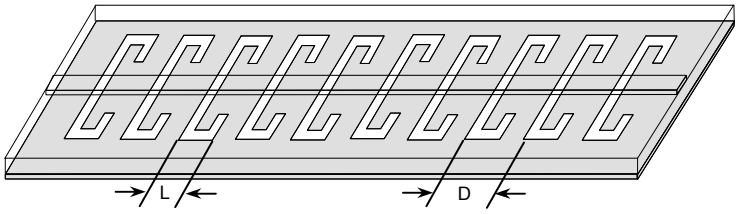

(b)

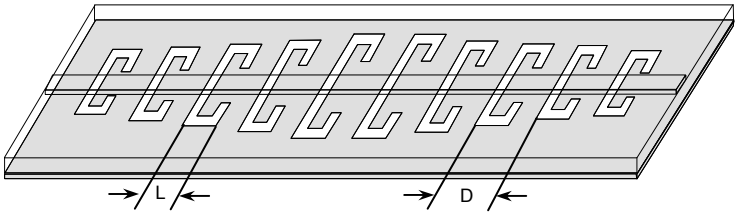

(c)

Fig. 3.26 Microstrip lowpass filters employing slots etched on ground plane: (a) rectangular slots, (b) uniform folded slots, and (c) non-uniform folded slots.

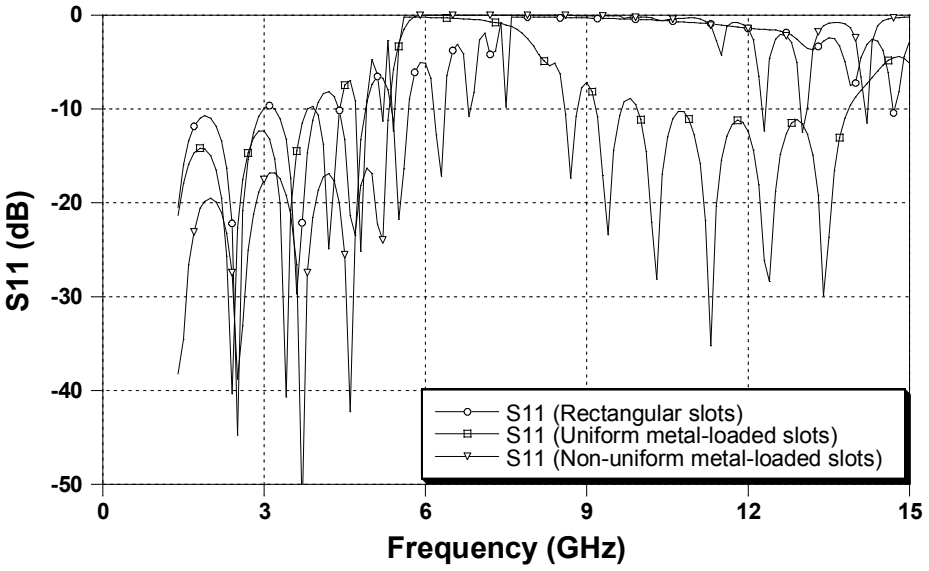

(a)

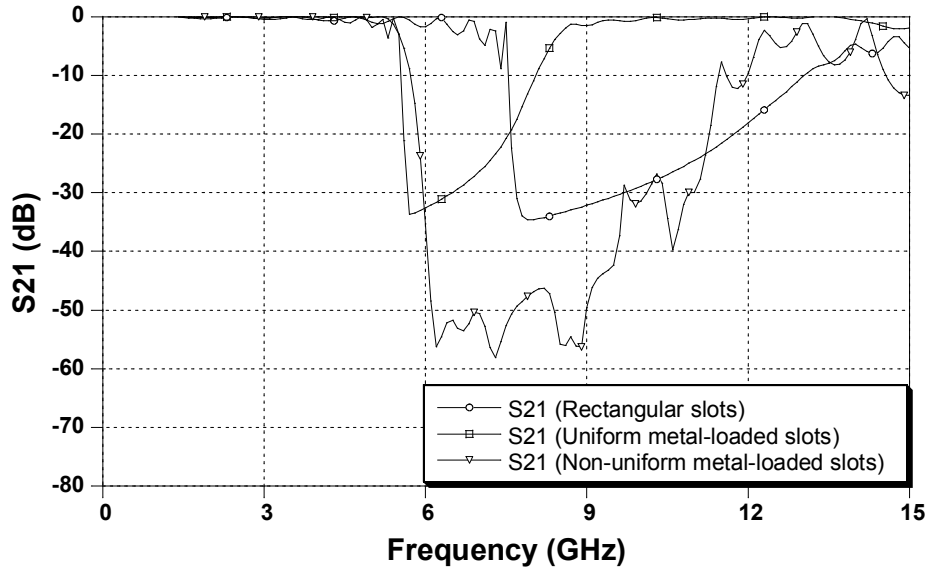

(b)

Fig. 3.27 EM simulation results of the microstrip lowpass filters with slots etched on the ground plane shown in Fig. 3.26: (a) S_{11} and (b) S_{21}.

To design and optimize microstrip lowpass filters with non-uniform folded slots, *RLC* lumped-element circuit models for single slots, demonstrated in Fig. 3.21, are chosen to construct and optimize the circuit model for the entire filter. The periodicity of the slots is $\lambda_g/4$ (λ_g is the guided-wavelength) at the centre frequency in stopband, which is half the spacing required for that of traditional EBG-based microstrip filters. The initial synthesis and design of the lowpass filters is based on a traditional lowpass filter design technique [69]. Yet, other modifications are carried out by using the proposed circuit model to optimize the filter performance. After the optimized circuit simulation results are obtained, an EM simulator is used to verify and fine tune the filter performance. The dimensions of the folded slots are adjusted to achieve the optimal performance of the lowpass filters.

Fig. 3.28 shows photographs of one of the fabricated microstrip lowpass filters with non-uniform folded slots, etched on the ground plane. Fig. 3.29 depicts both the *RLC* lumped-element circuit simulation and EM simulation of the designed microstrip lowpass filter. The experimental results for the fabricated filter are given in Fig. 3.30. As seen, a wide stop bandwidth and a significant improvement of the passband characteristics are achieved. Fig. 3.31 shows a photograph of another fabricated microstrip lowpass filter with non-uniform folded slots, etched on the ground plane, and the measured results are denoted in Fig. 3.32.

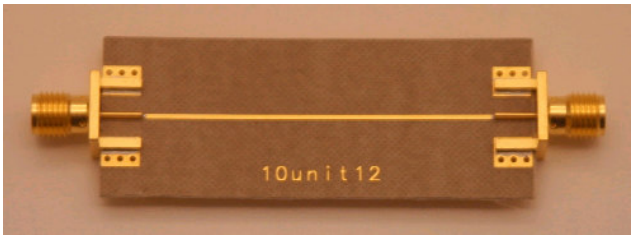

(a)

(b)

Fig. 3.28 Fabricated microstrip lowpass filter with non-uniform folded slots etched on the ground plane: (a) top view and (b) bottom view.

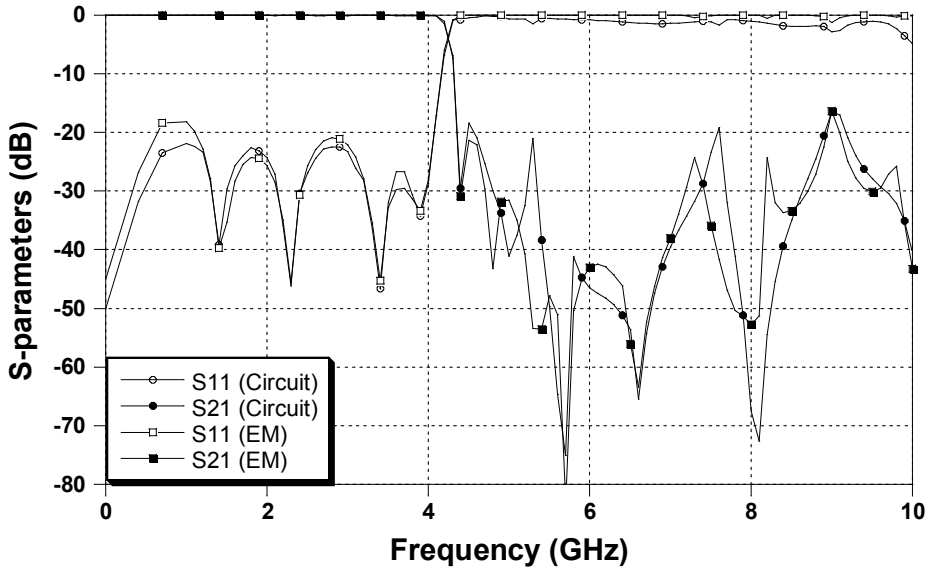

Fig. 3.29 Comparison of the *S*-parameters of the designed microstrip lowpass filter shown in Fig. 3.28 from the *RLC* lumped-element circuit model and the EM simulation.

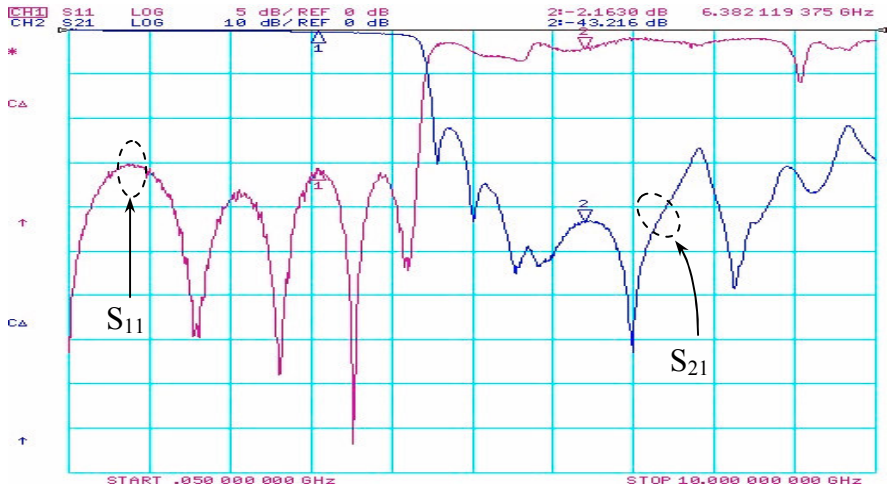

Fig. 3.30 Measurement results of the designed microstrip lowpass filter shown in Fig. 3.28.

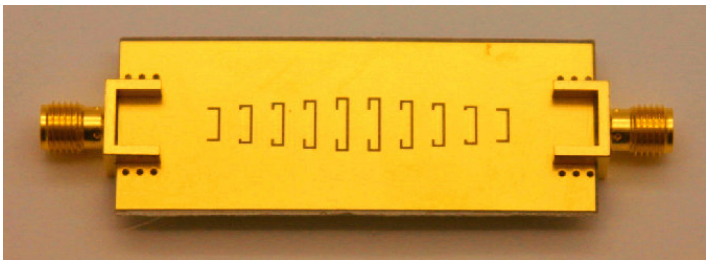

Fig. 3.31 Fabricated microstrip lowpass filter with non-uniform folded slots etched on the ground plane (bottom view).

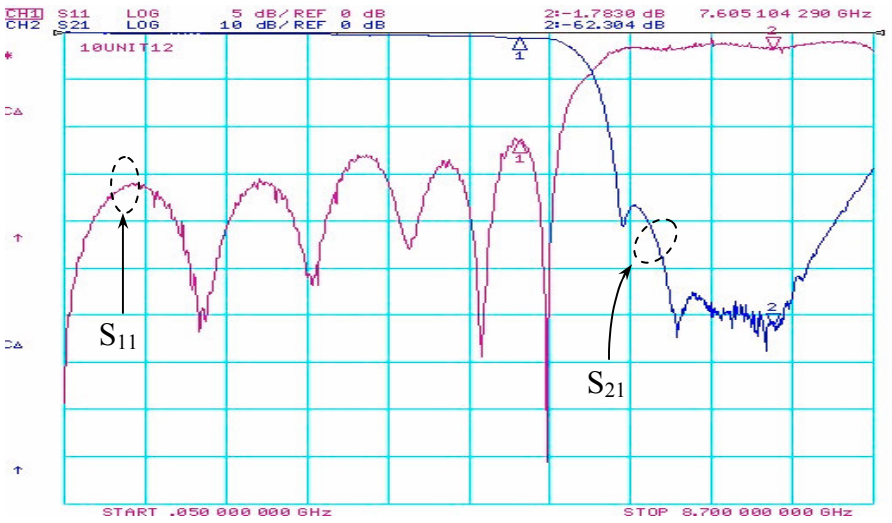

Fig. 3.32 Measurement results of the designed microstrip lowpass filter shown in Fig. 3.31.

Fig. 3.33 is a bottom view of the third fabricated microstrip lowpass filter which uses folded slots with a double-sided metal-loading. The advantage of such a filter is that it presents a lower cutoff frequency than a filter with the same dimensions, but employs folded slots with a one-side metal-loading. The filter can become more compact, and the same approach and procedure are performed to design the filter in Fig. 3.33. Both the EM simulation and experimental results for the fabricated filter are given in Fig. 3.34, which exhibits a good RF performance in both the passband and the stopband.

Fig. 3.33 Fabricated microstrip lowpass filter using folded slots with double-sided metal-loading (bottom view).

3.6.2.2 Applications of the Lowpass Filters

The novel compact microstrip lowpass filters, demonstrated in Section 3.6.2.1, have an insertion loss close to that of a 50Ω transmission line of the same length. They are useful in applications that require the suppression of out-of-band interference signals. Fig. 3.35 shows a schematic of a 5-pole microstrip bandpass filter operating at 7GHz. The dielectric substrate is 25mil-thick with a dielectric constant of 10.2. The EM simulation results are demonstrated in Fig. 3.36, which shows the first spurious mode located at 15GHz.

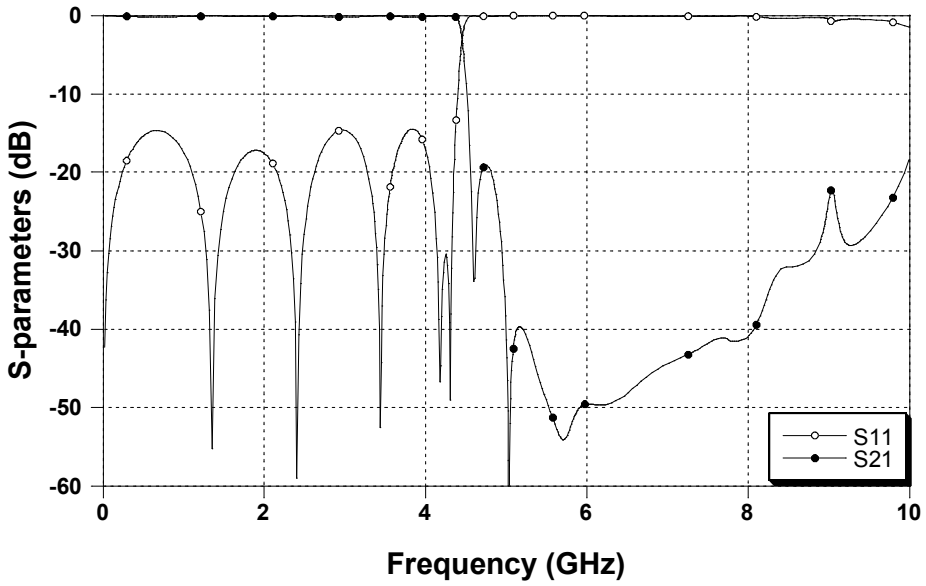

(a)

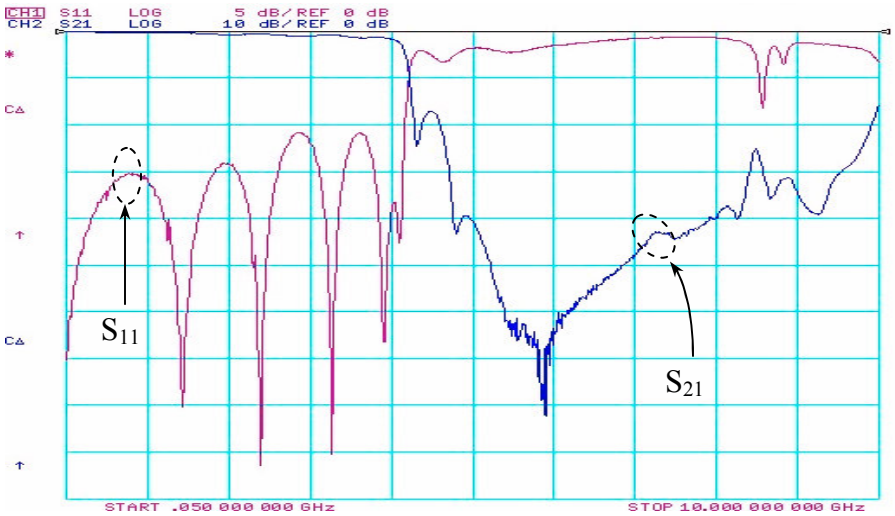

(b)

Fig. 3.34 Frequency responses of the designed microstrip lowpass filter shown in Fig. 3.33: (a) EM simulation and (b) measurement.

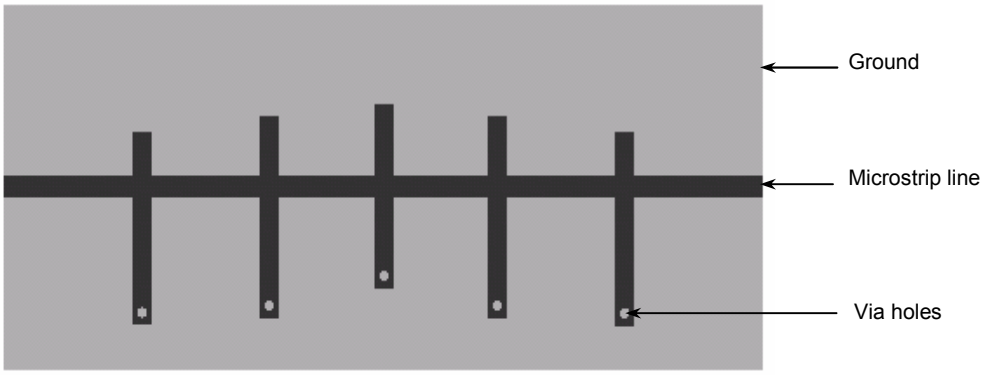

Fig. 3.35 Schematic of the 5-pole microstrip bandpass filter (top view).

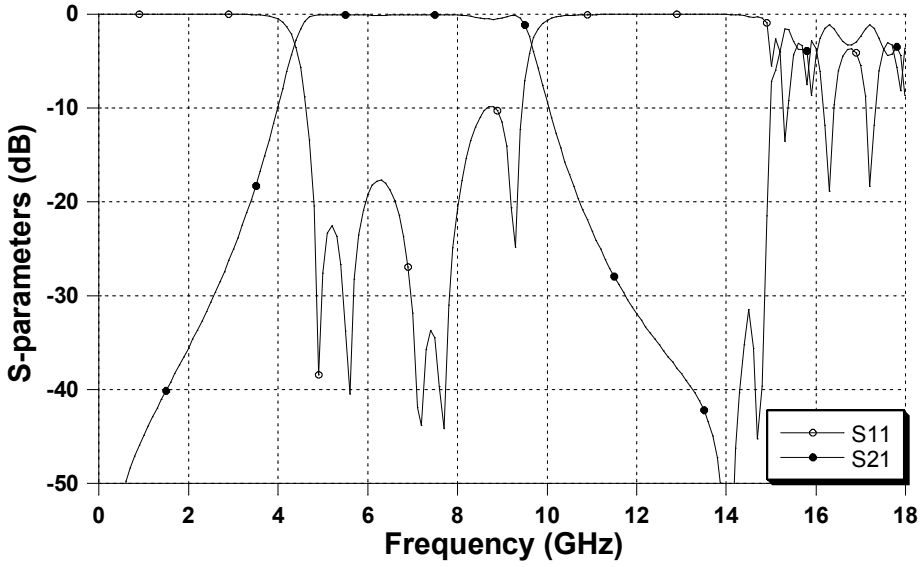

Fig. 3.36 Simulated frequency responses of the designed microstrip bandpass filter shown in Fig. 3.35.

Typically, the approach to reduce or eliminate the undesired spurious mode is to cascade the bandpass filter with a lowpass filter whose cutoff frequency is designed at approximately 15GHz. The integration of the bandpass filter and the lowpass filter, shown in Fig. 3.37, leads to a 20dB reduction of the spurious mode that is indicated in Fig. 3.38.

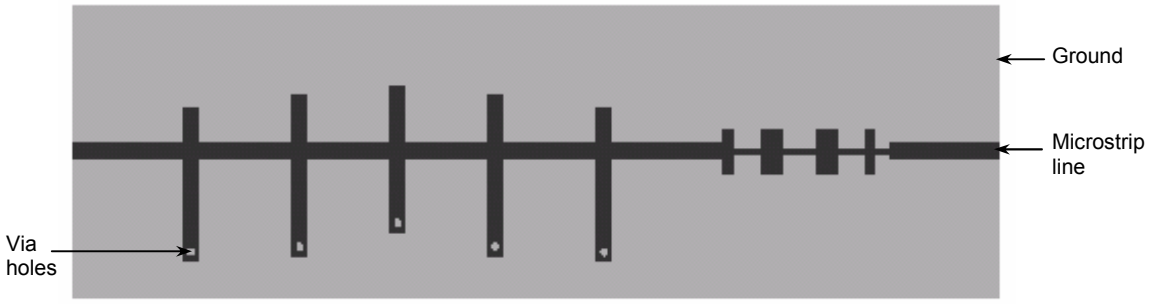

Fig. 3.37 Cascading of the bandpass filter with the lowpass filter (top view).

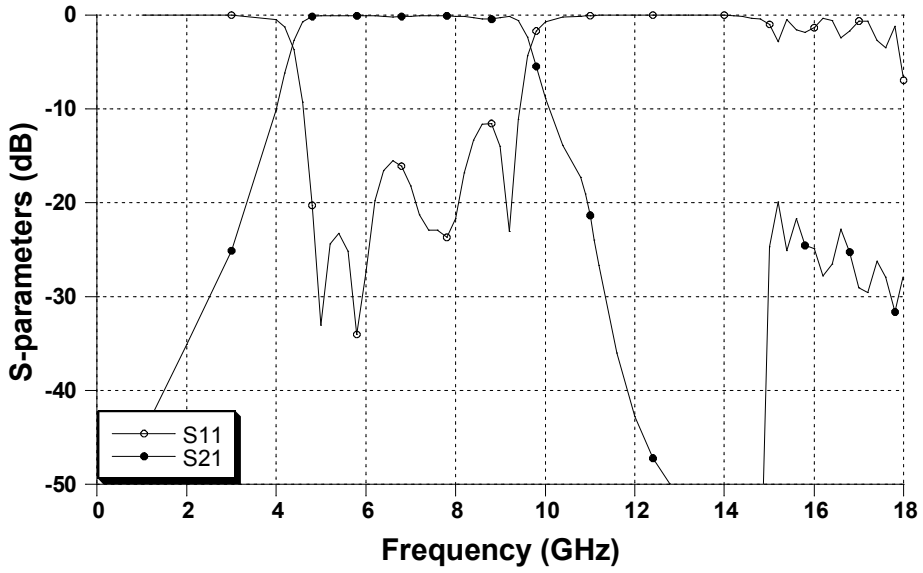

Fig. 3.38 Simulated frequency responses of the microstrip bandpass filter cascading with the lowpass filter shown in Fig. 3.37.

Alternatively, the lowpass filter in Fig. 3.37 can be replaced by the newly developed lowpass filters, demonstrated in Section 3.6.2.1, since such type of lowpass filters are amenable to microstrip structures. Furthermore, the lowpass filter use folded slots etched on the ground plane indicating that they can be placed immediately underneath the bandpass filter, instead of beside it. Thus, the integration of the two filters results in a very compact structure. Fig. 3.39 signifies the integration of the bandpass filter with the lowpass filter using folded slots, and the corresponding simulation results are shown in Fig. 3.40. The 20dB improvement of the spurious mode is achieved.

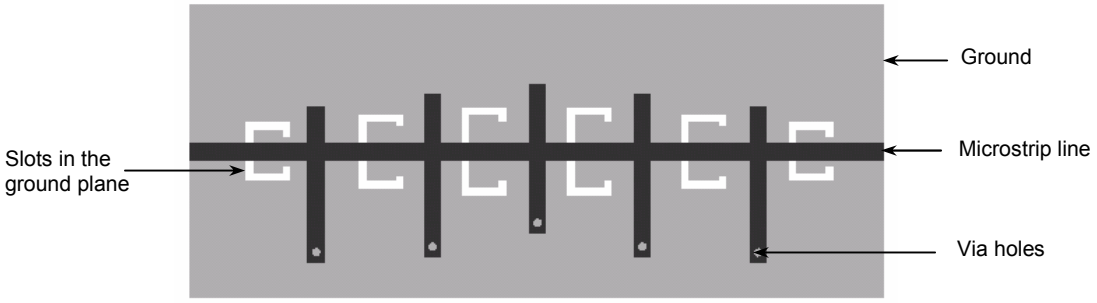

Fig. 3.39 Integration of the bandpass filter with the lowpass filter using folded slots (top view).

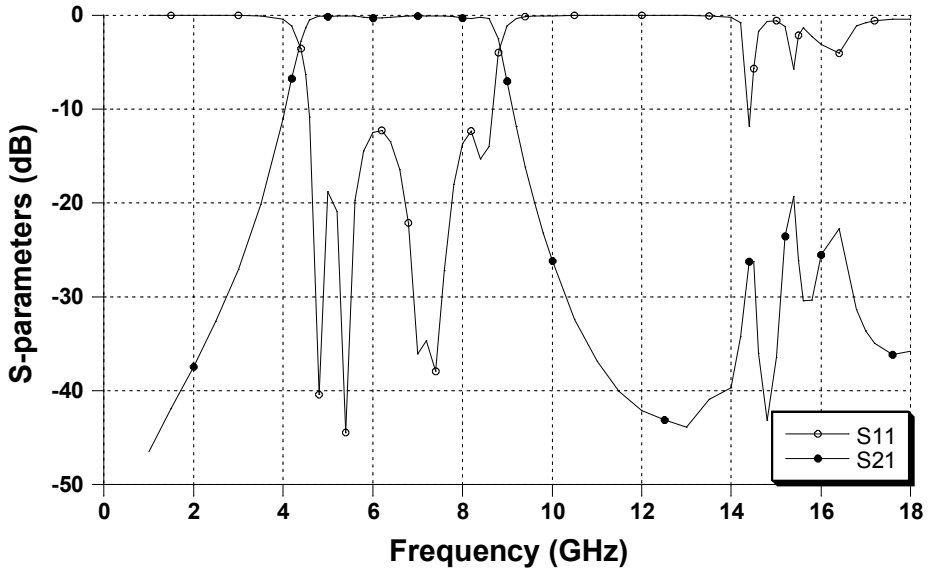

Fig. 3.40 Simulated frequency responses of the integration of the microstrip bandpass filter with the lowpass filter using the folded slots shown in Fig. 3.39.

3.6.3 Bandpass Filters

By introducing a series capacitor to a microstrip transmission line over a folded slot, a resonator demonstrating one attenuation pole and one passband pole is created. Fig. 3.41 demonstrates two possible means to generate a series capacitor over the folded slot.

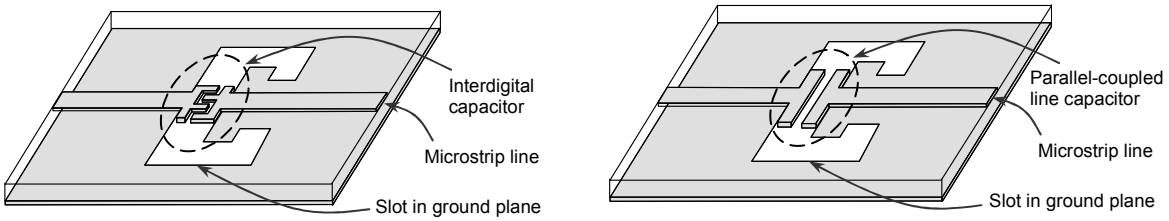

(a) (b)

Fig. 3.41 Schematics of resonators with folded slots etched on the ground plane by using (a) an interdigital capacitor and (b) a parallel-coupled line capacitor.

The introduction of additional series capacitors C_{s1} and C_{s2} to the inductances in Fig. 3.21 leads to the lumped-element circuit model in Fig. 3.42, which can be used to explain the transmission characteristics of the slot resonators in Fig. 3.41.

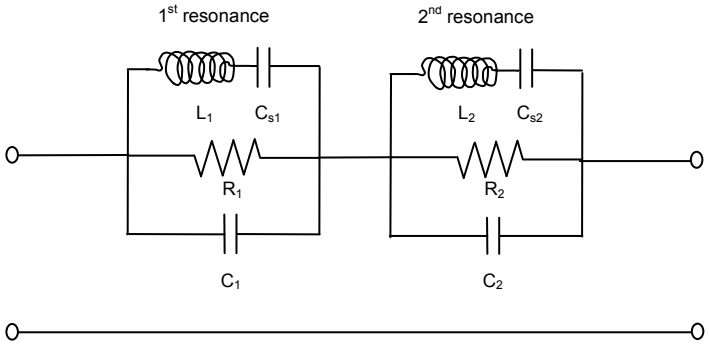

Fig. 3.42 Lumped-element circuit model of the resonators shown in Fig. 3.41.

The equivalent circuit in Fig. 3.42 indicates that the slot resonator has attenuation poles at ω_{0i} (i = 1,2) and passband poles located at ω_{ci} (i = 1,2), regarding the first and second resonance, respectively. R and C are determined by the attenuation poles so that their values can still be obtained from Eq. (3.21) and (3.22). According to the resonant conditions of the slot resonator, the values of C_s and L can be derived as

$$C_{si} = C_i\left(\frac{\omega_{0i}^2}{\omega_{ci}^2} - 1\right) \quad i = 1,2 \tag{3.27}$$

and

$$L_i = (\omega_{ci}^2 C_{si})^{-1} \quad i = 1,2\ . \tag{3.28}$$

Table 3.1 summarizes the physical dimensions (referring the definitions in Fig. 3.16) of the proposed folded slot resonator (Fig. 3.41 (a)) on a 25mil-thick dielectric substrate (ε_r = 10.2) and the corresponding extracted parameters of its lumped-element equivalent circuit. Fig. 3.43 demonstrates a good agreement between the results of the lumped-element circuit model shown in Fig. 3.42 and those of EM Simulations.

Table 3.1 Extracted equivalent circuit parameters for a folded slot resonator in Fig. 3.41 (a).

Dimensions of the Slot	1st Resonance	2nd Resonance
L = 120mils	R_1 = 2000 Ω	R_2 = 180 Ω
W = 240mils	C_1 = 0.20pF	C_2 = 0.61pF
a = 40mils, b = 80mils	L_1 = 2.68nH	L_2 = 0.12nH
g = 120mils	C_{s1} = 0.75pF	C_{s2} = 0.85pF

Bandpass filters can be carried out by cascading a number of the slot resonators, as given in Fig. 3.41. Two adjacent resonators are connected and coupled to each other by a piece of microstrip transmission line. To achieve 2-pole bandpass microstrip filters, two slot resonators are connected by a microstrip line whose length is approximate λ_g /8 (Fig. 3.44). The filters have much a smaller size than that of traditional quarter-wavelength coupled line bandpass filters or filters with half-wavelength capacitively coupled resonators. Also, instead of a narrow passband determined by the strong frequency dependency of the normal line resonator in the bandpass filter design, the slot resonator can be employed to the design of broadband bandpass filters.

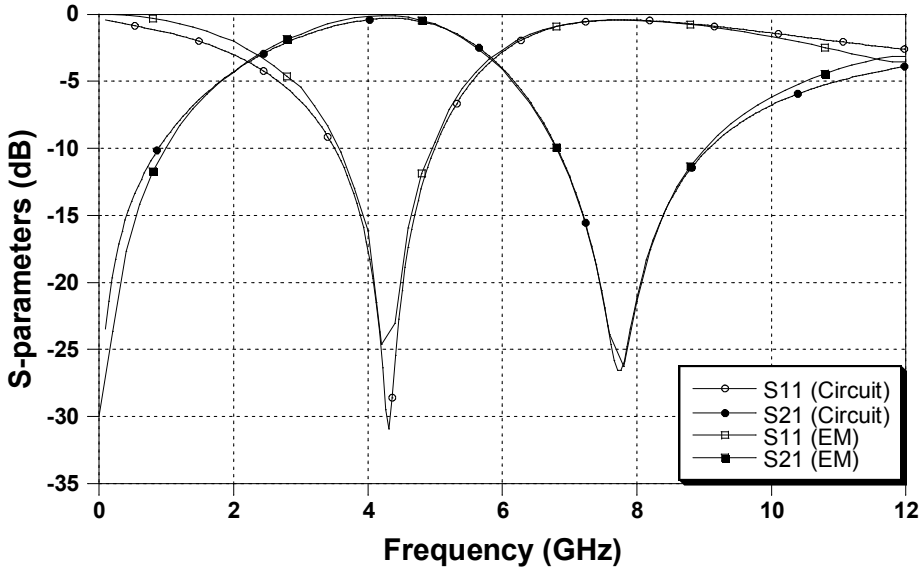

Fig. 3.43 Comparison of the *S*-parameters of the slot resonator shown in Fig. 3.41 (a) from the lumped-element circuit model (Fig. 3.42) and the EM simulation.

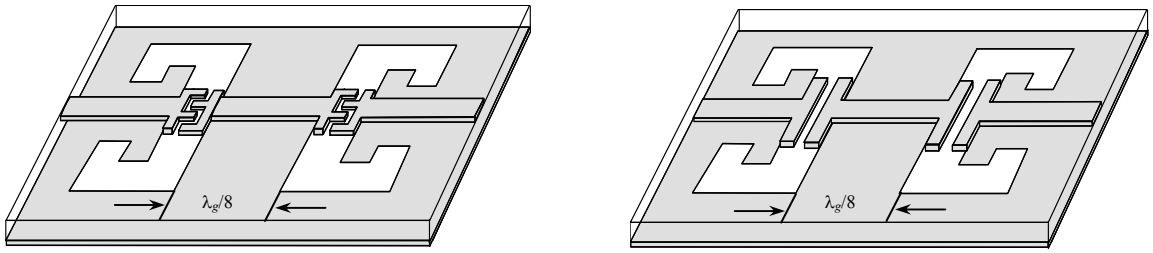

(a) (b)

Fig. 3.44 Schematics of 2-pole microstrip bandpass filters designed by using (a) the slot resonator shown in Fig. 3.41 (a) and (b) the slot resonator shown in Fig. 3.41 (b).

Fig. 3.45 reflects of the fabricated 2-pole microstrip bandpass filters with the schematic shown in Fig. 3.44 (a). The corresponding simulated and measured results for the fabricated filter are given in Fig. 3.46. A good agreement between the measurement results and those of EM simulations is demonstrated. The insertion loss is -0.8dB at the centre frequency of the filter.

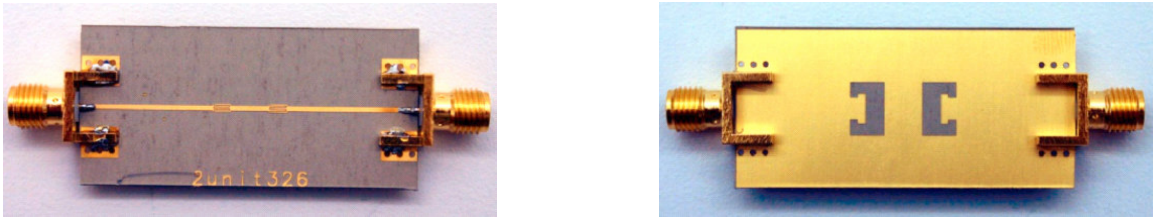

(a) (b)

Fig. 3.45 Fabricated microstrip bandpass filter with the schematic shown in Fig. 3.44 (a): (a) top view and (b) bottom view.

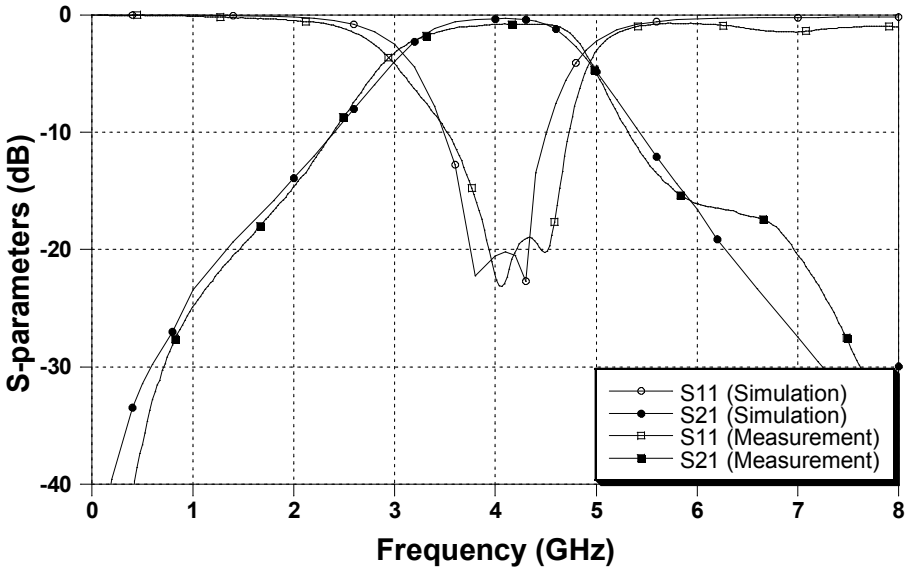

Fig. 3.46 Comparison of the *S*-parameters of the fabricated microstrip bandpass filter shown in Fig. 3.45 from the EM simulation and measurement.

Fig. 3.47 illustrates the fabricated 2-pole microstrip bandpass filters whose schematic isshown in Fig. 3.44(b). The corresponding simulated and measured results for the fabricated filter are given in Fig. 3.48. An insertion loss of -1.2dB at the centre frequency of the filter is obtained.

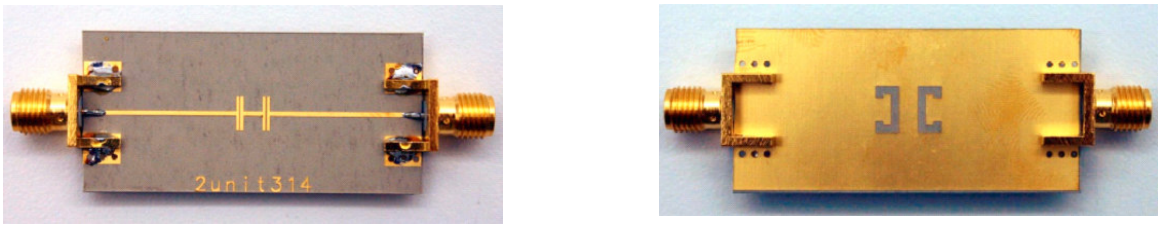

(a) (b)

Fig. 3.47 Fabricated microstrip bandpass filter with the schematic shown in Fig. 3.44 (b): (a) top view and (b) bottom view.

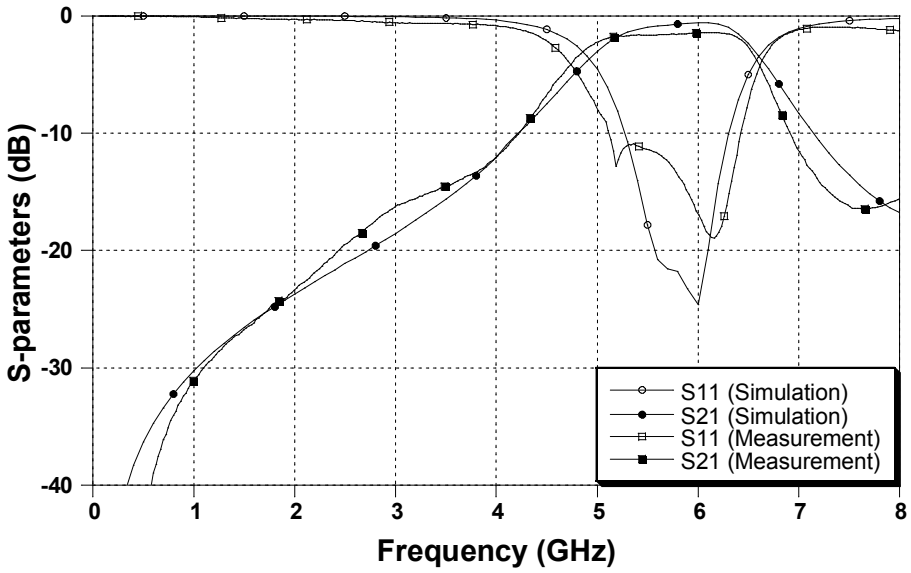

Fig. 3.48 Comparison of the *S*-parameters of the fabricated microstrip bandpass filter shown in Fig. 3.47 from the EM simulation and measurement.

Fig. 3.49 depicts a schematic of the designed 3-pole bandpass filter by using the slot resonator shown in Fig. 3.41 (a). Fig. 50 demonstrates that the EM simulation results are in a good correlation with the circuit simulation results.

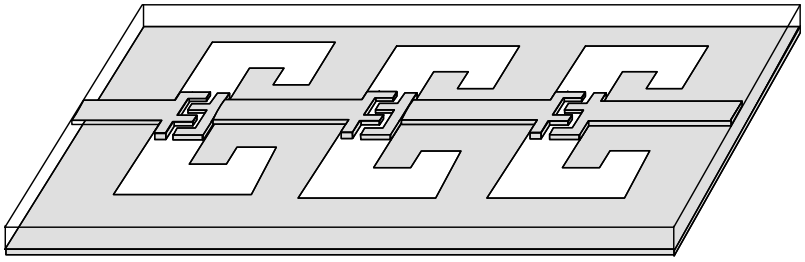

Fig. 3.49 Schematic of the designed 3-pole microstrip bandpass filter by using the slot resonator shown in Fig. 3.41 (a).

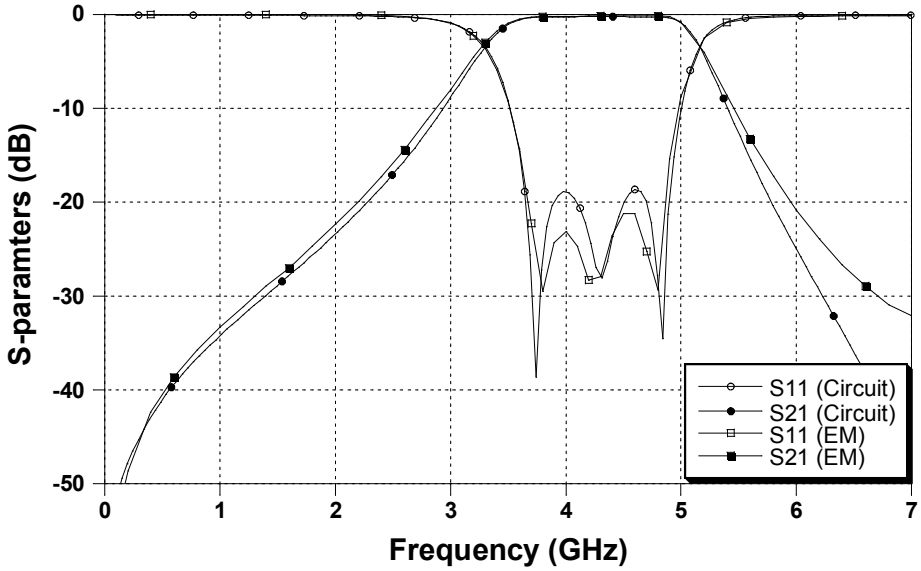

Fig. 3.50 Comparison of the *S*-parameters of the 3-pole bandpass filter shown in Fig. 3.49 from the circuit simulation and the EM simulation.

The novel microstrip bandstop, lowpass and bandpass filters, using proposed folded slots etched on the ground plane are introduced in this chapter. The bandstop filter is designed by using a general synthesis approach, based on the developed *RLC* lumped-element circuit model. Also, several microstrip lowpass filters employing the folded slot resonators, are fabricated and measured, providing a size reduction and a better RF performance than those traditional EBG-based microstrip filters. Several microstrip bandpass filters, using proposed folded slot structures, are designed and built as a very compact structure. Again, the measured results of the filters support the results of the simulations and exhibit a superior RF performance.

Chapter 4

Microstrip Tunable Lowpass Filters

4.1 Introduction

High performance RF tunable filters are needed in reconfigurable systems to facilitate efficient utilization of the available frequency spectrum. They are in demand in front-end receivers for the suppression of interference signals and for the relaxation of oscillator phase noise and dynamic range requirements.

Most of the work reported in the literature [70-79] has been focused on the tunable bandpass filters, whose insertion loss is determined by the Q of the filter itself and the Q of the tuning element whether it is a semiconductor, ferroelectric, ferromagnetic (YIG, ferrite), or MEMS device. YIG tunable filters suffer from a fairly bulky size despite their relatively low insertion loss. Semiconductor or MEMS tuning elements are amenable to integration with planar resonators, making it possible to realize miniature tunable bandpass filters. However, even with the use of high-Q MEMS tuning elements, the Q of this type of filter is limited mainly by the Q of the planar resonators.

The novel compact lowpass filter, demonstrated in Chapter 3, has an insertion loss close to that of a 50Ω transmission line of the same length. The integration of tuning elements into such types of lowpass filters [80, 81] results in a very low loss miniature tunable filter.

Although the majority of applications require the use of tunable bandpass filters, the availability of miniature tunable lowpass filters with a wide tuning range fits applications that require the suppression of out-of-band interference signals.

An implementation of digital and analogue tunable lowpass filters by using RF MEMS switches and varactor diodes, respectively, is presented in this chapter [81, 82]. To predict the performance of the tunable lowpass filters, the simple transmission line circuit models are employed. The analysis includes the effects of the physical dimensions of the filters and the tuning elements. The experimental results for the tunable lowpass filters confirm the results of the simulations, demonstrating a remarkable RF performance with a low loss and wide tuning range.

4.2 Microstrip Tunable Lowpass Filters

This section presents a new concept for implementing tunable lowpass filters by employing proposed folded slot resonators etched on the ground plane. When RF MEMS switches are selected to short-circuit the slots in the ground plane, the effective length of the slots can be varied to achieve a tunability at discrete frequencies. Continuous tuning is achieved by replacing the switches with varactors as the tuning elements. After simple transmission line circuit models for the proposed structures are presented, the tunable filters are then analyzed.

4.2.1 Design of Digital Tunable Lowpass Filters

The digital tunable lowpass filters presented in this section use commercially available RF MEMS switches [83] for integration into the slots. Such types of the switches act as an open circuit when in the OFF state and a short circuit when in the ON state. A digital tunable lowpass filter is implemented by actuating arrays of RF MEMS switches located on the slots between the ON and OFF states, thereby changing the cutoff frequency of the lowpass filter.

4.2.1.1 Digital Tunable Slot Resonators

Fig. 4.1 (a) shows a schematic of a $50\,\Omega$ microstrip line with a folded slot etched on the ground plane [80]. An EM simulation is performed by HFSS, whose frequency response is given in Fig. 4.1 (a). The structure exhibits typical passband-stopband properties [80]. The resonant frequency of the resonator is determined by width W and length L of the folded slot. Fig. 4.1 (b), (c), and (d) illustrate three configurations of the structure where short bridges are placed across the slot at different locations. Also, the RF performance of these structures is represented in Fig. 4.2 (b), (c), and (d), respectively. It is observed that, upon moving the short bridge from the slot edge (i.e., Fig. 4.2 (b)) to the slot centre (i.e., Fig. 4.2 (d)), the corresponding resonances are shifted to higher frequencies, demonstrating a tuning range of 4GHz.

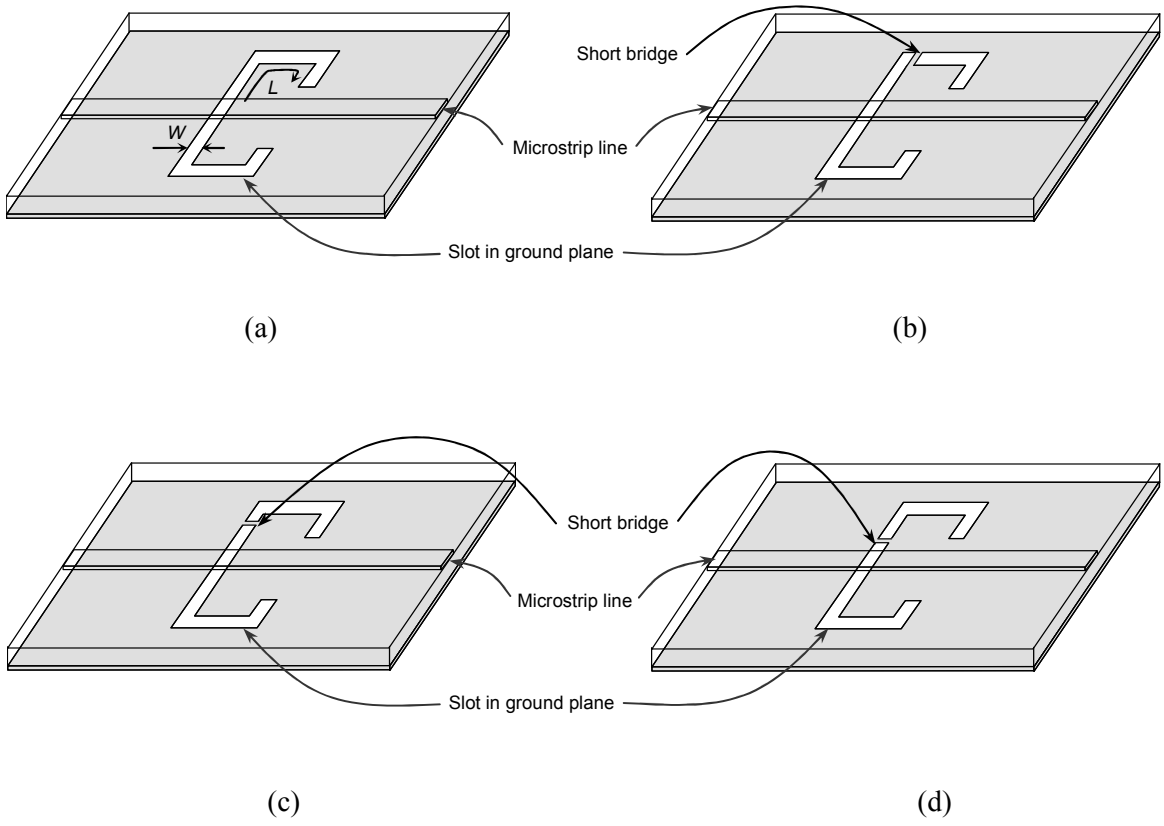

Fig. 4.1 Schematics of the slot resonators: (a) a resonator without any short bridges, (b), (c), and (d) resonators with short bridges at different positions.

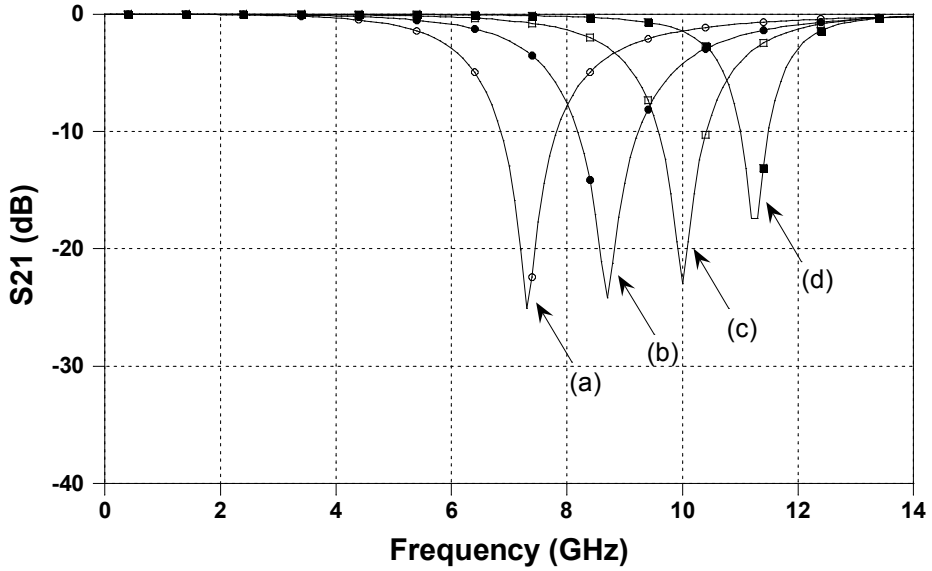

Fig. 4.2 EM simulations of the transmission coefficients of the slot resonators in Fig. 4.1.

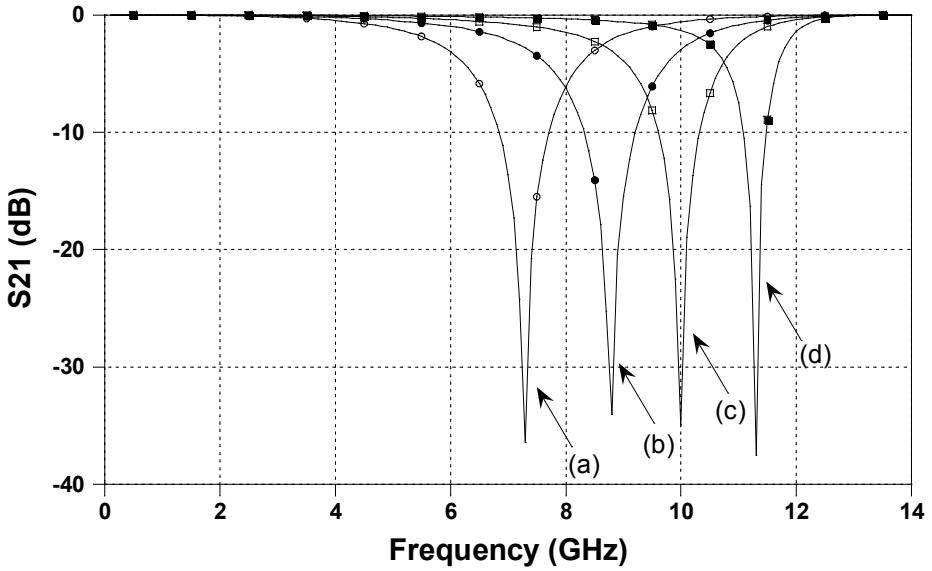

Fig. 4.3 Transmission line circuit simulations of the transmission coefficients of the slot resonators shown in Fig. 4.1.

To achieve a fast and accurate analysis of the slot resonators in Fig. 4.1, the transmission line circuit model, illustrated in Fig. 3.14 is used again. The length of L_2 is equal to L_1 in Fig. 4.1 (a) and is varied, as seen in Fig. 4.1 (b) to Fig. 4.1 (d), due to the different locations of the short bridge. Fig. 4.3 displays the simulation results of the corresponding slot configurations in Fig. 4.1 based on the transmission line circuit model. The results confirm those of HFSS, shown in Fig. 4.2.

The advantage of this resonator configuration is that the Q of the switching element (shorting bridge) does not have a significant impact on the RF performance of the structure. To investigate the losses caused by the short bridge on the slot, very lossy conductor is used as the short bridge in the simulation of the slot resonator in Fig. 4.1 (b). Fig. 4.4 presents a comparison of the simulated results between the resonator, assuming a perfect conductor for the short bridge, and a very lossy conductor with a conductivity of 4×10^5 s/m (i.e., 100 times less than the conductivity of gold). The resistance of the short bridge is calculated to be 10 Ω, if a conductivity of 4×10^5 s/m [84] is assumed. This value of the resistance is much higher than that of MEMS switches. It is selected high enough to represent the worst case scenario. It can be seen that the lossy element does not have a major impact on the insertion loss within the passband, indicating that the Q of the switching elements have a negligible effect on the insertion loss of the filter. Therefore, the loss of the tunable filter is predominantly determined by the Q of the planar structure; in this case, it can be as low as that of a 50Ω transmission line of the same length.

4.2.1.2 Digital Tunable Lowpass Filters

The proposed concept of the digital tunable slot resonators can be used to implement higher order tunable lowpass filters. Fig. 4.5 shows a schematic of a typical microstrip lowpass filter with 10-slot resonators, etched on the ground plane [80]. The frequency response of this filter is shown as curve (a) in Fig. 4.6. In addition, Fig. 4.6 shows three cases, where the short bridges are placed at various positions across each slot of the filter. The corresponding frequency responses for positions b, c, and d are marked on Fig. 4.6 as (b), (c), and (d).

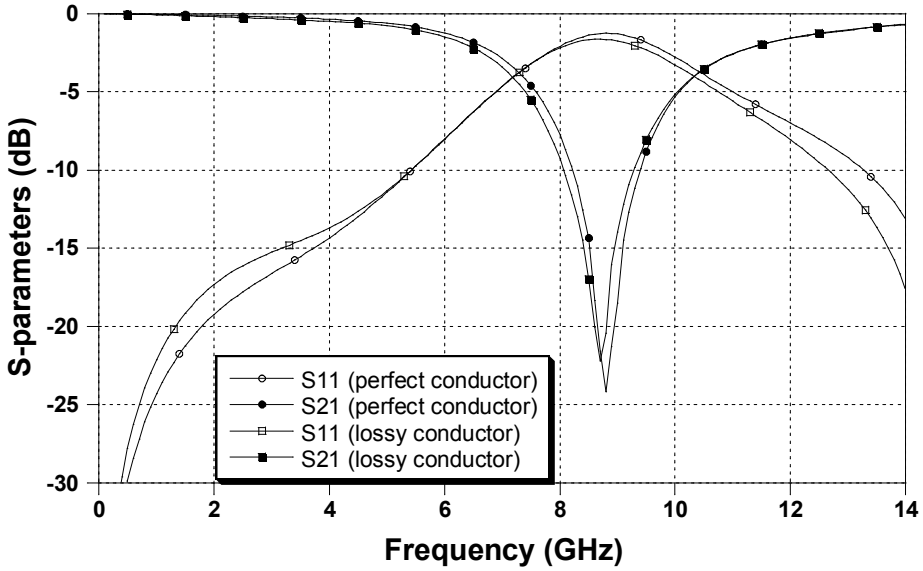

Fig. 4.4 Comparison of the simulation results, where the short bridge is made of either a perfect conductor or a very lossy conductor.

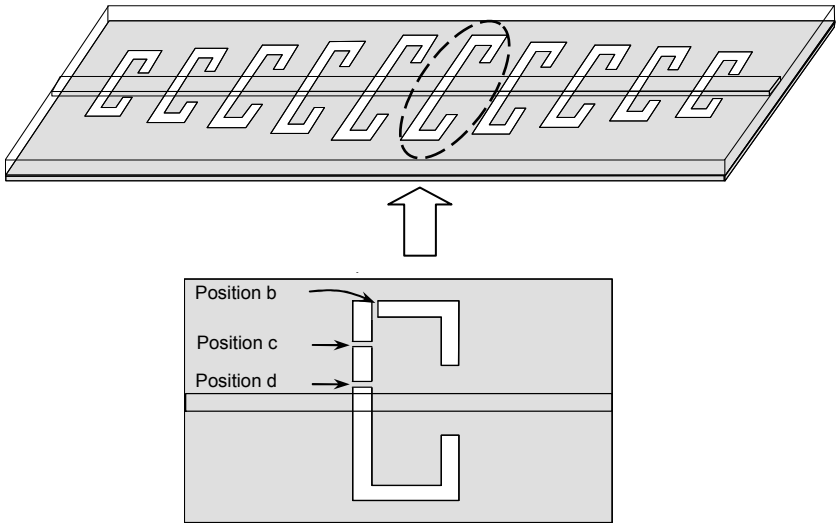

Fig. 4.5 Schemetic of a 10-slot microstrip lowpass filter.

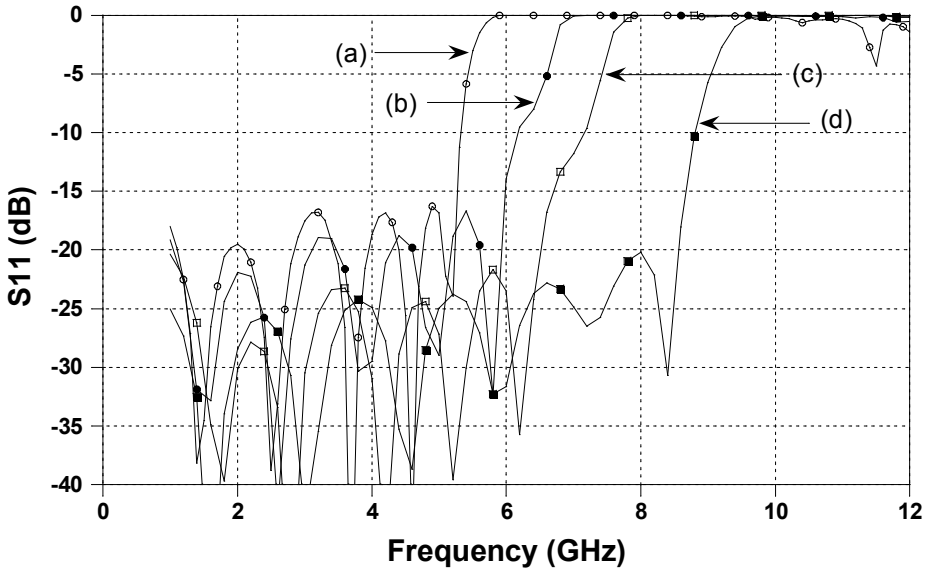

(i)

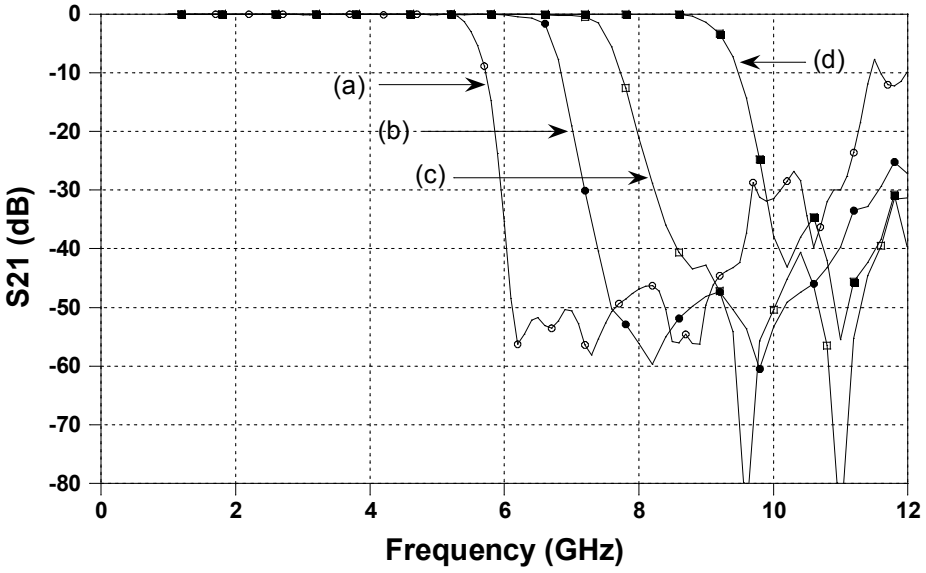

(ii)

Fig. 4.6 Simulated *S*-parameters (i) S_{11} and (ii) S_{21} of the lowpass filters: (a) without any short bridges and (b), (c), and (d) with short bridges at position b, c, and d respectively, as shown in Fig. 4.5.

To experimentally verify the proposed concept of tunable lowpass filters, bonding wires are used to emulate the short bridges. Fig. 4.7 pictures the fabricated filter and a microphotogragh of the centre slot with a bonding wire at its top left corner. The experimental results for the fabricated filter with wire bonds at positions b, c, and d on each slot (Fig. 4.5) are plotted in Fig. 4.8. It can be seen that a wide tuning range of approximately 60%, with a low insertion loss performance, is obtained.

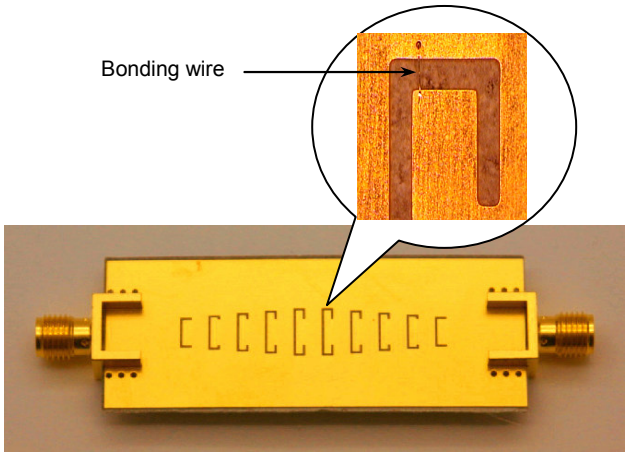

Fig. 4.7 Microstrip lowpass filter (bottom view) and the centre slot with the bonding wire at its top left corner.

The previous design of using the bonding wires as the short bridges on the slots to vary the cutoff frequency of the filter validates the proposed concept of implementing tunable lowpass filters. In principle, if the switches are on the slots of the filter, instead of the bonding wires, it is expected that the cutoff frequency of the filter can be digitally adjusted by activating the switches between their ON and OFF states. In addition, an increased flexibility in the tuning range of the filter is achievable by an appropriate combination of the ON/OFF states of the switches.

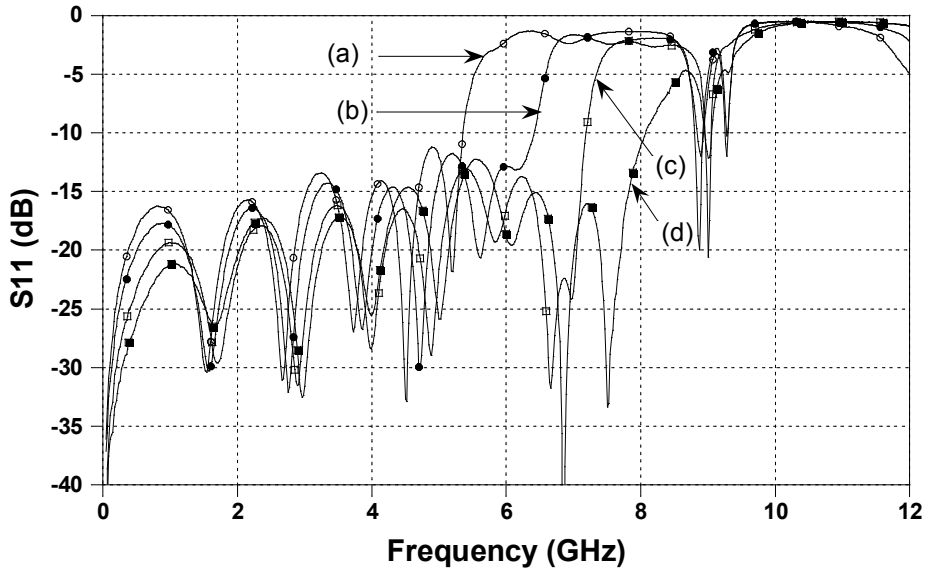

(i)

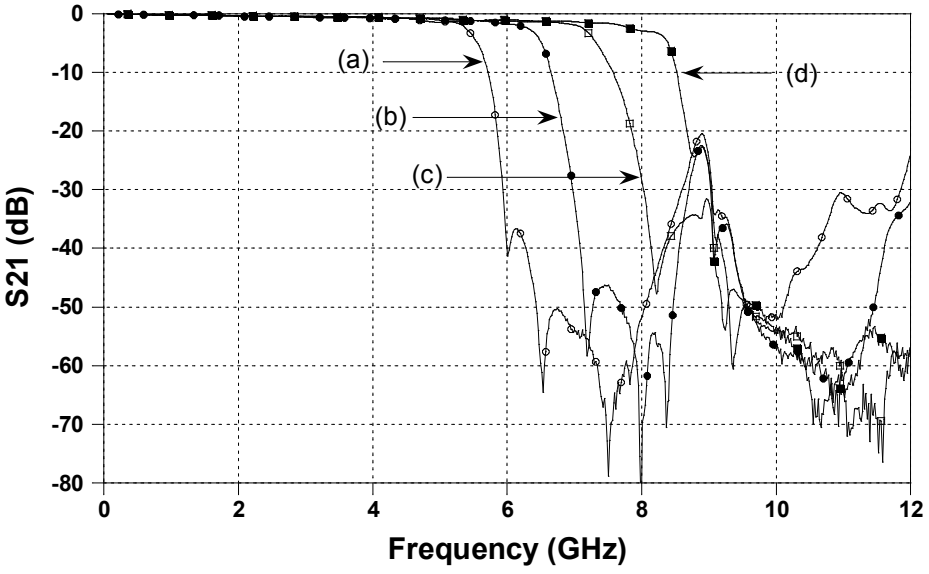

(ii)

Fig. 4.8 Measured *S*-parameters (i) S_{11} and (ii) S_{21} of the lowpass filters: (a) without any short bridges and (b), (c), and (d) with short bridges at position b, c, and d respectively, as shown in Fig. 4.5.

The commercially available Single-Pole-Single-Throw (SPST) MEMS switches from Radant [83] are selected as a replacement for the short bridges, implemented in the digital tunable lowpass filters. These switches are designed to operate with a triggering voltage of 80 V over a frequency range of DC – 12GHz. At 4GHz, the isolation of the switch is 20dB, whereas in the ON state the insertion loss of the switch is 0.18dB and the return loss is 24dB. The ON state resistance of the switch is less than 1Ω.

Fig. 4.9 illustrates the fabricated digital tunable lowpass filter loaded with two arrays of switches, four for each array. This design leads to a switched tunable filter with four states. The simulated and measured transmission coefficients of the tunable filter are shown in Fig. 4.10 and Fig. 4.11, respectively. The measurements reveal that the cutoff frequency of the tunable filter is 4.5GHz with all the switches off (state 1). The frequency shifts to 5.2GHz, when only the first array of switches is turned on (state 2), and climbs to 5.8GHz, when only the second array of switches is activated (state 3). A cutoff frequency of 6.5GHz is obtained, when all the switches are turned on (state 4). The experimental results show a broad tuning range of 2GHz with a low insertion loss of 0.6dB. It can be seen that there is a minor distortion of the frequency response of state 4. Perhaps, this can be attributed to the fact that all of the switches might not have identical operating performances, which slightly degrades the overall performance of the tunable filter.

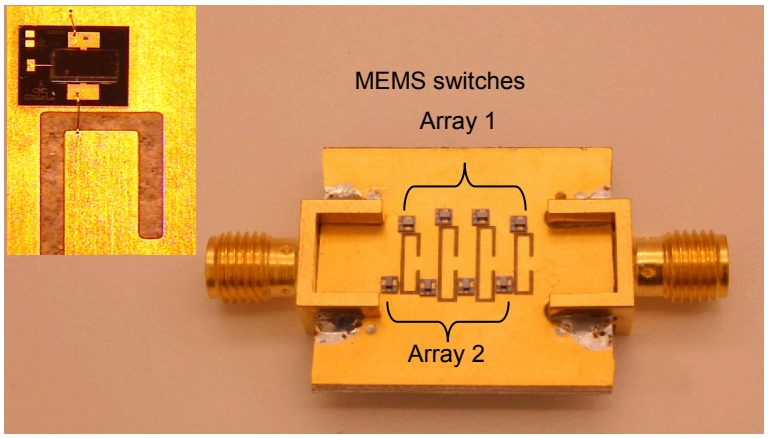

Fig. 4.9 Digital tunable lowpass filter (bottom view) using two arrays of SPST MEMS switches and the detail of MEMS switch assembly.

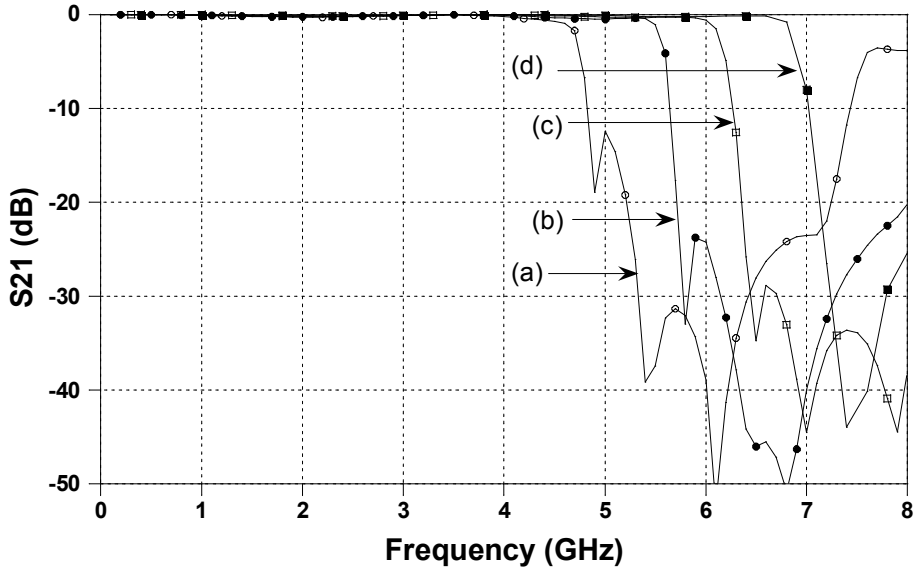

Fig. 4.10 Simulated transmission coefficients of the fabricated digital tunable lowpass filter shown in Fig. 4.9: (a) state 1, (b) state 2, (c) state 3, and (d) state 4.

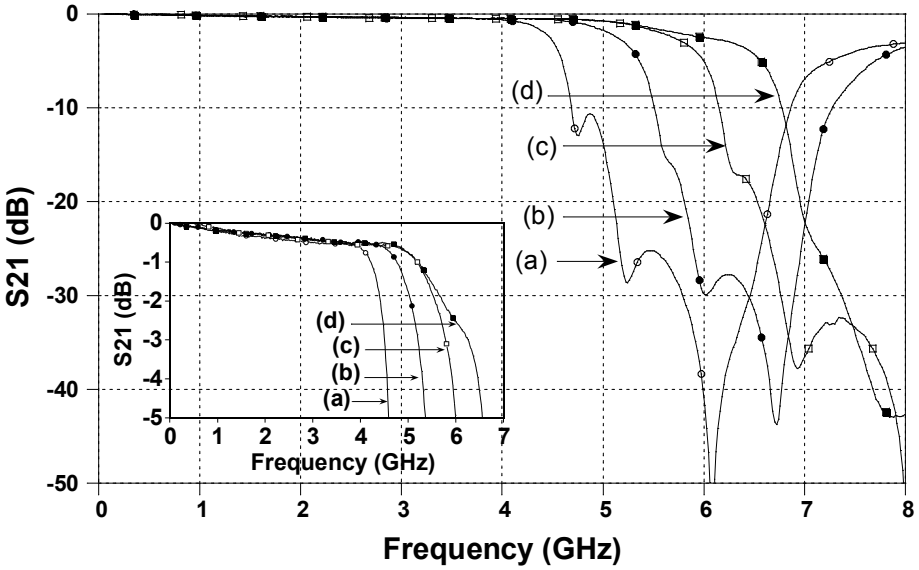

Fig. 4.11 Measured transmission coefficients of the fabricated digital tunable lowpass filter shown in Fig. 4.9: (a) state 1, (b) state 2, (c) state 3, and (d) state 4; Insert: magnified measured transmission coefficients in the passband.

It should be pointed out that the experimental tunable lowpass filters, without shielding, exhibit radiations from the slots in the stopband. This radiation, which occurs only in the stopband, has no significant impact on the passband performance of the tunable lowpass filters. However, it is necessary and important to take into account the radiation loss of the designed filters. This is due to the fact that in some cases, there is a requirement to reduce or avoid the radiation of the slots to any other neighboring circuits. Like conventional microstrip filters, the proposed tunable lowpass filter needs to be packaged. The performance of the filter is investigated, with the filter positioned inside a metallic housing. Fig. 4.12 displays a three-dimensional (3-D) view of the 4-slot tunable lowpass filter (Fig. 4.9) in a metallic box. Because the ground plane is perforated, the filter must be suspended in the box instead of being fixed on a metal base directly.

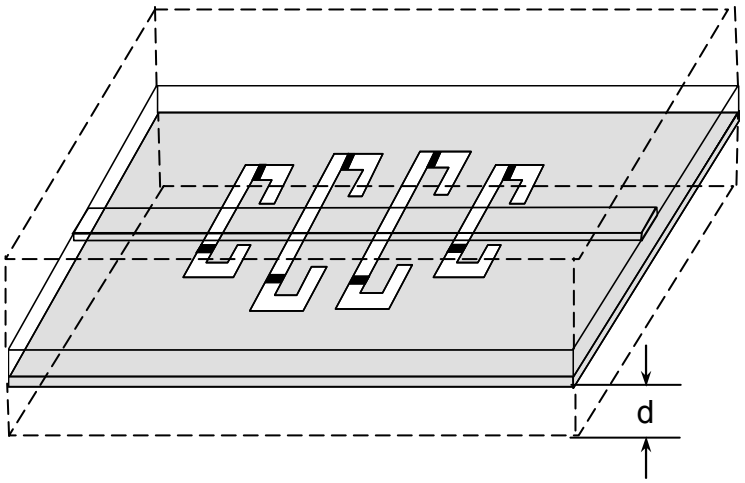

Fig. 4.12 3-D view of the tunable lowpass filter suspended in a metallic housing (dashed line).

The simulation results indicate that the effect of the radiation loss significantly depends on spacing *d* between the ground of the filter and the bottom plate of the housing. If spacing *d* is very small; that is, less than the thickness of the dielectric substrate, the cutoff frequency of the passband significantly shifts to a higher frequency, than that of the unshielded filter. The extreme situation happens if there is no spacing between the ground and the bottom plate of the housing. In this case, the circuit is no longer a lowpass filter; instead, it transmits signals like a microstrip line. When the spacing is large enough; that is, more than four times of the thickness of the substrate, the cutoff frequency of the filter remains unchanged. Fig. 4.13 offers a comparison of the radiation loss $(1-|S_{11}|^2-|S_{21}|^2)$ between the tunable lowpass filter with and without a metallic housing. All switches are in the OFF state (state 1 in Fig. 4.10). It can be clearly seen that the radiation mainly occurs in the stopband.

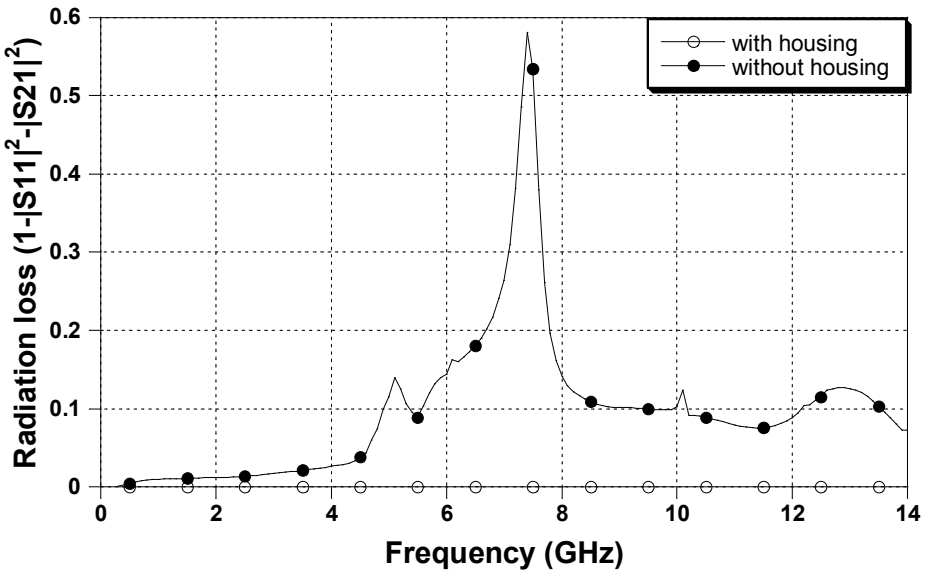

Fig. 4.13 Comparison of the simulated magnitude of the radiation loss $(1-|S_{11}|^2-|S_{21}|^2)$ between the tunable lowpass filter (Fig. 4.9) with and without a metallic housing when all switches are in the OFF state.

4.2.2 Design of Analogue Tunable Lowpass Filters

The replacement of the RF MEMS switches with varactor diodes attached across the slots, provides the capability to continuously tune the filters. As a result, a lowpass filter with tunability at continuous frequencies, based on the previous concepts, is developed, fabricated, and measured.

4.2.2.1 Analogue Tunable Slot Resonators

An analog tunable slot resonator is obtained by using a variable capacitor loaded across the slot in the ground plane. Fig. 4.14 exhibits a configuration of a tunable slot resonator with a varactor located at the position of the short bridge and the corresponding equivalent circuit. In the ideal case of no loss, a circuit analysis is performed, based on the same approach in Section 3.4.1 by considering the varactor as a variable capacitor, mounted at a specific position of the slot.

In Fig. 4.14 (b), Z_{S2} is given by

$$Z_{S2} = Z_{SC} \frac{\dfrac{1}{1/Z_{S3} + j\omega C_J} + jZ_{SC}\tan(\dfrac{2\pi}{\lambda_{sg}} \cdot L_2)}{Z_{SC} + j\dfrac{1}{1/Z_{S3} + j\omega C_J}\tan(\dfrac{2\pi}{\lambda_{sg}} \cdot L_2)}. \qquad (4.1)$$

Z_{Si} (i = 1,2,3) is the input impedance at the positions shown in Fig. 4.14 (b). Z_{S1} and Z_{S3} are calculated by using Eq. (3.19) in Chapter 3. The definitions of λ_{sg} and Z_{SC} are the same as those definitions in Eq. (3.19). Consequently, the corresponding S-parameters of the slot resonator in Fig. 4.14 (a) are calculated by the same method as the one used to calculate the S-parameters for the folded slot resonator itself, in Section 3.5.1.

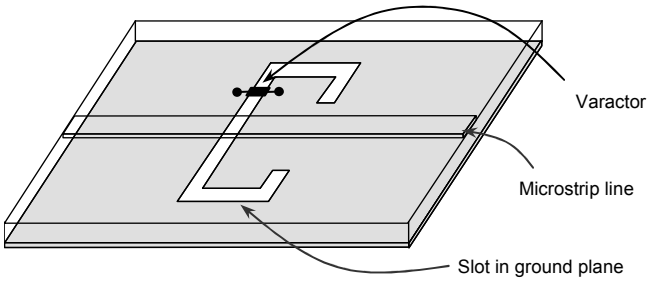

(a)

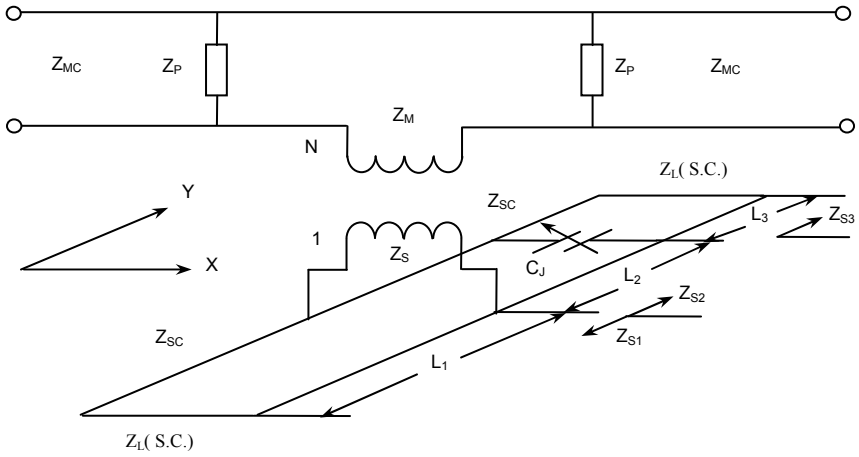

(b)

Fig. 4.14 Tunable slot resonator with a varactor on the slot: (a) configuration and (b) equivalent circuit model.

The HFSS EM simulation results are obtained by assuming a parallel-plate capacitor connected across the slot. The capacitance is varied by changing the thickness of the dielectric material between the two plates. Both the EM and the circuit (Fig. 4.14 (b)) simulation results are depicted in Fig. 4.15. It is observed that the resonant frequency moves down by 1.4GHz as the capacitance value of the variable capacitor increases from 0.2pF to 0.7pF. Again, the two results are in good agreement. Since the capacitance of the varactor varies within a range of the DC bias voltage, a continuous tuning range is achievable, when the DC bias voltage is adjusted within the varactor's voltage range.

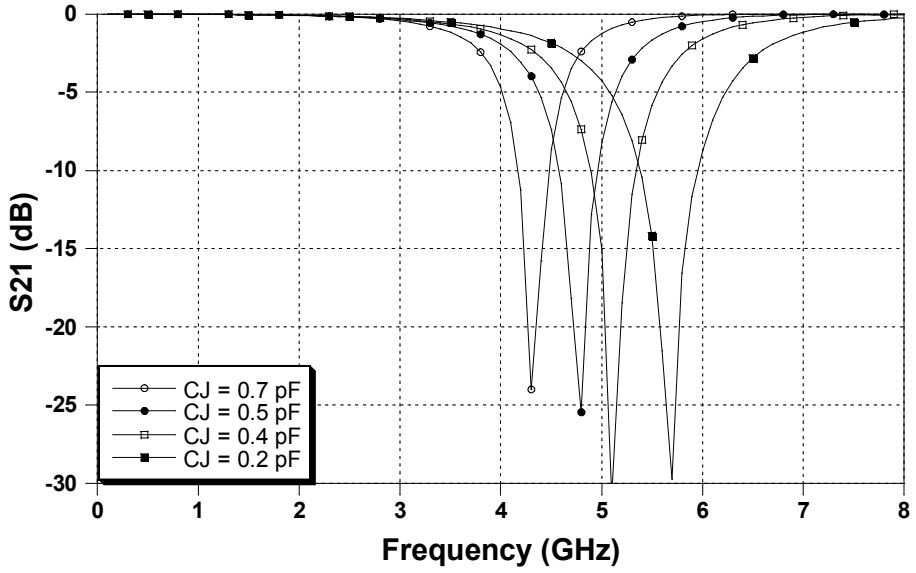

(a)

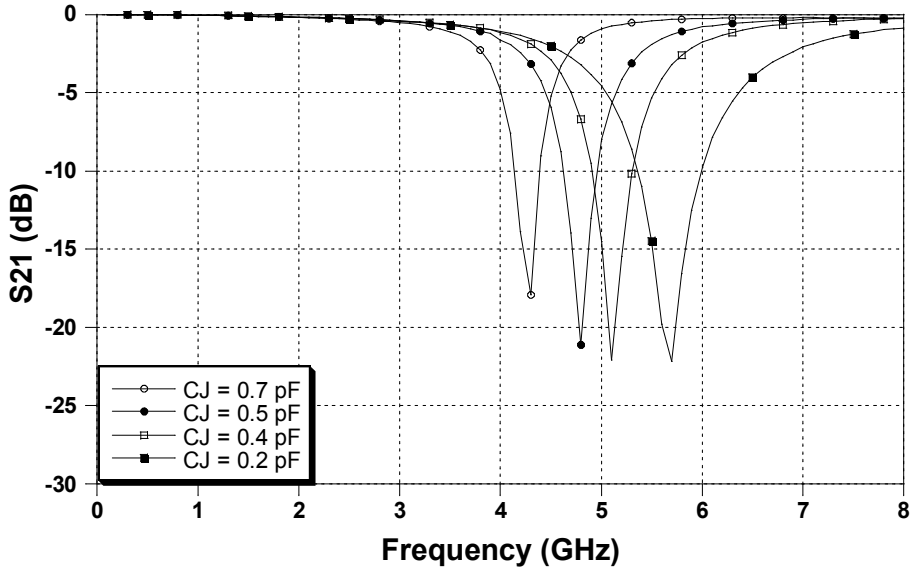

(b)

Fig. 4.15 Simulation results of a tunable slot resonator with a variable capacitor on the slot in Fig. 4.14 (a): (a) circuit simulation and (b) EM simulation.

To experimentally validate the concept, an analogue tunable slot resonator is fabricated with a MDT varactor diode [85] mounted on the ground plane. In Fig. 4.16, the varactor is biased with a 100pF capacitor from the bias line to ground, providing an RF short for the varactor and an open circuit for the bias.

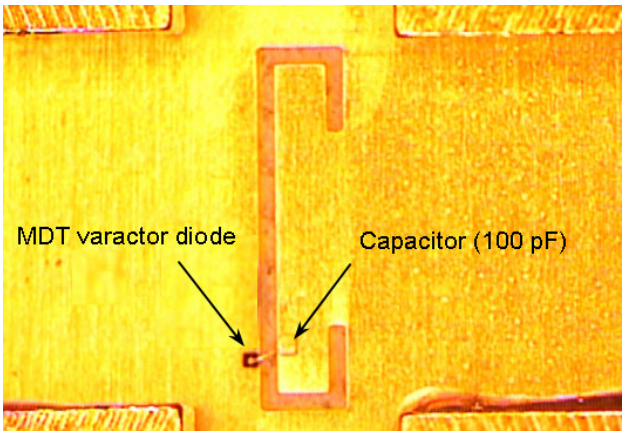

Fig. 4.16 Analogue tunable slot resonator (bottom view) with a MDT varactor diode on the ground plane.

Fig. 4.17 conveys the measured results of the tunable resonator with junction capacitance C_J varied from 0.2pF (when the bias voltage = 25V) to 0.7pF (when the bias voltage = 1V) over a 25V bias range. The results indicate that a practical tuning range of 1.4GHz is achieved, the same as the value predicted by the proposed circuit model analysis. However, each resonant frequency from the testing results is consistently around 0.7GHz lower than those values of the simulations. The measurement results exhibit the same loss level within the passband as predicted from the simulations; a degradation of the rejection level is yet revealed in the stopband. These observed discrepancies, in terms of the frequency shift, are very likely due to the package parasitics of the varactor diode. The problem can be circumvented by testing the varactor diode independently to determine its actual equivalent circuit before assembly.

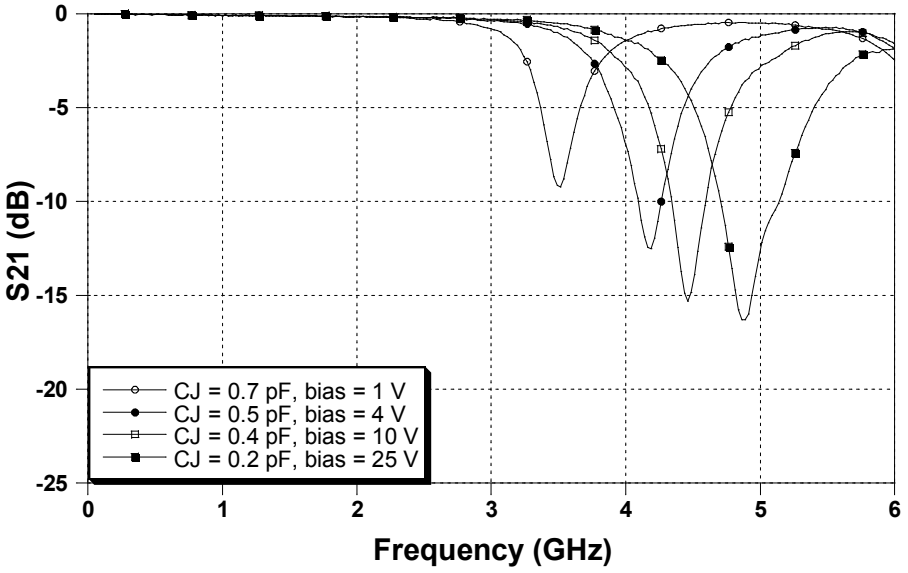

Fig. 4.17 Measurement results of the fabricated analogue tunable slot resonator with a MDT varactor diode on the ground shown in Fig. 4.16.

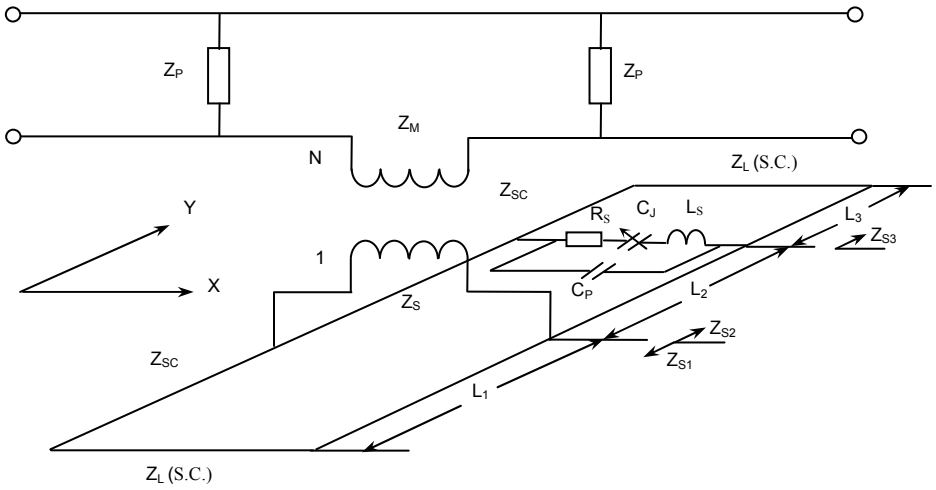

Fig. 4.18 Lossy circuit model of a tunable slot resonator with a packaged varactor.

To further investigate the loss effect on the RF performance, a lossy model of the varactor is used to replace the simple lossless variable capacitor in the circuit analysis to more closely represent the real situation. The corresponding circuit diagram is shown in Fig. 4.18. R_S is the series resistance of the varactor, whereas C_P represents the shunt package capacitance. L_S accounts for the inductance of the bonding wire to the package. Junction capacitance, C_J(V), varies as a function of the bias voltage.

In the investigation, described in this thesis, $R_S = 4\Omega$, $L_S = 1.0$nH and $C_P = 0.15$pF. All the characteristics of the varactor diode used in the tunable resonator are provided by MDT from a data sheet, listing the measured performance of each varactor. The circuit simulation results of the lossy model of the varactor (Fig. 4.18) are presented in Fig. 4.19. Now it is easy to include the varactor losses, such that the results are in good agreement with the measured ones. Theoretically, the varactor is a capacitive loading that is equivalent to increasing the electrical length of the slots. Consequently, analogue tunable slot resonators with varactors, provide tuning ranges at lower frequencies than those using digital tunable slot resonators.

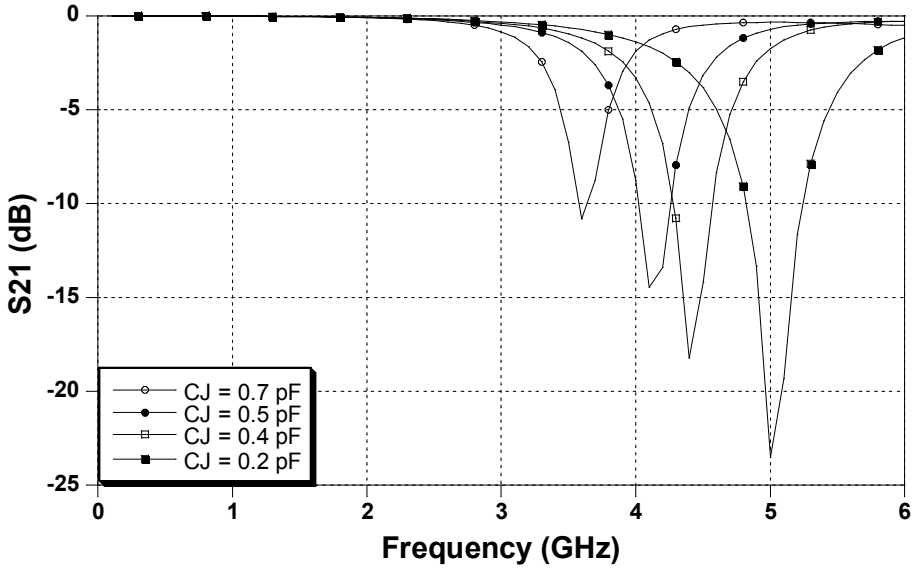

Fig. 4.19 Simulation results of the fabricated tunable slot resonator using the lossy model of the varactor shown in Fig. 4.18.

4.2.2.2 Analogue Tunable Lowpass Filters

Analogue tunable lowpass filters can be implemented by cascading several varactor-tuned slot resonators. Unlike the digital tunable lowpass filter whose tuning range is principally determined by the position of the RF MEMS switches across the slots, the tuning range of the analogue tunable lowpass filter is decided by both the value of the variable capacitance and the location of the varactors on the slots. Fig. 4.20 displays a schematic of an analogue tunable lowpass filter with the same varactors placed across the slot at positions A and B. The simulated RF performance of the filter for the two cases is shown in Fig. 4.21 (a) and (b) respectively. Obviously, the tuning range of the filter depends on the location of the varactor diodes. Input impedance *Zs* of the single slot in Fig. 4.18 varies according to the different location of the varactor on the slot, like the transmission characteristics of the tunable filter with a cascade of several slot resonators.

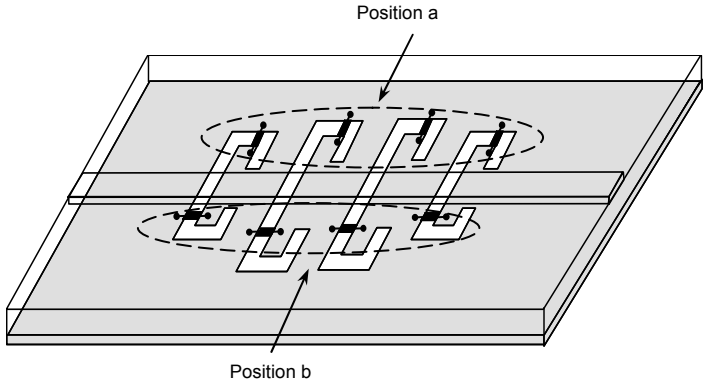

Fig. 4.20 Schematic of an analogue tunable lowpass filter with the same varactors placed across the slot at positions a and b.

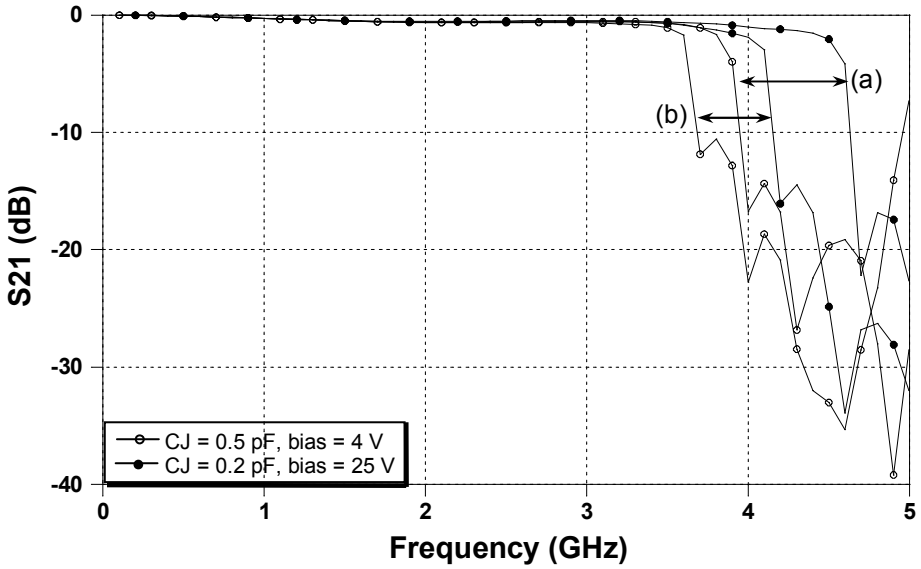

Fig. 4.21 Simulated transmission coefficients of the analogue tunable lowpass filter with the same varactors at the different locations on the slots: (a) varactors at position a and (b) varactors at position b.

An analogue tunable lowpass filter, as illustrated in Fig. 4.22, is designed, manufactured, and measured. Transmission line equivalent circuit models for single slot resonators are used to construct the circuit model for the entire tunable filter. Four varactor diodes are mounted on the ground plane in the same manner as the RF MEMS switches of the digital tunable 4-slot lowpass filter. The varactor diodes are from MDT [85] with a series resistance of 4Ω, a series inductance of 1.0nH, and a package capacitance of 0.15pF. Junction capacitance C_J varies from 0.2pF to 0.7pF over a 25V bias range. Each varactor is biased with a 100pF DC block capacitor. The four varactors are then connected one to another through a wire bond, such that only one DC bias is needed for operating the entire circuit.

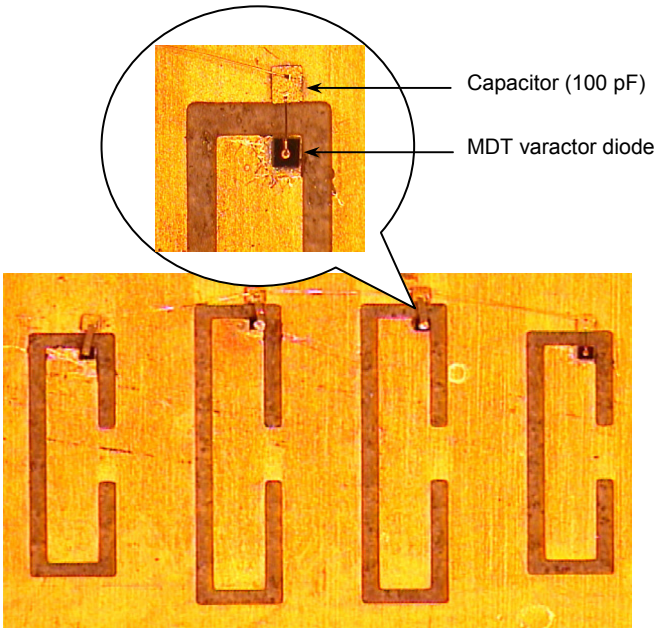

Fig. 4.22 Analogue tunable lowpass filter (bottom view) using four varactors and the detail of the varactor assembly.

The simulated and measured transmission coefficients of the analogue tunable lowpass filter are shown in Fig. 4.23 (a) and (b) respectively. The calculated tuning range is from 3.7GHz (C_J = 0.5pF) to 4.6GHz (C_J = 0.2pF). The measured response of the filter presents a tuning range from 3.6GHz to 4.4GHz with all varactors biased equally in parallel. The results clearly indicate that the agreement between the measured results and theoretical predictions is good enough that the developed transmission line circuit model is definitely practical for applications for designing such types of filters. The measured insertion loss of the entire passband under each bias voltage is less than 0.6dB, which is almost the same as that of the lowpass filter itself. The experimental results prove that by varying the voltages applied to the varactor diodes over a 25V bias range, a tuning range of 0.8GHz is achievable without a performance degradation in the passband. Fig. 4.24 depicts the measured 3dB cutoff frequency of the analogue tunable lowpass filter as a function of the applied varactor bias voltage.

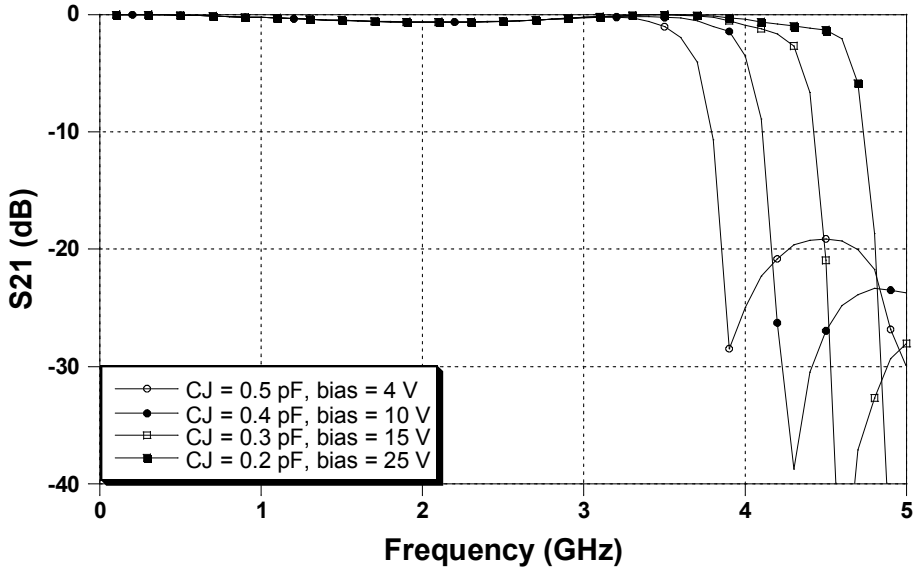

(a)

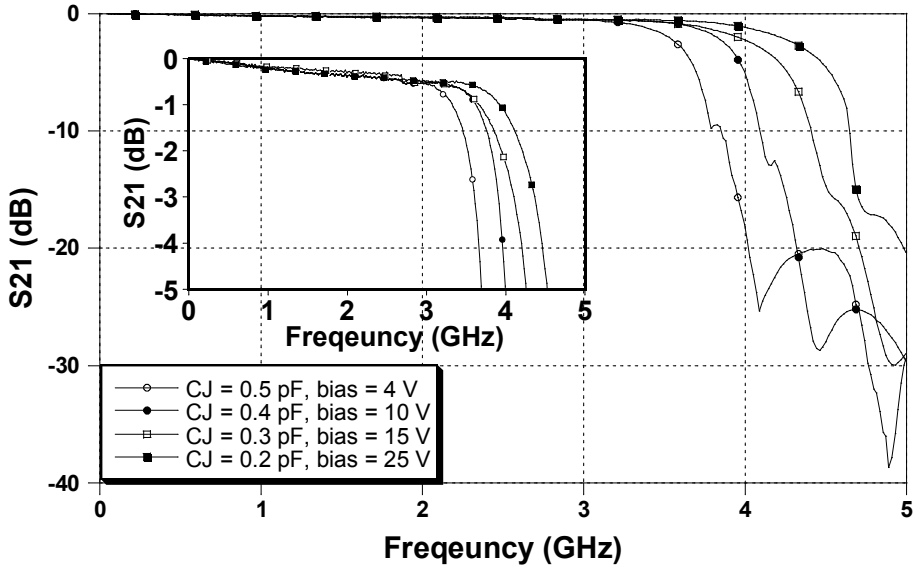

(b)

Fig. 4.23 Transmission coefficients of the fabricated analogue tunable lowpass filter shown in Fig. 4.22: (a) circuit simulation results and (b) measurement results; Insert: magnified measured transmission coefficients in the passband.

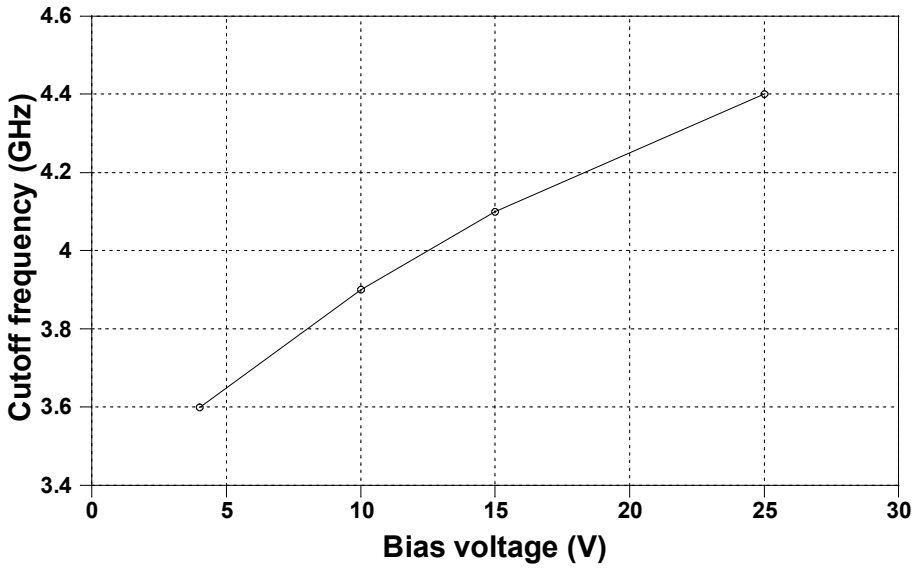

Fig. 4.24 Measured 3dB cutoff frequency of the fabricated analogue tunable lowpass filter versus the applied bias voltage of the varactor.

4.2.3 Ultra-Wideband Tunable Lowpass Filter

It is noticed that the digital tunable lowpass filter, described in Section 4.2.1, provides a tuning range of 2GHz (from 4.5GHz to 6.5GHz), whereas the analogue tunable lowpass filter in Section 4.2.2 presents a total tuning range of 0.8GHz (from 3.6GHz to 4.4GHz). For a fixed slot length, the tuning range can be extended to a higher frequency with the use of switches and to a lower frequency with the use of varactors. It is expected that the combination of these two types of tuning elements (i.e., the switches in Section 4.2.1.2 and the varactors in Section 4.2.2.2) in the filter can generate an even larger tuning range. This concept is demonstrated in Fig. 4.25.

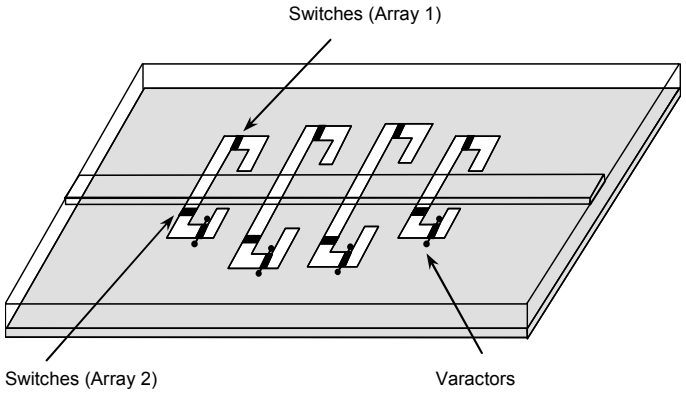

Fig. 4.25 Configuration of the ultra-wideband tunable lowpass filter.

Fig. 4.26 illustrates the simulated transmission coefficients of the proposed tunable lowpass filter in Fig. 4.25. The cutoff frequencies of the ultra-wideband tunable lowpass filter at the different states are listed in Table 4.1, where the results demonstrate a broad tuning range of 3GHz. In this case, varactors can also be used for fine tuning the filter.

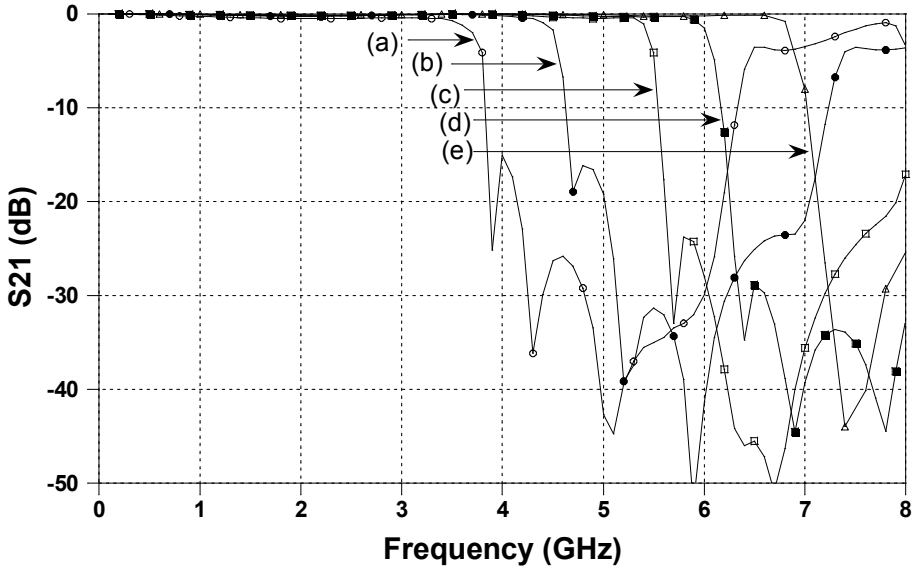

Fig. 4.26 Simulated transmission coefficients of the ultra-wideband tunable lowpass filter shown in Fig. 4.25: (a) state 1, (b) state 2, (c) state 3, (d) state 4, and (e) state 5.

Table 4.1 Cutoff frequencies of the ultra-wideband tunable lowpass filter at the different states.

	Switches (Array 1)	Switches (Array 2)	Varactor Bias (V)	Junction Capacitance C_j (pF)	Cutoff Frequency (GHz)
State 1	OFF	OFF	4	0.5	3.7
State 2	OFF	OFF	25	0.2	4.6
State 3	ON	OFF	25	0.2	5.4
State 4	OFF	ON	-	-	6.0
State 5	ON	ON	-	-	6.7

Chapter 5

Low-Cost Dielectric Resonator Filters

5.1 Introduction

A wireless communication system demands a large number of base station filters with not only a good in-band performance in terms of low losses, but also a reliable out-of-band spurious performance. DR filters are preferable for wireless base stations due to their superior characteristics of a high Q and miniaturization. However, cost reduction is still a key factor for furthering the applications of DR filters in wireless base station applications. There are increased demands for low-loss DR filters that are compact, and capable of being manufactured in a large quantity at a reasonable low cost [86].

The most commonly used DR structures are divided into two configurations: individual dielectric resonators that are loaded axially in metal enclosures, in which it is difficult to physically support the resonators [32, 35, 87], or individual resonators that are mounted in a planar configuration [40, 44, 88, 89]. In the latter case, DRs are centred and mounted inside a filter housing by a support of low-dielectric-constant and low-loss material. The cost involved with the assembly, alignment, and integration of the combined dielectric resonator/support structure is a major factor of the overall cost of DR filters. Additionally, grinding the individual resonators and machining the individual supports contributes to the

overall cost of DR filters. Consequently, the current approaches for implementing DR filters are therefore relatively expensive and hardly amenable to mass production.

In addition, the employment of nonadjacent couplings to implement advanced filter functions such as asymmetric frequency responses is required in some applications. A cascaded triplet is essential for asymmetric filter realization. This triplet can be regarded as a basic building block for the implementation of higher order coupled filters with asymmetric responses. A transmission zero in the stopband of the triplet is formed by producing either a positive or negative cross coupling between the input and output resonators. In traditional DR triplets, probes are sometimes needed to realize these transmission zeros. The traditional DR triplets are, therefore, mechanically difficult to manufacture and integrate due to the complicated assembly of the probe. This drives up the production cost significantly, emphasizing the need for a new approach to implement the nonadjacent coupling for the DR triplets.

In this chapter, a novel DR filter configuration, implemented as a single piece of a high-K ceramic substrate, is presented [90, 91]. The proposed configuration considerably reduces the cost of assembly and integration, associated with conventional DR filters. A 2-pole and 4-pole filter of this type operating in a TEH_{01} fundamental mode, are developed, manufactured, and tested. After the spurious performance of the filters is investigated, an improved spurious response is demonstrated theoretically and experimentally for the 2-pole and 4-pole filters. Furthermore, a novel triplet structure, based on the concept of the proposed DR configuration, is introduced to provide a new approach to implement nonadjacent couplings for the realization of asymmetric filtering characteristics. The proposed filter structures are very attractive for use in low-cost high-Q mass production of wireless filter applications.

5.2 Design Considerations for Dielectric Resonator Filters

Design considerations for dielectric resonator filters include the filter Q value, spurious performance, power handling capability, and production costs [88].

The Q value provided by the DR suppliers, is the unloaded Q, not the actual filter Q. Typically, unloaded Q is the inverse of the loss tangent of the dielectric material. Besides the loss tangent, the achievable filter Q value is determined by other factors such as the size of the enclosure, support structure and tuning elements. Increasing the size of the enclosure increases the Q value of the filter. Also, the conductivity of the metal materials used for the enclosure has an impact on the Q value. A support structure, constructed of dielectric material with a low dielectric constant (e.g., ε_r = 4.5) is used to mount the dielectric resonator. A layer of adhesive material is inserted between the resonator and the support (Fig. 5.1). It is crucial to keep in mind that the support structure can significantly degrade the Q if it is not properly designed. A variation in the dielectric constant translates to a shift in the resonant frequency of a dielectric resonator. Typically, grinding machine is applied to adjust the resonator dimensions to compensate for the tolerances in the dielectric constant. However, screws are still needed to tune the resonant frequencies, and the coupling values between any two of the resonators. However, these screws degrade the Q value of the filter.

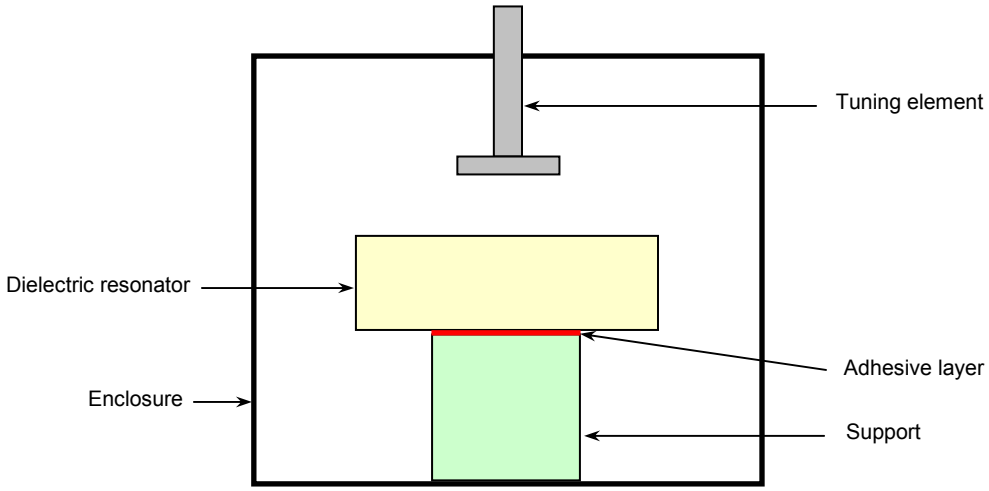

Fig. 5.1 Typical support structure of a DR resonator.

Among all known types of microwave filters (e.g., waveguide, coaxial, and etc.), DR filters exhibit the worst spurious performance. Usually, an improvement can be achieved by cascading another lowpass filter with the DR filter to eliminate some spurious modes, but at the expense of increasing the size and insertion loss. Otherwise, a specific structure (e.g., a ring resonator) must be used to suppress the spurious modes.

The thermal conductivity of the support and adhesive material are significant factors in designing high-power DR filters. The support structure should be designed to allow the heat, generated by the dielectric resonator, to be easily transferred to the metallic enclosure.

The production cost of DR filters includes the materials of the resonator and support, and involves the assembly, integration, and alignment of the dielectric resonators, a major cost item. Tuning is a must in order to meet all the specification requirements. It is this tuning process that increases the production costs of DR filters.

5.3 Configurations of the Proposed DR Filter and Support

The proposed DR filters are constructed as one piece from a substrate of high-K materials. All the dielectric resonators are connected one to another by the same high-K dielectric material, resulting in a piece which can be efficiently and accurately cut to the desired dimensions. Thus, for a DR filter operating at the single mode, the assembly of the N-pole filter reduces from the assembly of N individual resonators to the assembly of one dielectric substrate. To support the new DR filters, a corresponding mounting structure is proposed. The DR filters and the support structure are combined by a layer of adhesive so that they can easily fit inside the filter housing. Thus, the complexity of the assembly process is substantially reduced.

5.3.1 High-K Ceramic Dielectric Substrates

The commercially available Trans-Tech [92] high-K ceramic substrates that are used to construct the proposed DR filters are represented in Fig. 5.2. The composition of the material is a blend of $BaTi_4O_9$ and $Ba_2Ti_9O_{20}$. The employed substrate, which is the same as the one for the traditional dielectric resonators, has a thickness of 3.5mm, a dielectric constant of 38.6.

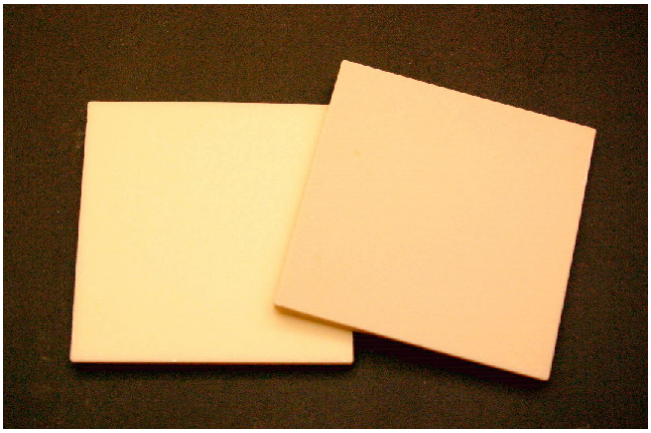

Fig. 5.2 Trans-Tech high-K ceramic substrates used to construct the proposed DR filters.

5.3.2 Proposed DR Filter Configurations

Fig. 5.3 illustrates two feasible resonator configurations that are easily machined from a single piece of the dielectric substrates, given in Fig. 5.2. The two square resonators are physically attached to each other, either at the corner or in the middle, through the same high-K material. Such structures ensure a precise spacing among resonators, since they are indeed a single piece, eliminating the need for alignment between the resonators of the conventional DR filters. The dielectric material linkage between the two resonators, along with the air gap provides the necessary electrical coupling between the two resonators. Fig. 5.4 displays the electric-field distributions of the single-mode and dual-mode of the two DR configurations, obtained by the HFSS eigenvalue solver. The resonators operate in either the TEH_{01} mode or the HEH_{11} dual mode, similar to that of conventional single-mode or dual-mode dielectric resonators, respectively.

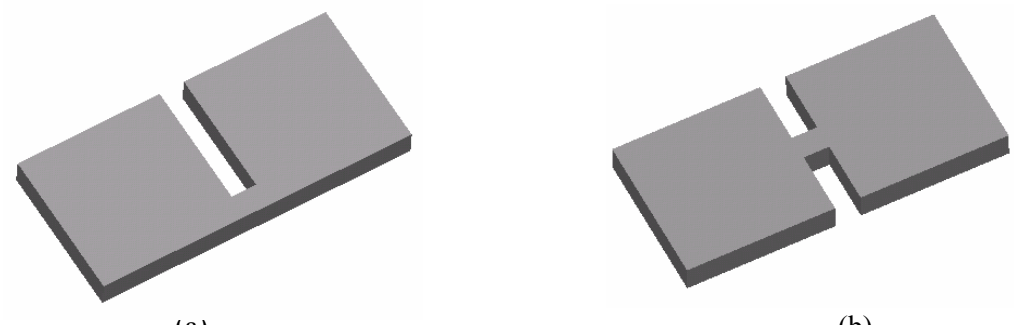

(a) (b)

Fig. 5.3 Two feasible DR configurations.

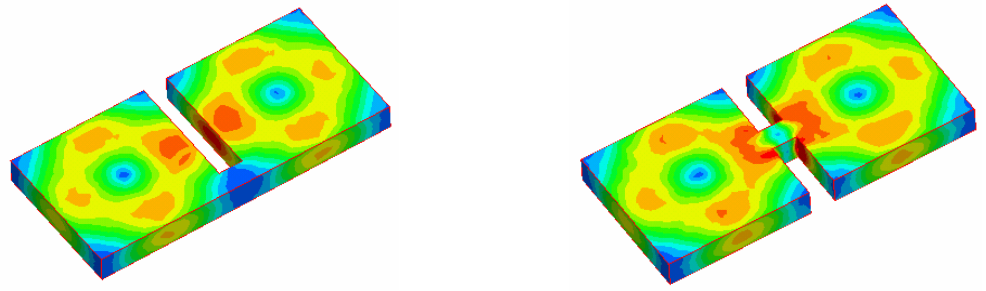

TEH_{01} mode

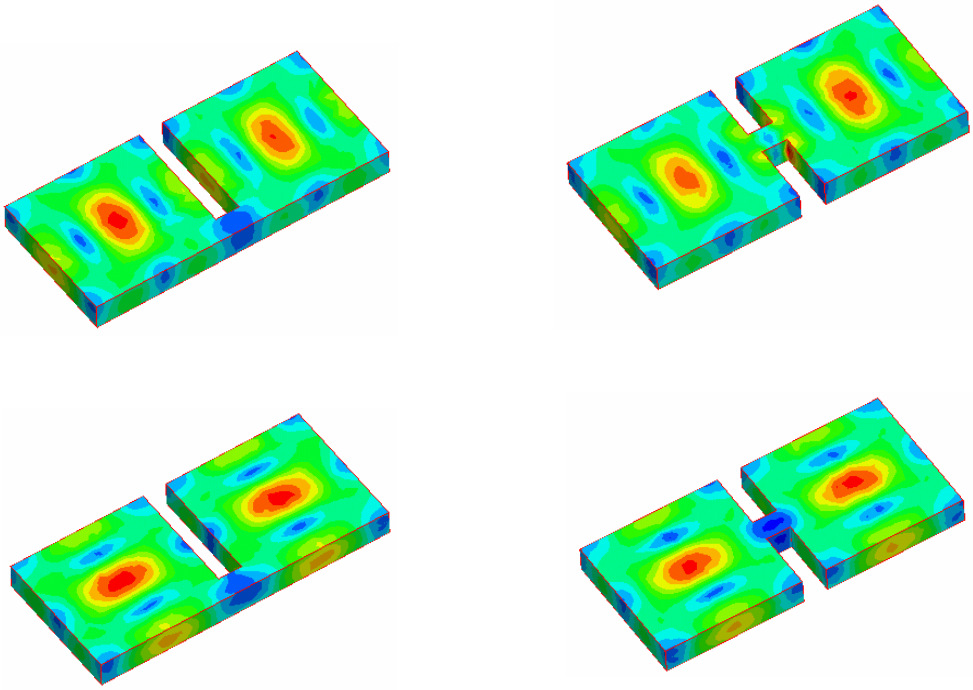

HEH_{11} dual mode

Fig. 5.4 Electric-field distributions of the two DR configurations shown in Fig. 5.3.

To implement DR filters by using the proposed DR configurations, the coupling between two connected resonators is investigated. The coupling coefficient depends on the spacing and the shape of the gap. In order to calculate the coupling, HFSS [58] EM simulations of two identical coupled resonators are carried out for various values of the inter-resonator spacing D with the calculation of the even and odd resonance frequencies f_e and f_m. The normalized coupling coefficient K is then given by $(f_e^2-f_m^2)/(f_e^2+f_m^2)$. The results of the calculated coupling coefficients, as a function of D for both proposed configurations (Fig. 5.3) with a fixed width (e.g., 1mm) W of the linkage between the two resonators are demonstrated in Fig. 5.5. It can be seen that the coupling values, generated by both proposed DR configurations in Fig. 5.3, are fairly close. As a result, either configuration can be used to construct a DR filter in terms of the coupling required in the filter design.

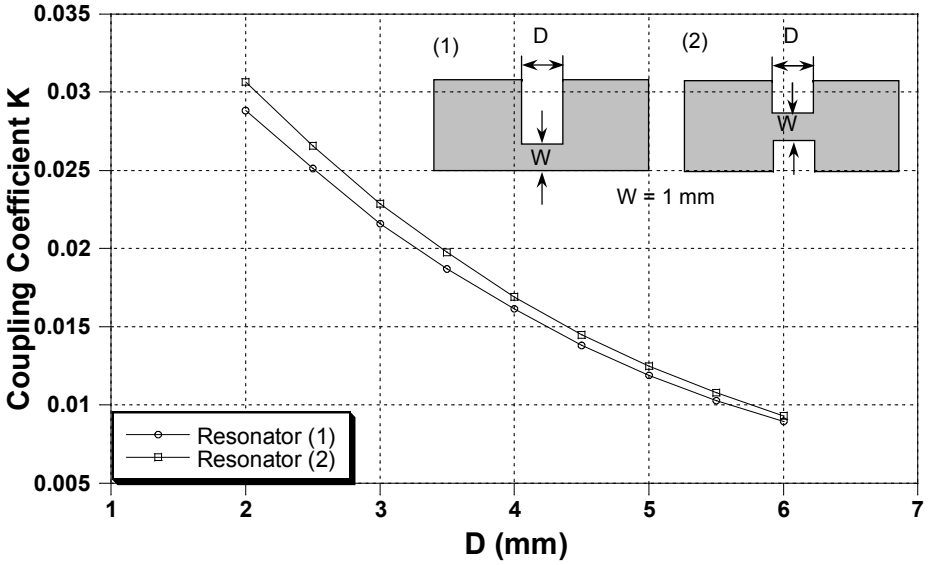

Fig. 5.5 Coupling coefficients versus D.

5.3.3 Structure of the Support

Like conventional dielectric resonators, a mounting structure is also required to support the proposed resonator structures. This prevents the direct contact of resonators with the metallic enclosure, reducing conductor losses and enhancing the unloaded Q values.

Mounting arrangements and support materials have a significant impact on the overall filter performance. Also, the support materials have to meet specific criteria such as low dielectric constant, low loss, and being mechanically stable.

The supports for the proposed DR filters are fabricated from commercially available Teflon with a low dielectric constant of 2.1 and a loss tangent of 0.0003. Teflon is also used here because it can be easily cut, sheared, and machined to the desired shape, as represented in Fig. 5.6 (a). The primary benefit of using a single piece of Teflon as the support, rather than individual cylindrical post commonly found in conventional DR filters, is that the manufacturing complexity is greatly reduced, and there is no need of alignment between the resonators and the support. The resonators can fit well into the support with the help of a low-loss adhesive layer. This structure of the support is more suitable for mounting the DR in Fig. 5.3 (a) than with the DR in Fig. 5.3 (b), since it provides a much better support for the linkage between the resonators. Therefore, the DR structure in Fig. 5.3 (a) is selected for designing all the proposed filters. The assembled structure, as conveyed in Fig. 5.6 (b), can be easily fit inside the filter housing as one piece.

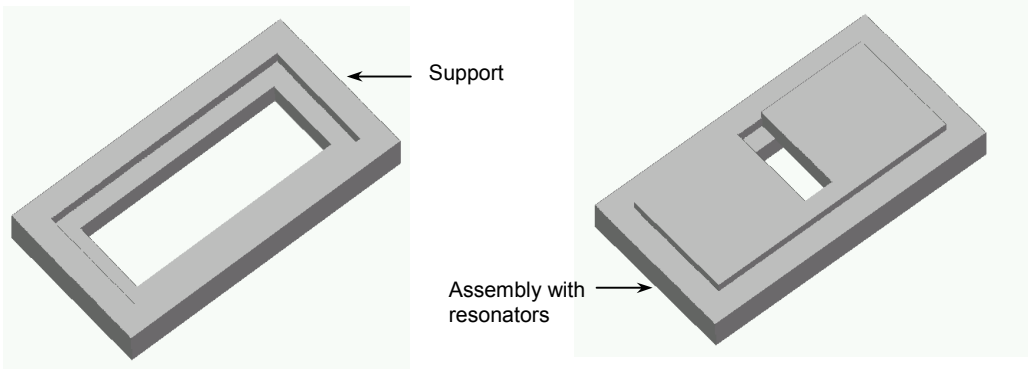

(a) (b)

Fig. 5.6 (a) Support structure and (b) the assembled support and the resonators shown in Fig. 5.3 (a).

5.4 Fabrication of the Proposed DR Filters

The most challenging part of achieving the proposed DR filter structures is to find an appropriate fabrication approach. Traditional mechanical machining fails to work on the ceramic substrates due to the hardness of the materials. Laser machining (Fig. 5.7 (a)) is relatively expensive, and is not well applicable for cutting such thick ceramic materials due to the high power and heat input. As an alternative, low-cost waterjet machining (Fig. 5.7 (b)) turns out to be very effective in machining such substrates. This technique uses a powerful stream of cold water mixed with a certain amount of fine sand, directed onto the substrate to carry out the cutting. Unlike laser machining, waterjet cutting has the unique advantage that there is no heat input to distort the material. At the same time, the machining is computer controlled, leading to a highly precise and efficient process.

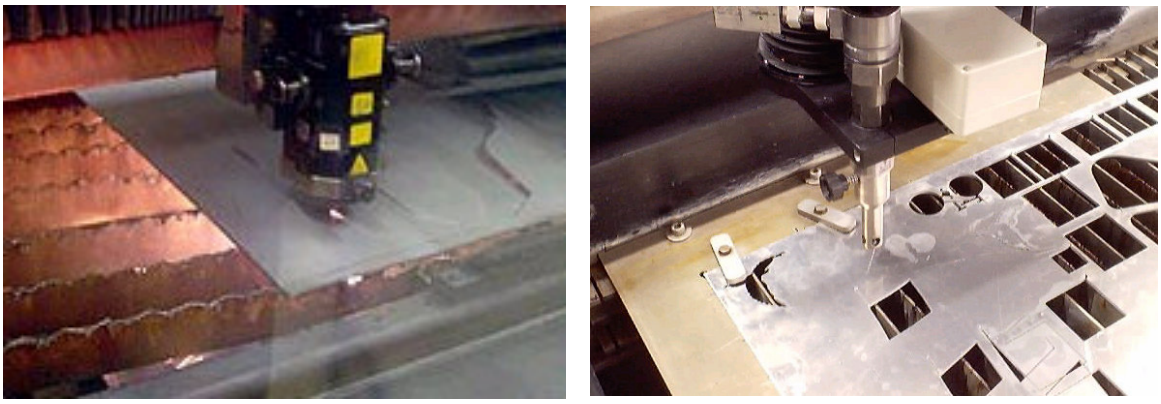

(a) (b)

Fig. 5.7 Available fabrication methods: (a) laser machining and (b) waterjet machining.

5.5 DR Filter Designs

To implement DR filters by using the proposed dielectric resonator configurations, mode charts, internal and external couplings of the DR filters are investigated. Several filters of this type operating in the TEH_{01} fundamental mode are designed, fabricated, and measured. The

spurious performance of the filters is investigated, and the theoretical designs of the filters are confirmed and supported by measurement results.

5.5.1 Mode Chart

Typically, DR filters exhibit an excellent in-band performance, but poor out-of-band spurious characteristics due to the crowded mode spectrum. The rule of design in achieving a DR filter with a wide spurious-free performance is to use a mode chart to select the resonator dimensions that provide a well-spaced mode spectrum.

For high-K ceramic substrates with a dielectric constant of 38.6 from Trans-Tech, the available thickness of the substrates varies from less than 1mm up to several millimetres. For the quality factor and spurious performance, it is critical to select the appropriate thickness of the substrate. Fig. 5.8 shows a mode chart that describes the effects on the resonant frequency when substrates with a thickness of 3.5mm are selected.

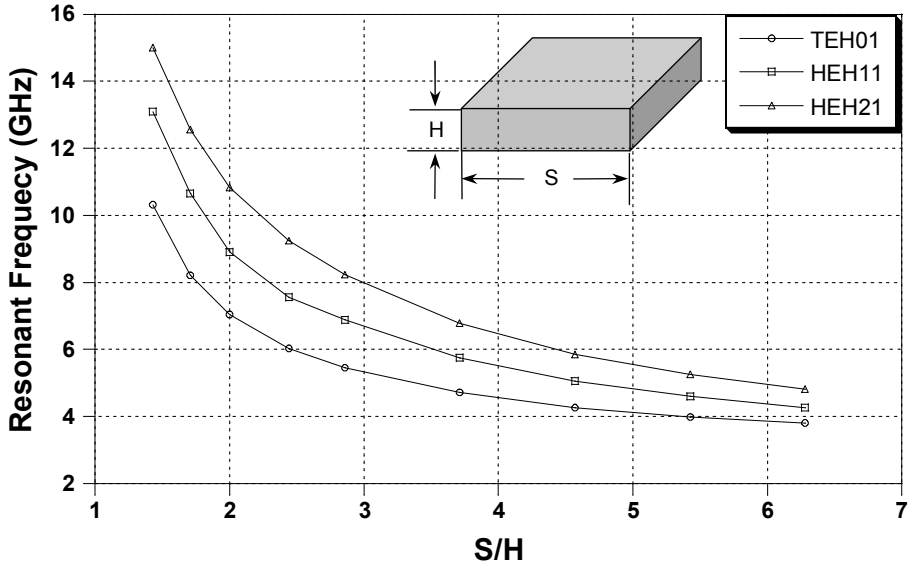

Fig. 5.8 Mode chart of a DR made from Trans-Tech ceramic materials with a dielectric constant of 38.6 and a thickness of 3.5mm.

5.5.2 Internal and External Coupling

The design of the proposed DR filters follows the standard filter synthesis steps. The internal coupling between the two adjacent resonators and external (input/output) coupling are synthesized from the elements of the filter coupling matrix.

To implement a 2-pole filter, the simple coupling structure, illustrated in Fig. 5.3 (a) is used. Spacing *D* between the two resonators and width *W* of the linkage between the two resonators determines the inter-resonator coupling. The coupling coefficients are calculated as a function of *D* and *W*, and the corresponding results are given in Fig. 5.9. When *D* is fixed, the coupling decreases as *W* increases. When *W* is fixed, the larger value of *D* leads to a smaller coupling.

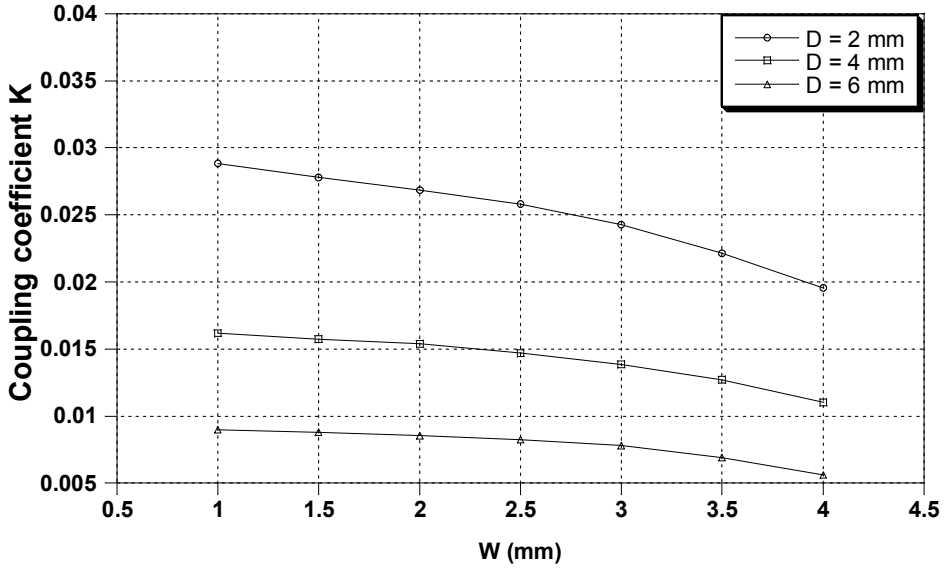

Fig. 5.9 Coupling coefficient versus *W*.

In the newly designed 2-pole filter, a *W* of 3mm is chosen for both the RF performance and the solidity of the filter structure. The corresponding specified correlation, between the coupling coefficient and spacing *D*, is given in Fig. 5.10. From it, the value of spacing *D* can be determined with the knowledge of the required coupling value.

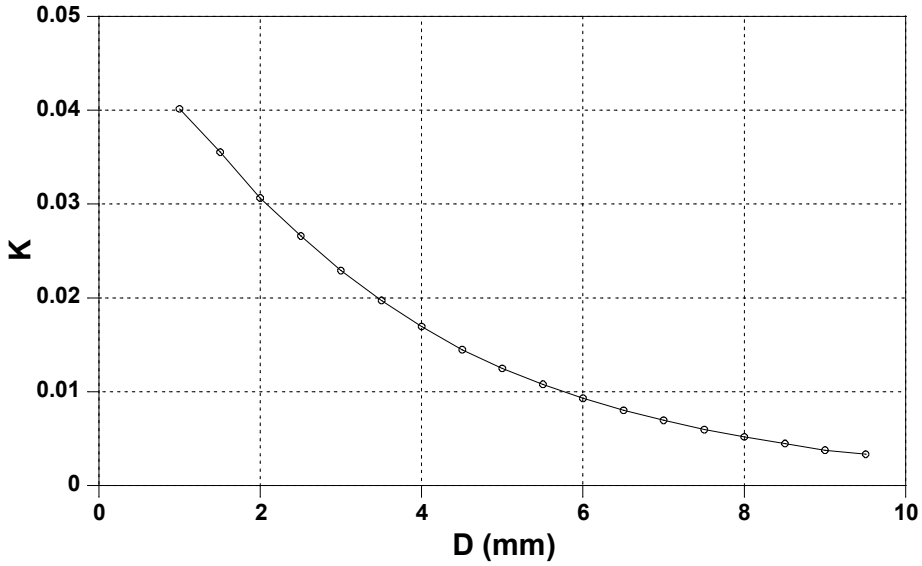

Fig. 5.10 Coupling coefficient versus D (W = 3mm).

The external couplings are attained by using coaxial probes. The probes are placed co-directional with the electric-field of the I/O resonators to excite the TEH_{01} mode inside the resonators. The desired external Q is obtained by varying the I/O coupling between the probes and the end resonators [68] by changing the length L of the probes, as depicted in Fig. 5.11. The calculated external quality factor Q_e, as a function of the probe length, is presented in Fig. 5.12.

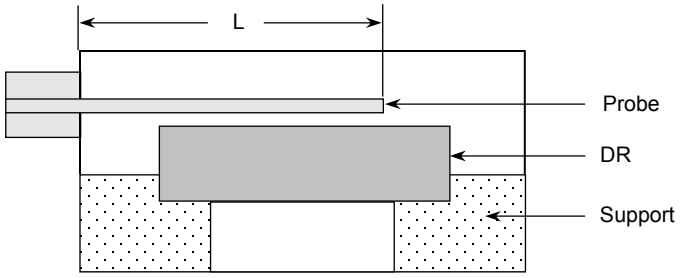

Fig. 5.11 Simulation model of the external quality factor (side view).

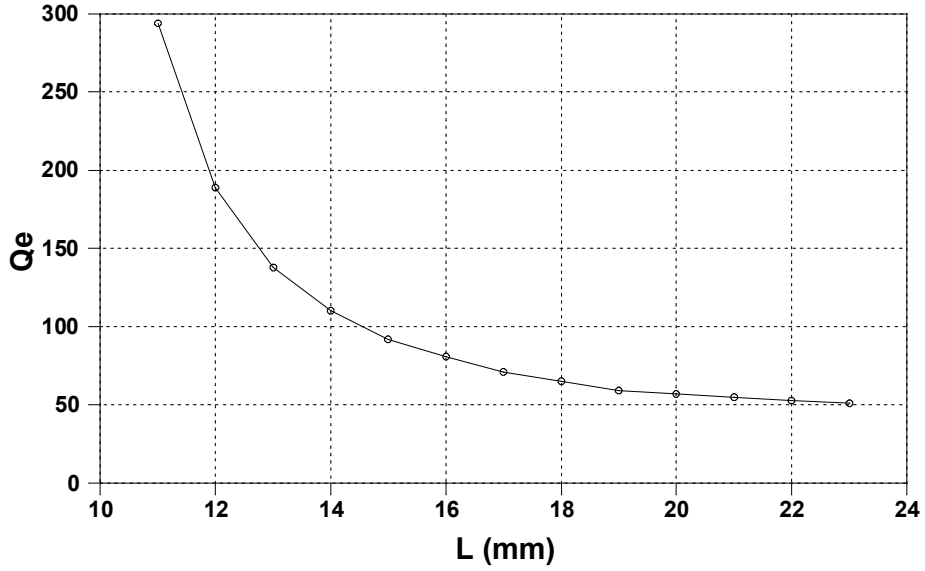

Fig. 5.12 Calculated external quality factor versus L.

5.5.3 2-Pole DR Filters

To achieve a Chebyshev 2-pole filter with a passband ripple of 0.04dB, a centre frequency of 4GHz, and a bandwidth of 40MHz, the internal coupling value $K = 0.01662$ and the external quality factor $Q_e = 66$ are required. The corresponding dimensions of the resonators can then be determined from Fig. 5.10 and Fig. 5.12. The designed filter is precisely machined with the desired dimensions and mounted in a metallic enclosure. The enclosure is manufactured from copper, in two parts: a body and a lid. When fine tuning is necessary, tuning screws for adjusting both resonant frequency and couplings can be inserted through the holes in the lid.

A 2-pole DR filter, based on the proposed concept, is designed with a centre frequency of 4GHz and a bandwidth of 40MHz (i.e., a relative bandwidth of 1%). In the design procedure all the relevant geometrical features, including the dielectric resonators, the support, and the metallic enclosure are taken into account. Fig. 5.13 gives a photograph with the assembly of the fabricated 2-pole DR filter. The measured in-band results of the filter are

shown in Fig. 5.14 in comparison with the simulation results. The centre frequency is slightly lower than 4GHz due to the tolerance of the dielectric constant of the ceramic substrate.

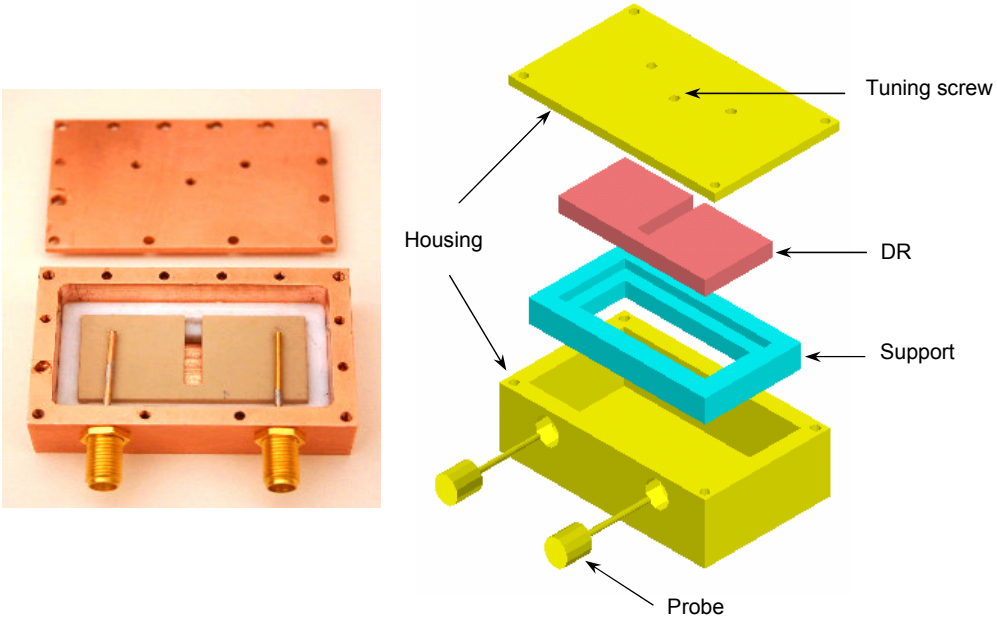

Fig. 5.13 Photograph and the assembly of the fabricated 2-pole DR filter.

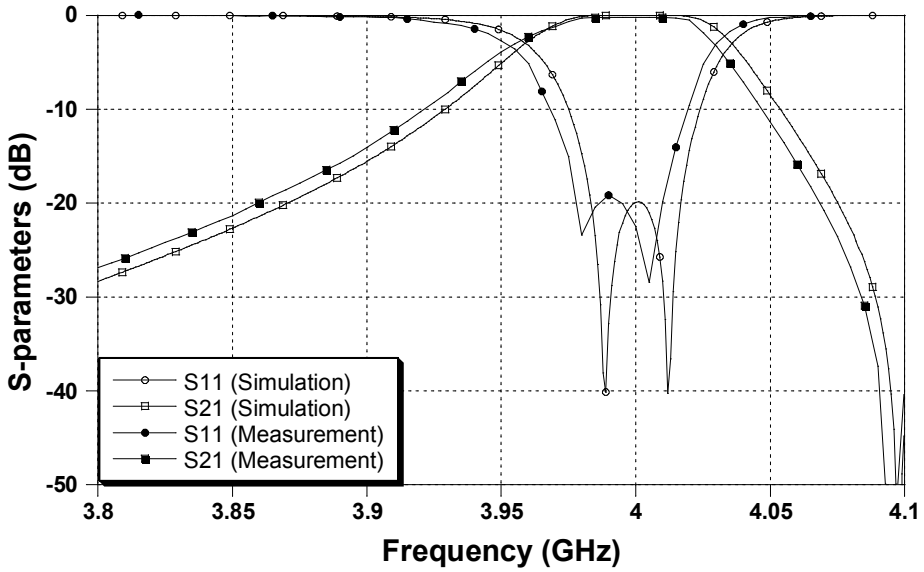

Fig. 5.14 Simulation and measurement results of the fabricated 2-pole DR filter shown in Fig. 5.13.

In addition, the spurious performance of the 2-pole filter is examined. Fig. 5.15 denotes the simulated and measured wideband frequency responses of the fabricated 2-pole DR filter in Fig. 5.13. According to the prediction of the mode chart in Fig. 5.8, the first spurious frequency is the HEH_{11} mode which should appear at 4.6GHz. There is another spurious resonance that shows up at 4.18GHz. The simulated two-dimensional electric-field distribution of the filter, at 4.18GHz, is plotted in Fig 5.16. It shows that this undesirable spurious mode is the result of the filter configuration with two resonators connected to each other. Furthermore, Fig. 5.16 provides valuable information for the suppression of this unwanted mode. It is indicated that this mode can be significantly suppressed (i.e., moved to a higher frequency) by making a circular hole along the axis of the resonator; yet, the fundamental passband performance remains unchanged, since the fundamental mode has a zero electric-field along the axis, whereas the spurious mode has an electric-field that is concentrated in the middle of the resonator.

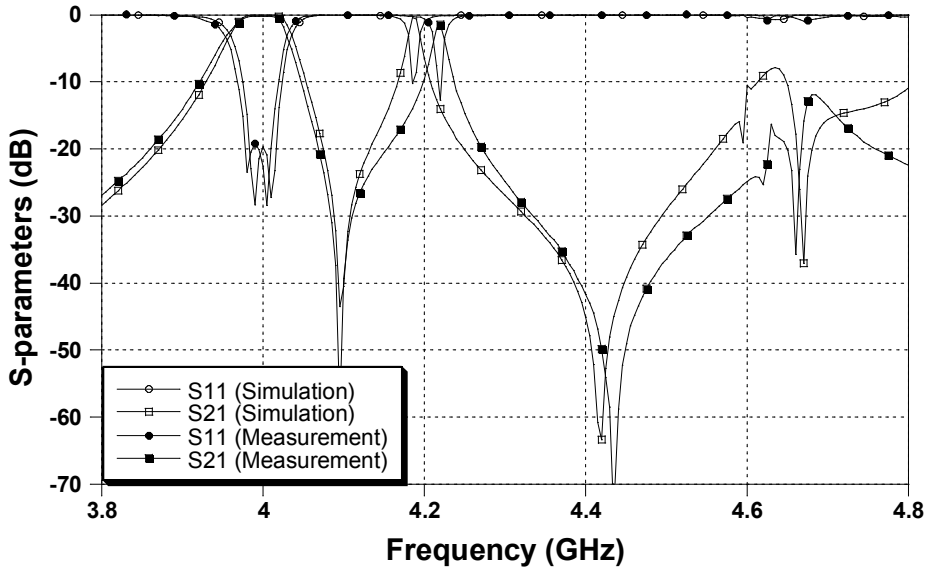

Fig. 5.15 Wideband frequency responses of the fabricated 2-pole DR filter shown in Fig. 5.13.

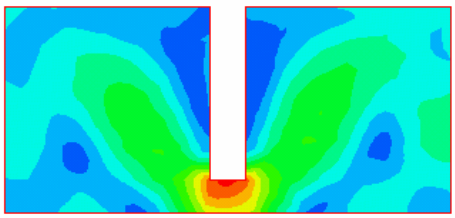

Fig. 5.16 Two-dimensional electric-field distribution of the 2-pole DR filter (Fig. 5.13) at 4.18GHz.

A modified 2-pole DR filter with concentric holes drilled through the resonators is designed and fabricated, as shown in Fig. 5.17. To achieve the required internal and external coupling, the size of the resonators and the spacing between them are changed. The concentric holes can be easily drilled by waterjet machining with the precise positions and dimensions as designed. Fig. 5.18 presents the corresponding simulated and measured results of this new filter, where the spurious-free stopband is increased from 180MHz to 600MHz. The maximum insertion loss in the passband of the 2-pole filter (Fig. 5.17) is 0.25dB, and an unloaded Q of approximately 5,000 is achieved. The Q-factor incorporates the conductor losses and the dielectric losses of the resonator and its surroundings. In particular, it is degraded due to the insertion of the tuning screws, which damage the filter performance, caused by the screw loss and screw self-resonance. A much better Q can be achieved with the use of the recently developed high-Q dielectric materials, as well as with the use of silver or gold-plated housing and tuning screws.

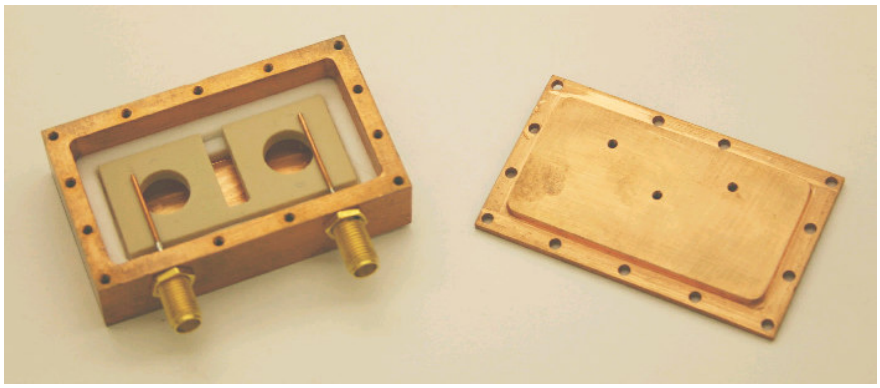

Fig. 5.17 Modified 2-pole DR filter with concentric holes in the resonators.

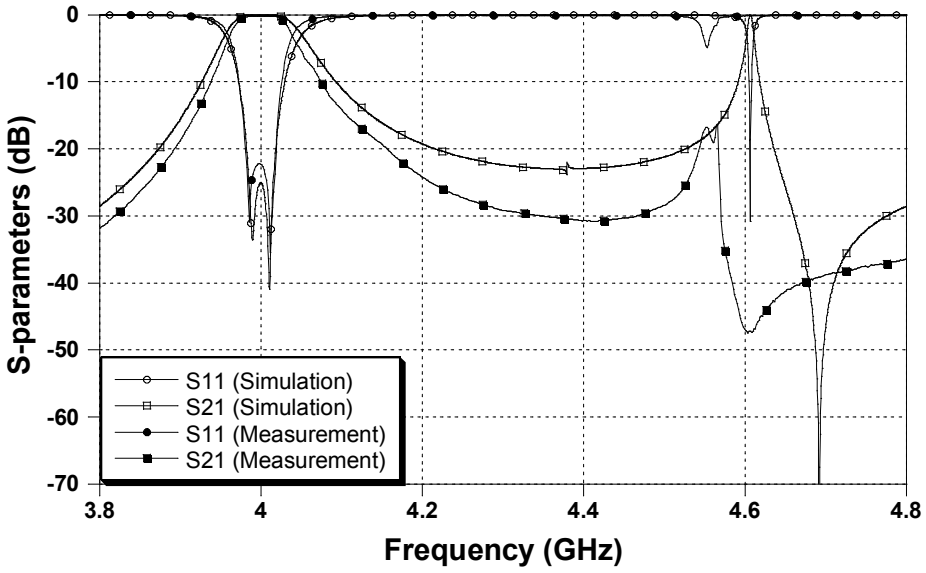

Fig. 5.18 Simulation and measurement results of the fabricated 2-pole DR filter shown in Fig. 5.17.

5.5.4 4-Pole DR Filters

The successful design of the 2-pole DR filters makes it possible to implement higher order DR filters by using the same concept. As a result, a 4-pole DR filter is designed and built. To achieve a Chebyshev 4-pole filter with a passband ripple of 0.04dB, a centre frequency at 4GHz and a bandwidth of 40MHz, the inter-resonator coupling value $K_{12} = K_{34} = 0.0091$, $K_{23} = 0.007$ and the external quality factor $Q_e = 93$ are required. However, for the 4-pole filter, when the effects of the coupling from other adjacent or nonadjacent resonators are introduced, the centre frequencies of each resonator vary slightly, thus, the resonator dimensions require further adjustment in order to maintain the same centre frequency.

A photograph with an assembly of the designed and fabricated 4-pole DR filter is given in Fig. 5.19. To eliminate the mutual coupling between the input and output resonators, the built-in shielding fin is employed. Fig. 5.20 signifies the simulated and measured in-band performances of the filter. A transmission zero appears in the upper frequency band and is attributed to a small stray coupling.

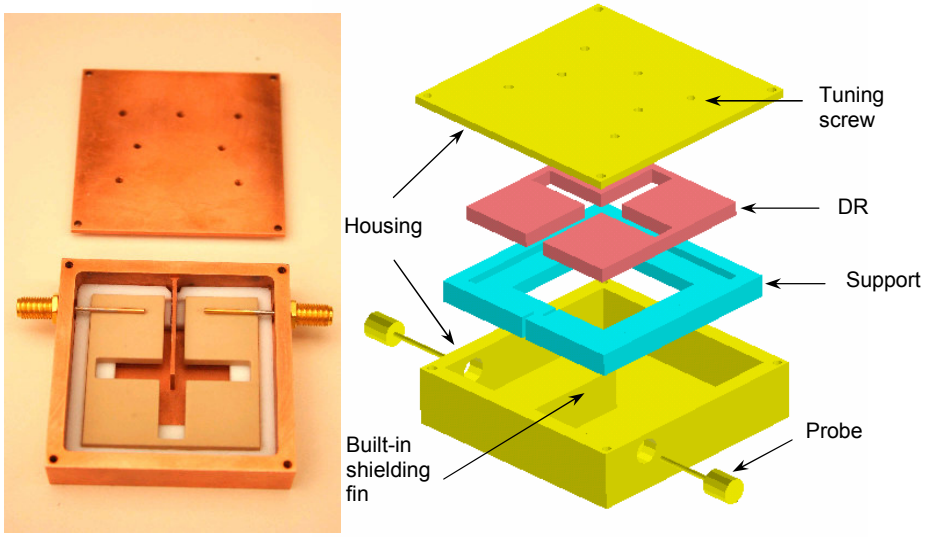

Fig. 5.19 Photograph and the assembly of the fabricated 4-pole DR filter.

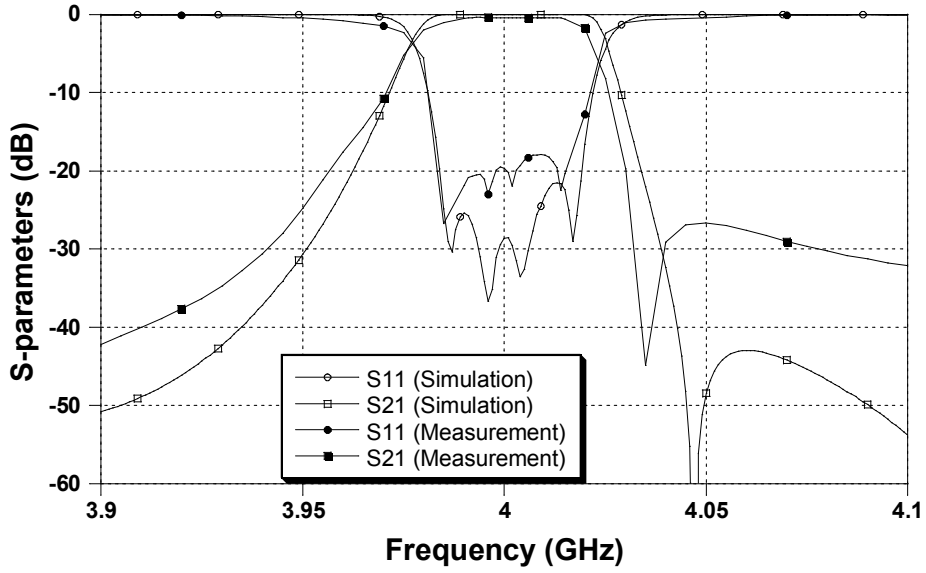

Fig. 5.20 Simulation and measurement results of the fabricated 4-pole DR filter shown in Fig. 5.19.

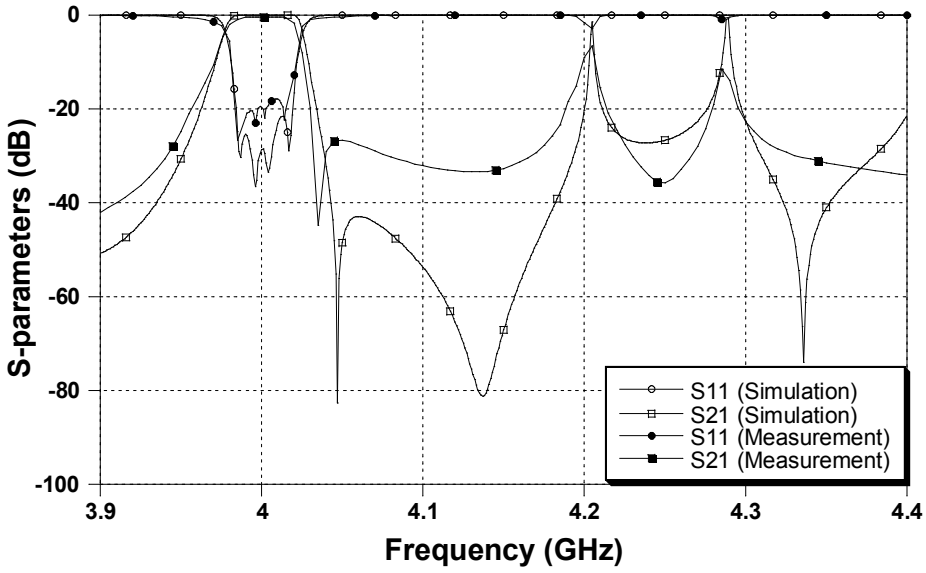

Fig. 5.21 Spurious responses of the fabricated 4-pole DR filter shown in Fig. 5.19.

Fig. 5.21 demonstrates the spurious responses of the fabricated 4-pole filter in Fig. 5.19. Similarly, the first spurious appears at 4.2GHz due to the integration of the four resonators as a single piece, whose electric-field distribution at the spurious frequency is shown in Fig. 5.22. To suppress the unwanted spurious response at 4.2GHz, a new 4-pole DR filter with concentric holes in the resonators and a cross-shaped built-in fin in the housing, as shown in Fig. 5.23, is designed and fabricated.

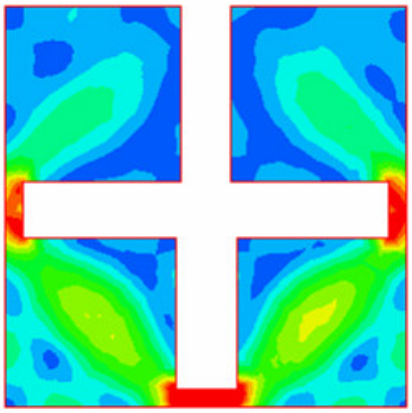

Fig. 5.22 Two-dimensional electric-field distribution of the 4-pole DR filter (Fig. 5.19) at 4.2GHz.

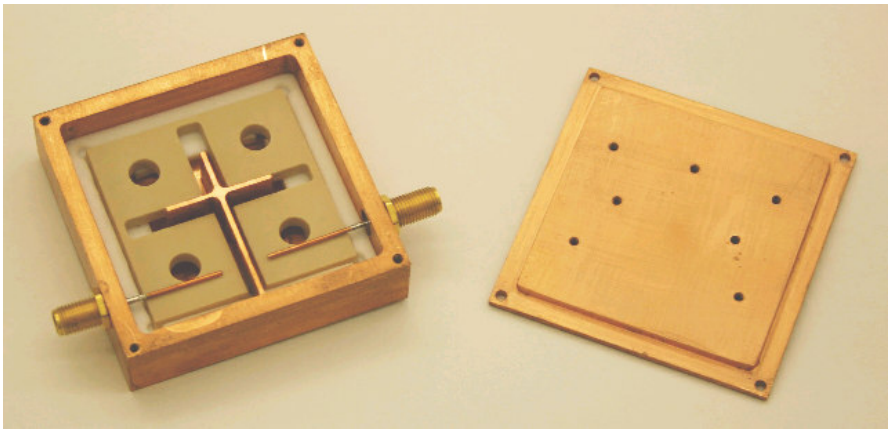

Fig. 5.23 Modified 4-pole DR filter with concentric holes in the resonators.

Fig. 5.24 illustrates a configuration to calculate the coupling coefficient for designing the filter shown in Fig. 5.23. A plot of the calculated coupling coefficient as a function of D with a fixed width but different length L of the built-in fin is drawn in Fig. 5.25. Fig. 5.26 offers the corresponding simulated and measured results of the modified 4-pole DR filter design (Fig. 5.23). The spurious-free stopband is increased from 200MHz to 480MHz, and the maximum insertion loss in the passband of the filter (Fig. 5.23) is 0.4dB. An unloaded Q of about 5,000 is achieved. The use of Trans-Tech materials with a dielectric constant of 45, where $Q \times f = 50{,}000$ would lead to a much higher Q value.

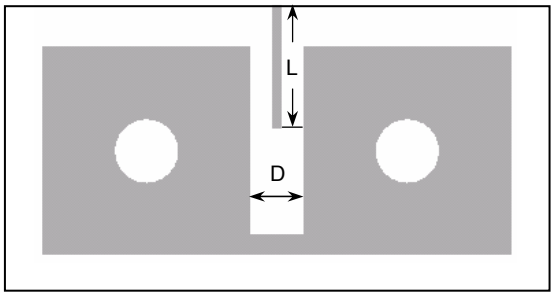

Fig. 5.24 Simulation model of the inter-resonator coupling coefficient (top view) for the design of the 4-pole filter shown in Fig. 5.23.

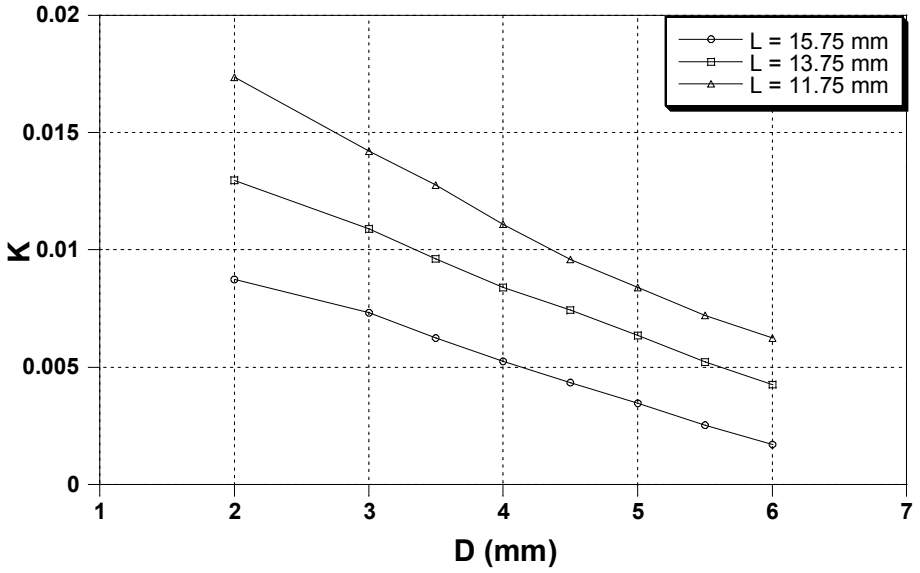

Fig. 5.25 Calculated coupling coefficient versus spacing D between two resonators with the different iris length L.

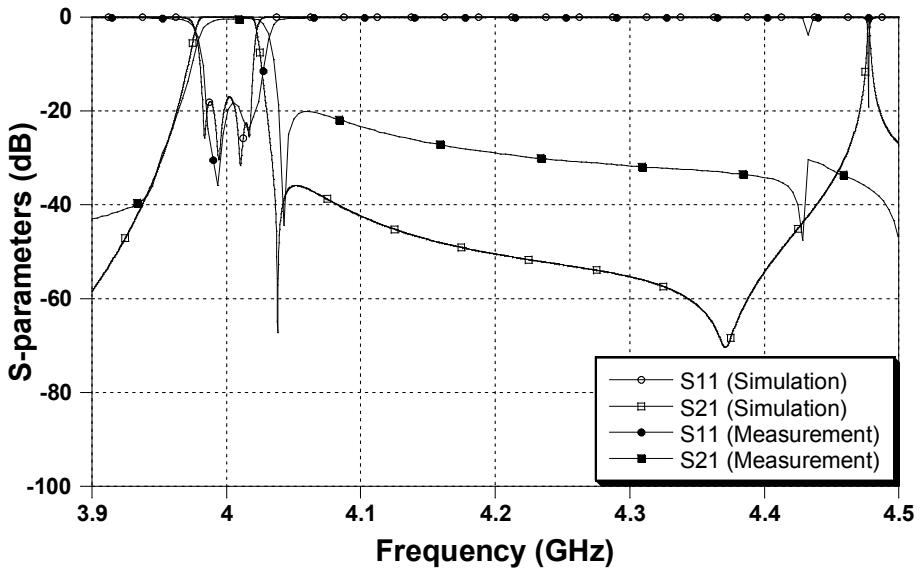

Fig. 5.26 Simulation and measurement results of the fabricated 4-pole DR filter shown in Fig. 5.23.

5.5.5 Triplets

In the conventional DR triplet in Fig. 5.27 (a), an asymmetric filtering characteristic is obvious; that is, the cross coupling implemented by an iris between input and output resonators produces a transmission zero outside the passband of the frequency response. By using a coupling probe, as indicated in Fig. 5.27 (b), the location of the transmission zero can be moved from one side outside the passband to the opposite side. This approach for implementing DR triplets is quite difficult and expensive. This is due not only to the complexity of the integration and the alignment of the resonators, but also to the additional efforts to assemble a probe between the I/O resonators when it is necessary.

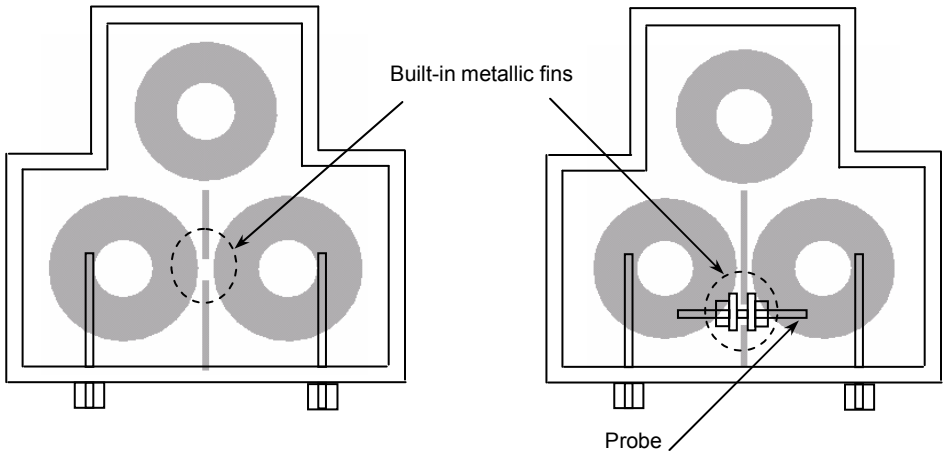

(a) (b)

Fig. 5.27 Conventional asymmetric filtering functions: (a) a triplet with positive cross coupling and (b) a triplet with negative cross coupling by using a probe between the input and the output resonators.

A new triplet structure, based on the proposed DR configuration, is employed to realize asymmetric filtering functions. Fig. 5.28 (a) shows a layout of the novel triplet structure. Three resonators are connected all together since they are machined in one piece from a ceramic dielectric substrate. The same Teflon support for mounting the 2-pole and 4-pole filters also is used to support the triplet. The connecting dielectric material between the input and output resonators provides the required cross coupling to realize a transmission zero. This triplet structure simplifies the assembly, integration, and alignment of the resonators, reducing the time and production costs. More importantly, the presence of the physical linkage between the input and output resonators provides the capability of changing the sign of the cross coupling, which then relocates the transmission zero from one side to the

opposite side of the passband response. As demonstrated by the layout in Fig. 5.28 (b), this can be easily achieved in practice by simply placing a stripe line on the surface of the dielectric linkage by means of photo-etching, metallic ink printing, or attaching a piece of metallic tape with the designed dimensions. No additional probe is needed at all. This proposed configuration can further reduce the complexity of the manufacturing of the triplet while providing the desired asymmetric filtering characteristic.

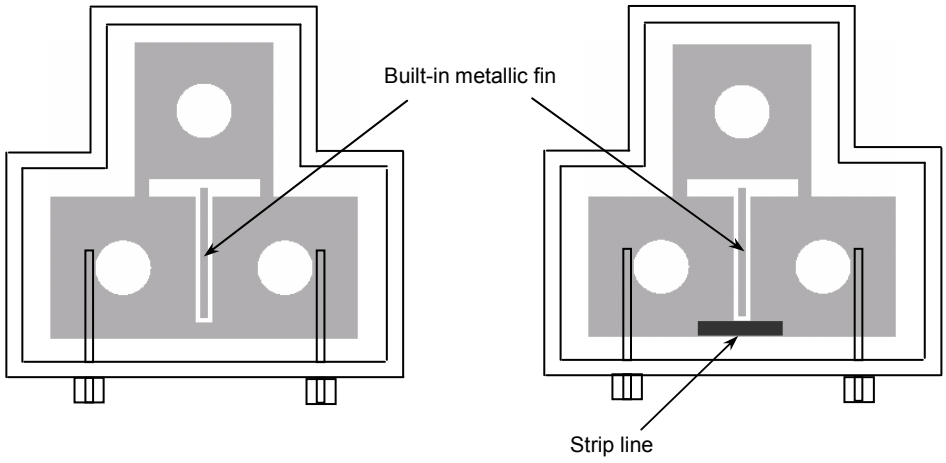

(a) (b)

Fig. 5.28 Proposed asymmetric filtering functions: (a) a triplet with positive cross coupling and (b) a triplet with negative cross coupling by placing a strip line on the dielectric substrate between the input and the output resonators.

Once the two triplets are designed, they are fabricated according to the layouts in Fig. 5.28. Photographs of the fabricated DR triplets are shown in Fig. 5.29, and the simulation and measurement results are graphed in Fig. 5.30. Obviously, there is a transmission zero in the upper frequency band of the triplet in Fig. 5.29 (a), and the transmission zero moves to a lower frequency band when a strip line is introduced to the triplet in Fig. 5.29 (b).

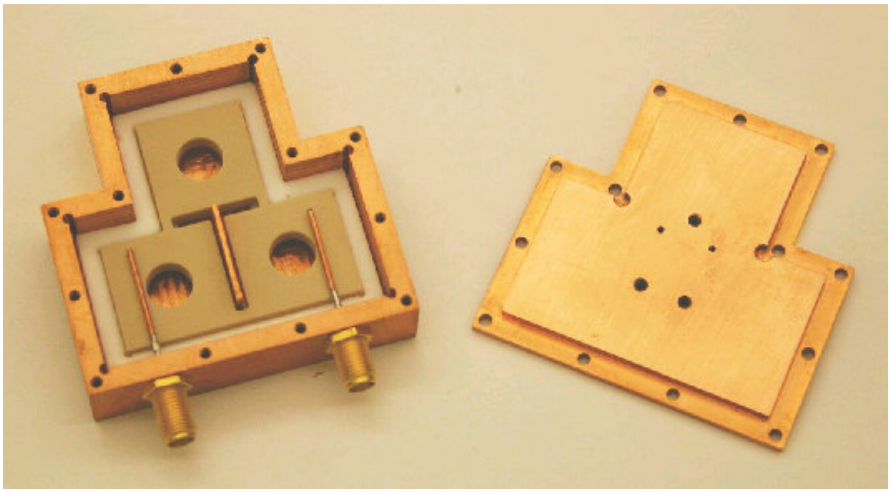

(a)

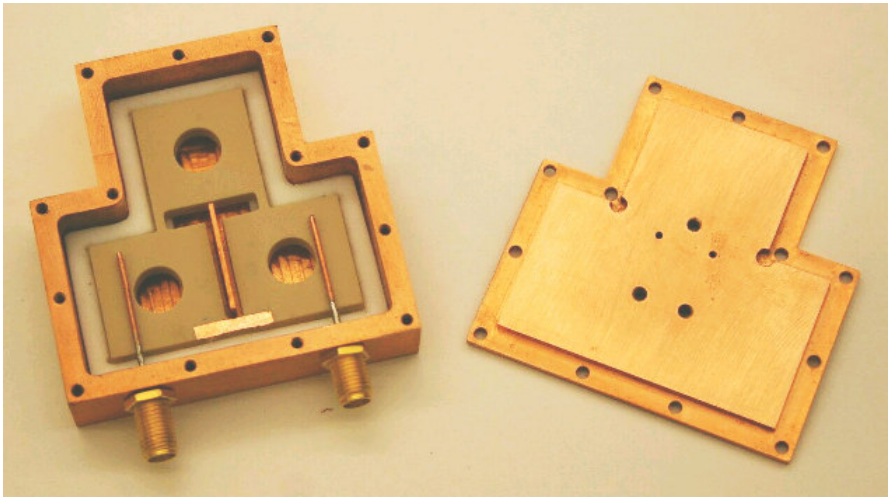

(b)

Fig. 5.29 Two fabricated DR triplets: (a) without a strip line and (b) with a strip line on the dielectric substrate between the input and the output resonators.

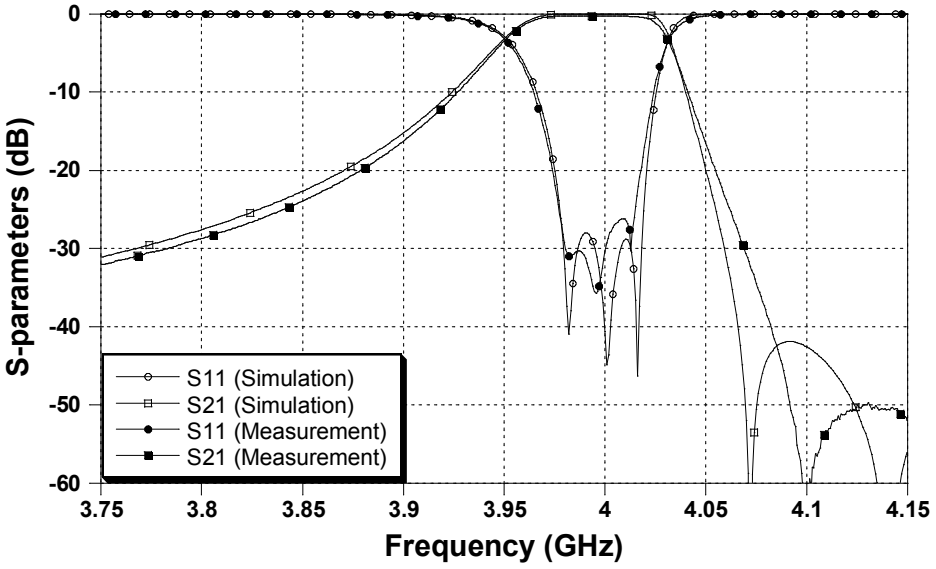

(a)

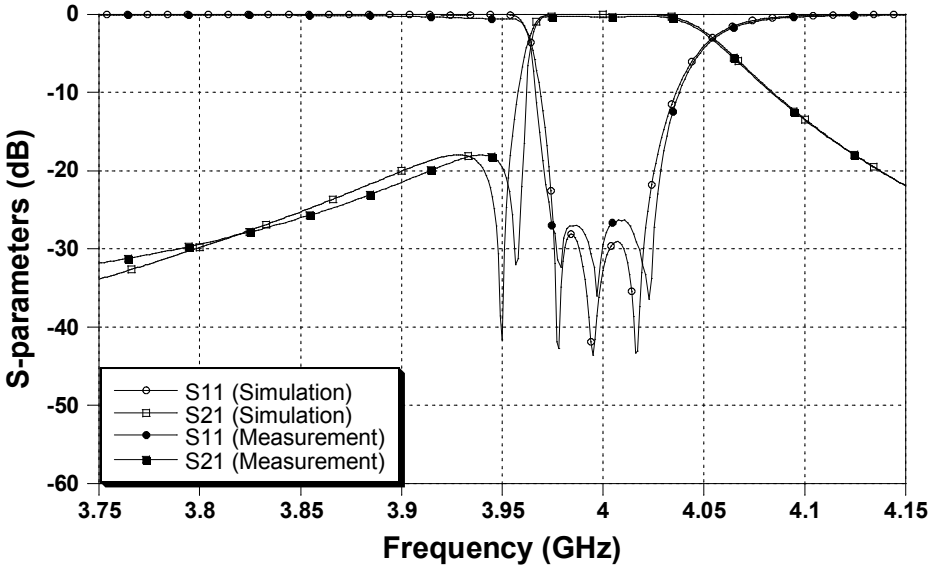

(b)

Fig. 5.30 Simulation and measurement results of the two fabricated DR triplets: (a) results of the triplet shown in Fig. 5.29 (a) and (b) results of the triplet shown in Fig. 5.29 (b).

5.6 DR Diplexer Design

In all communication systems, diplexers and multiplexers are essential components for channel separation [48, 93-96]. For example, a diplexer is usually used for a multi-frequency transceiver system in an RF front end. Diplexers consist of a transfer junction, terminated with bandpass filters of different passband frequencies at each of the two output ports. The demand for large quantities of compact, low-loss and low-cost diplexers that can adapt to various frequency bands requires a variety of filter structures. Typically, the filters for diplexers are constructed of metal waveguides because of their low loss and high isolation [97-99]. However, such filters are quite bulky. DR filter is another good candidate for realizing diplexers due to its advantages of a low loss, a high Q and small size [47, 100]. This type of diplexer comprises two DR filters (channels), connected to a three-port junction which is either a waveguide or a coaxial structure. The cost involved with the assembly, alignment, and integration of the DR filters and the junction is the primary contribution to the overall cost of the DR diplexers.

The novel DR configuration for low-cost mass production of DR filters has been presented in Section 5.5 of this chapter [90, 91]. This concept can be applied to achieve a DR diplexer with low costs. The new DR diplexer configuration eliminates the need of the integration of either a waveguide or a coaxial junction with two channel filters. As a result, for a DR diplexer of this type, the assembly of the two filters and the junction reduces the traditional assembly of individual filters and the junction to the assembly of only one dielectric substrate.

5.6.1 Channel Filters

The construction of diplexers classically starts from two signal channels and a three-port junction that are separately designed and combined in a specific way as to maximize performance. Each channel of the diplexer is a narrow bandpass filter. First of all, two DR bandpass filters are designed according to the configuration described in Section 5.5, to provide passbands centred at 4.6GHz and 4.8GHz, respectively, with absolute bandwidths of

40MHz (namely, 0.87% and 0.83% fractional bandwidths for transmission and reception, respectively). The filter with a centre frequency of 4.6GHz is denoted as transmit (Tx) filter, and the filter centred at 4.8GHz is denoted as receive (Rx) filter. The schematic of the DR filter is shown in Fig. 5.31. The substrate has a dielectric constant of 45, and $Q \times f = 40{,}000$, which supplied by Trans-Tech. Two strip lines on the top surface of the filter replace the long coaxial probes employed in the filter, described in Section 5.5, providing the required input/output coupling. This coupling scheme is suitable for the construction of the proposed DR diplexer. Fig. 5.32 conveys the HFSS EM simulation results of the Tx and Rx filters. The two filters have return losses of more than 20dB. The rejection of filters at each other's passband is about 20dB.

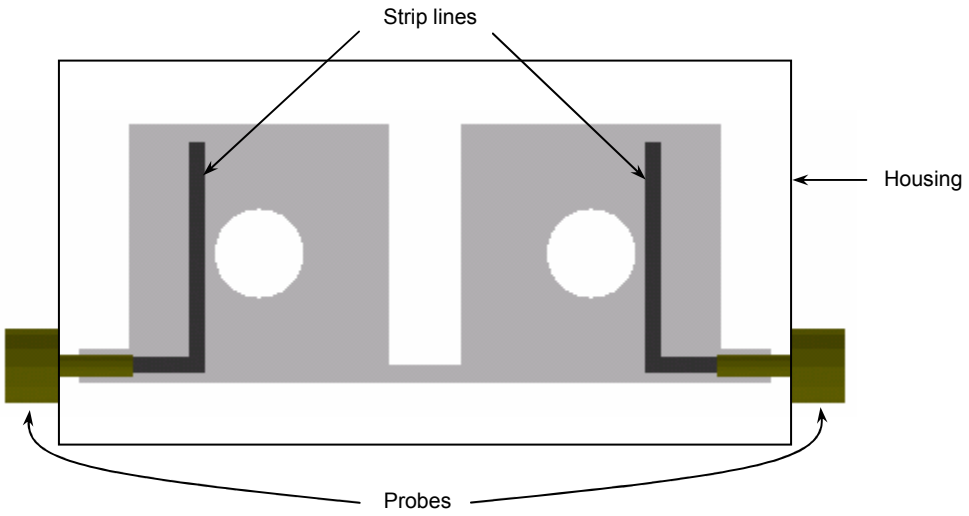

Fig. 5.31 Schematic of the designed Tx and Rx filters constructed from high-K ceramic substrates (top view).

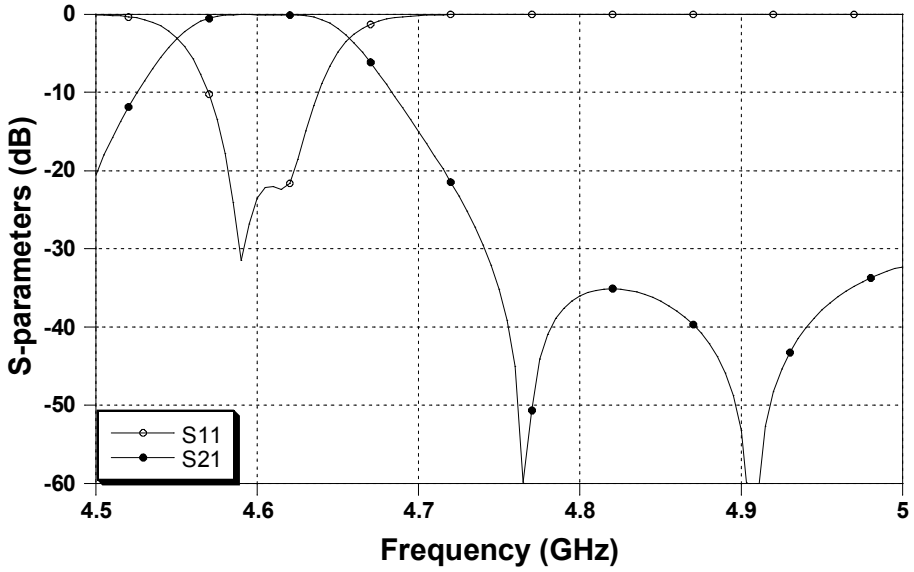

(a)

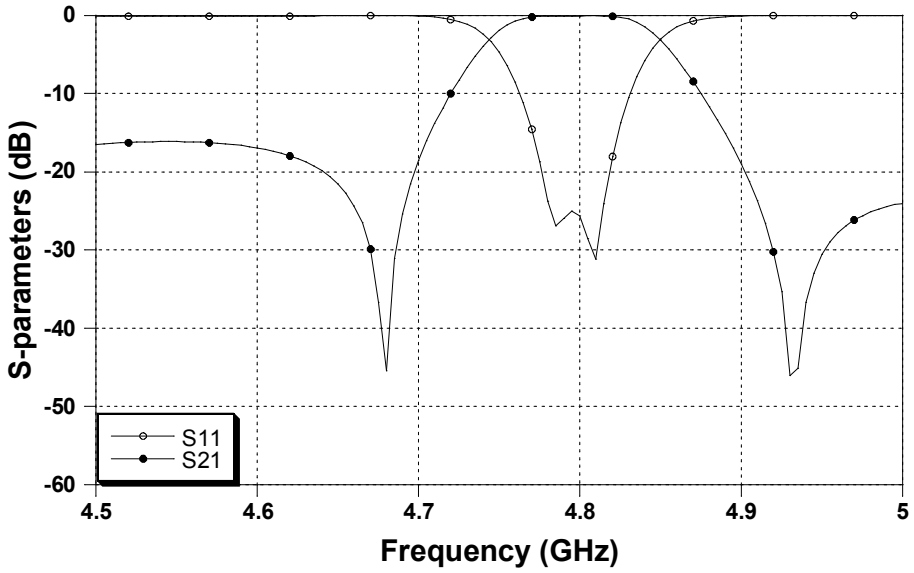

(b)

Fig. 5.32 Simulated frequency responses of the two filters: (a) Tx filter and (b) Rx filter.

5.6.2 Junction

To implement a diplexer, the designed Tx and Rx filter are connected to a three-port microstrip-line junction at its two ports in such a way that one of the filters, operating as an open circuit, matches the junction at the centre frequency of the other filter. A simple approach to fabricate the junction by using the same high-K ceramic substrate so that the device is a single piece which can be easily cut to the desired shape and dimensions simultaneously. Fig. 5.33 illustrates the schematic of the designed microstrip-line junction. The microstrip line at each port is $50\,\Omega$ at the operating frequency of the diplexer. Fig. 5.34 represents the simulation results of the three-port junction.

Fig. 5.33 Schematic of the designed microstrip-line junction using the high-K ceramic substrate (top view).

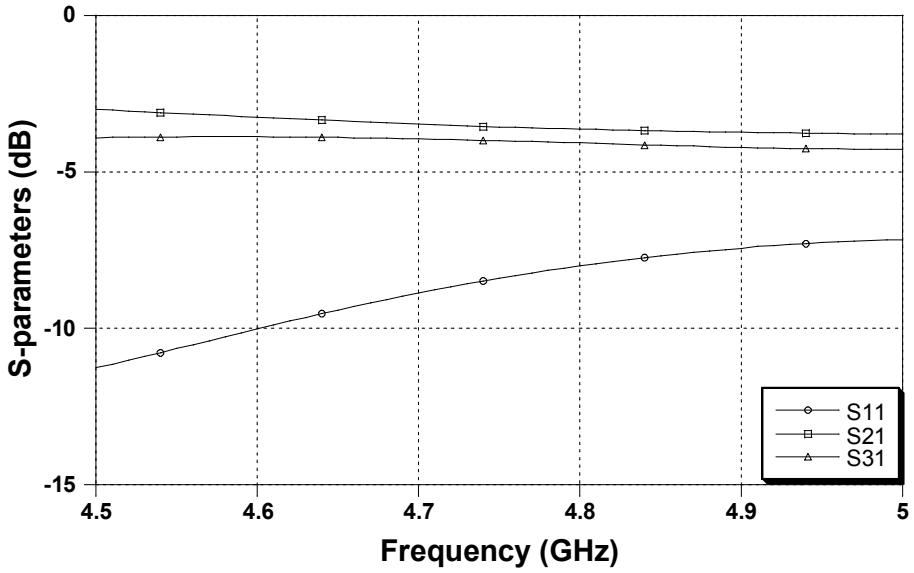

Fig. 5.34 Simulation results of the junction shown in Fig. 5.33.

5.6.3 Diplexer

The two filters designed with the configuration shown in Fig. 5.31 are then cascaded at the two ports of the junction. The schematic of the constructed diplexer is illustrated in Fig. 5.35. However, simply connecting filters and junction deteriorates the performance of the two filters in their passbands, due to the interactions of all of the individual parts. The performance of the diplexer can be improved by modifying each filter, and sometimes, an optimization of the overall structure is required.

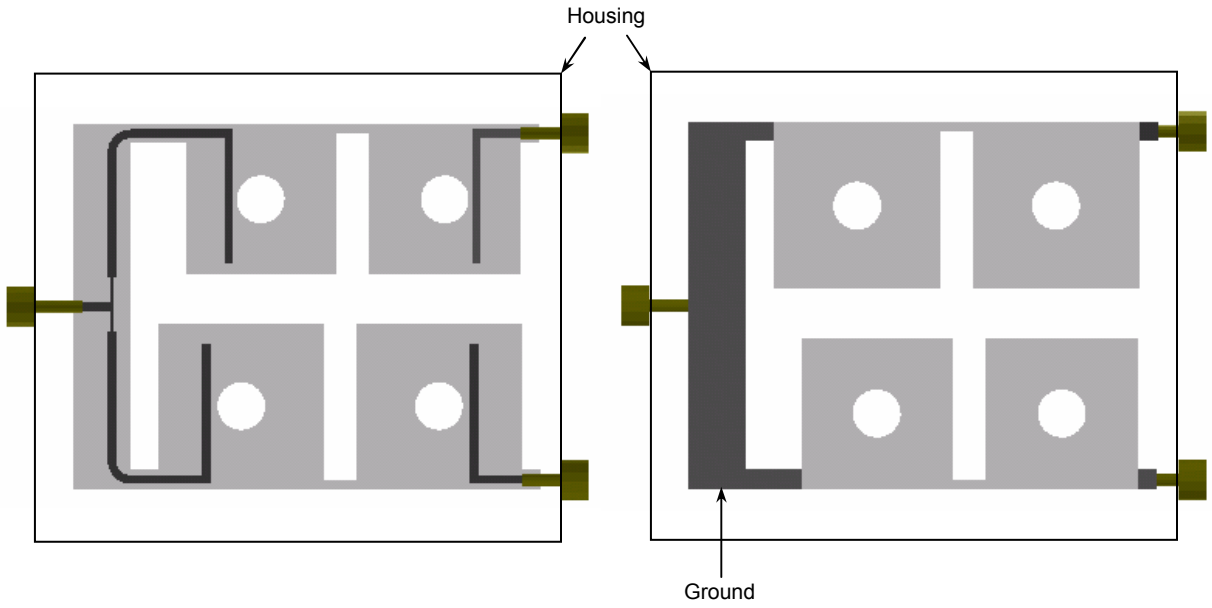

Fig. 5.35 Schematic of the constructed DR diplexer: (a) top view and (b) bottom view.

Fig. 5.36 displays the simulated frequency responses of the designed diplexer. Due to the discontinuity caused by the junction, the insertion loss of each filter in the diplexer is slightly increased from the insertion loss of the filter itself. The return loss is more than 15dB for the two frequencies, and the passband has a bandwidth of approximately 40MHz at two frequencies.

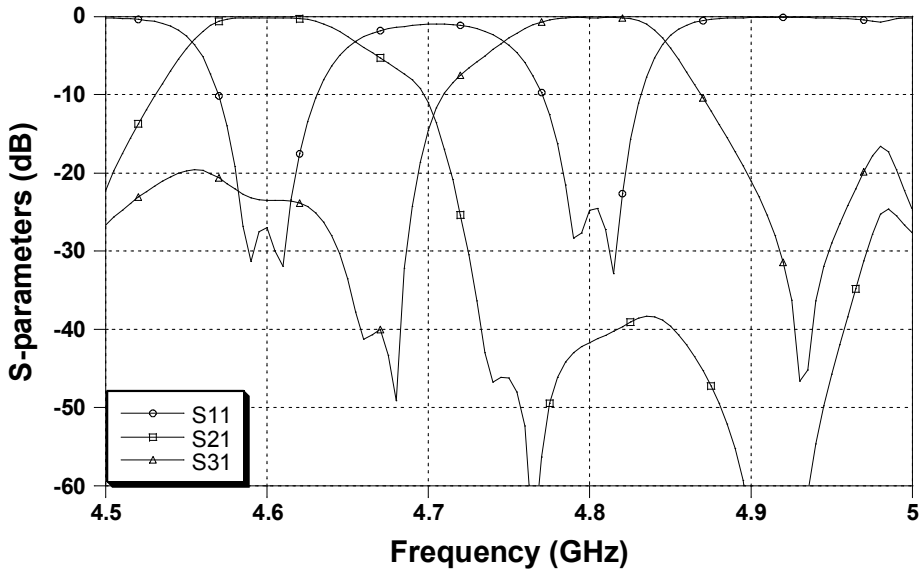

Fig. 5.36 Simulated frequency responses of the designed DR diplexer.

This type of diplexer promises to be useful in wireless base station applications. Furthermore, the concept can be also applied to implement DR multiplexers.

Chapter 6

Conclusions

6.1 Contributions of the Thesis

A novel compact microstrip lowpass filter, employing metal-loaded slots etched on the ground plane, is proposed in this thesis [80]. Various metal-loaded slot configurations are examined. Modelling results of the slots by a transmission line circuit model are in agreement with the EM simulation results. Several lowpass filters are developed, fabricated, and measured. They exhibit an excellent performance in comparison with conventional microstrip EBG filters in both the passband and the stopband. The slots in the ground plane are added to a bandpass filter to demonstrate the miniaturization achieved with the use of the proposed concept, while improving the out-of-band rejection performance. The slots in the ground plane are combined with capacitive stubs in the top surface of the substrate to realize highly miniature bandpass filters.

To realize low-loss digital and analogue tunable lowpass filters, MEMS switches and semiconductor varactors are integrated in the slots respectively [81, 82]. The proposed structure offers a low loss since the Q of the switching and tuning elements is negligible in determining the insertion loss of the filter. Other advantages of the proposed structure are its ease of assembly and application of the DC bias voltage. Several tunable filters are

developed, fabricated, and tested. A very wide tuning range is achieved. Combination of both switches and varactors can lead to an even wider tuning range.

A novel DR filter configuration, implemented as a single piece of a high-K ceramic substrate, is presented in this thesis [90, 91, 101]. It considerably reduces the cost of assembly and integration associated with conventional DR filters. A 2-pole and 4-pole filter of this type operating in the TEH_{01} fundamental mode, is developed, manufactured, and tested. After the wideband spurious performance is investigated for the designed filters, a simple approach is used to improve the spurious response. A novel triplet structure based on the proposed DR configuration presents a new simple way to implement the nonadjacent cross coupling for realizing asymmetric filtering characteristics. The proposed concept is extended and applied to implement DR diplexers, which are promises to be very useful in wireless base station applications.

6.2 Future Work

Overall, EBG-based structures are proven to exhibit broad applications to satisfy the needs of designing various microstrip circuits. The work reported in this thesis can be extended to waveguide devices employing EBG structures on the waveguide walls. Such devices will be useful in the suppression of higher order spurious modes of compact waveguide filters. An EM analysis based on combining the mode matching technique and the transverse resonance technique which was proposed in Chapter 3, should be efficient in the analysis of such types of waveguide EBG-based filters.

There are several unexplored issues in the applications of the proposed DR filters and other related devices. There is no doubt that in the immediate future, further studies and efforts are needed to finish the development, analysis, fabrication, and measurement of the DR diplexers/multiplexers, described at the end of Chapter 5. It is also believed that the same concept can be extended to metallic resonators allowing the realization of metal-loaded filters on a single metallic sheet. The development of higher order self- equalized DR filters is another research area with potential. Such filters require the use of controlled positive and

negative coupling between nonadjacent resonators which can be implemented conveniently by using the proposed DR filter structure.

References

[1] R. Qiang, Y. Wang, and D. Chen, "A novel microstrip bandpass filter with two cascaded PBG structures," *IEEE APS Symp.,* vol. 2, pp. 510-513, 2001.

[2] Y. Qian and T. Itoh, "Microwave applications of photonic band-gap (PBG) structures," *1999 Asia-Pacific Microwave Conf.,* vol. 2, pp. 315-318, 1999.

[3] Y. Qian, V. Radisic, and T. Itoh, "Simulation and experiment of photonic band-gap structures for microstrip circuits," *1997 Asia-Pacific Microwave Conf.,* pp. 585-588, 1997.

[4] A. S. Andrenko, Y. Ikeda, K. Mori, and O. Ishida, "EM analysis of PBG substrate microstrip circuits for integrated transmitter front end," *Mathematical Methods in Electromagnetic Theory Conf.,* vol. 1, pp. 295-297, 2000.

[5] V. Radisic, Y. Qian, R. Coccioli, and T. Itoh, "Novel 2-D photonic bandgap structure for microstrip lines," *IEEE Microwave Guided Wave Lett.,* vol. 8, pp. 69-71, Feb. 1998.

[6] R. Hu, X. X. Zhang, and B. X. Gao, "2-D PBG structure in microstrip line and symmetrical microstrip line," *2000 Asia-Pacific Microwave Conf.,* pp. 1218-1221, 2000.

[7] C. O. Lee, C. C. Shin, I. M. Park, and S. T. Kim, "2-D PBG structures with improved ripple characteristic in passband and wideband band-stop filter design," *2002 Asia-Pacific Microwave Conf.*.

[8] N. C. Karmakar, M. N. Mollah, and S. K. Padhi, "Improved performance of a non-uniform ring patterned PBG assisted microstrip line," *IEEE APS Symp.,* vol. 2, pp. 848-851, 2002.

[9] F. R. Yang, K. P. Ma, Y. Qian, and T. Itoh, "A uniplanar compact photonic-bandgap (UC-PBG) structure and its applications for microwave circuits," *IEEE Trans. Microwave Theory Tech.,* vol. 47, pp. 1509-1514, Aug. 1999.

[10] C. Caloz, C. C. Chang, and T. Itoh, "A novel multilayer super-compact inharmonic photonic band-gap (PBG) structure for microstrip applications," *2001 Asia-Pacific Microwave Conf.,* vol. 2, pp. 651-654, 2001.

[11] D. Ahn, J. S. Park, C. S. Kim, J. Kim, Y. Qian, and T. Itoh, "A design of the low-pass filter using the novel microstrip defected ground structure," *IEEE Trans. Microwave Theory Tech.,* vol. 49, pp. 86-93, Jan. 2001.

[12] J. I. Park, C. S. Kim, J. Kim, J. S. Park, Y. Qian, D. Ahn, and T. Itoh, "Modeling of a photonic bandgap and its application for the low-pass filter design," *1999 Asia-Pacific Microwave Conf.,* vol. 2, pp. 331-334, Nov. 1999.

[13] J. S. Park, J. S. Yun, and D. Ahn, "A design of the novel coupled-line bandpass filter using defected ground structure with wide stopband performance," *IEEE Trans. Microwave Theory Tech.,* vol. 50, pp. 2037-2043, Sept. 2002.

[14] V. Radisic, Y. Qian, and T. Itoh, "Broad-band power amplifier using dielectric photonic bandgap structure," *IEEE Microwave Guided Wave Lett.,* vol. 8, pp. 13-14, Jan. 1998.

[15] C. S. Kim, J. S. Park, D. Ahn, and J. B. Lim, "A novel 1-D periodic defected ground structure for planar circuits," *IEEE Microwave Guided Wave Lett.,* vol. 10, pp. 131-133, Apr. 2000.

[16] H. B. Zhu and K. Wu, "Broadband and compact multi-pole microstrip bandpass filters using ground plane aperture technique," *IEE Proc. Microwave Antennas Propagat.,* vol. 149, pp. 71-77, Feb. 2002.

[17] H. S. Song, K. H. Park, and J. K. Kim, "New compact microstrip slow-wave resonator filter with a wide upper stopband," *2002 Asia-Pacific Microwave Conf.*.

[18] Q. Xue, K. M. Shum, and C. H. Chan, "Novel 1-D microstrip PBG cells," *IEEE Microwave Guided Wave Lett.,* vol. 10, pp. 403-405, Oct. 2000.

[19] A. Giorgio, A. G. Perri, and M. N. Armenise, "Very fast and accurate modeling of multilayer waveguiding photonic bandgap structures," *Lightwave Technology,* vol. 19, pp. 1598-1613, Oct. 2001.

[20] W. Kim and B. Lee, "Modelling and design of 2D UC-PBG structure using transmission line theory," *IEEE APS Symp.,* vol. 3, pp. 780-783, 2002.

[21] S. Lee, J. M. Kim, J.-M. Kim, Y. K. Kim, and Y. Kwon, "Millimeter-wave MEMS tunable low pass filter with reconfigurable series inductors and capacitive shunt switches," *IEEE Microwave and Wireless Component Lett.,* vol. 15, pp. 691-693, Oct. 2005.

[22] J. H. Park, S. Lee, J. M. Kim, H. T. Kim, Y. Kwon, and Y. K. Kim, "Reconfigurable millimeter-wave filters using CPW-based periodic structures with novel multiple-contact MEMS switches," *Jounal of Microelectromechanical Systems,* vol. 14, pp. 456-463, June 2005.

[23] D. Peroulis, S. Pacheco, K. Sarabandi, and L. P. B. Katehi, "Tunable lumped components with applications to reconfigurable MEMS filters," *IEEE MTT-S. Microwave Symp. Dig.,* pp. 341-344, May 2001.

[24] A. Tombak, J. P. Maria, F. T. Ayguavives, Z. Jin, G. T. Stauf, A. I. Kingon, and A. Mortazawi, "Voltage-controlled RF filters employing thin-film barium-strontium-titanate tunable capacitors," *IEEE Trans. Microwave Theory Tech.,* vol. 51, pp. 462-467, Feb. 2003.

[25] Y. Konoshi, "Novel dielectric waveguide components-microwave applications of new ceramic materials," *Proc. IEEE,* vol. 79, pp. 726-740, June 1991.

[26] S. J. Fiedziuszko, I. C. Hunter, T. Itoh, Y. Kobayashi, T. Nishikawa, S. N. Stitzer, and K. Wakino, "Dielectric materials, devices, and circuits," *IEEE Trans. Microwave Theory Tech.,* vol. 50, pp. 706-720, Mar. 2002.

[27] D. L. Rebsch, D. C. Webb, R. A. Moore, and J. D. Cowlishaw, "A mode chart for accurate design of cylindrical dielectric resonators," *IEEE Trans. Microwave Theory Tech.,* vol. MTT-13, pp. 468-469, May 1965.

[28] W. E. Courtney, "Analysis and evaluation of a method of measuring the complex permittivity and permeability of microwave insulators," *IEEE Trans. Microwave Theory Tech.,* vol. MTT-18, pp. 476-485, Aug. 1970.

[29] Y. Kobayashi and S. Tanaka, "Resonant modes of a dielectric rod resonator short-circuited at both ends by parallel conducting plates," *IEEE Trans. Microwave Theory Tech.,* vol. MTT-28, pp. 1077-1085, Oct. 1980.

[30] K. A. Zaki and A. E. Atia, "Modes in dielectric-loaded waveguides and resonators," *IEEE Trans. Microwave Theory Tech.,* vol. MTT-31, pp. 1039-1045, Dec. 1983.

[31] K. A. Zaki and C. Chen, "New results in dielectric-loaded resonators," *IEEE Trans. Microwave Theory Tech.,* vol. MTT-34, pp. 815-824, July 1986.

[32] S. B. Cohn, "Microwave bandpass filters containing high Q dielectric resonators," *IEEE Trans. Microwave Theory Tech.,* vol. MTT-16, pp. 218-227, Apr. 1968.

[33] K. Wakino, T. Nishikawa, S. Tamura, and Y. Ishikawa, "Microwave bandpass filters containing dielectric resonator with improved temperature stability and spurious response," *IEEE MTT-S. Microwave Symp. Dig.,* vol. 75, pp. 63-65, May 1975.

[34] Y. Kobayashi and M. Minegishi, "A bandpass filter using electrically coupled TM_{01} dielectric rod resonators," *IEEE MTT-S. Microwave Symp. Dig.,* vol. 1, pp. 507-510, May 1988.

[35] S. J. Fiedziuszko, "Dual-mode dielectric resonator loaded cavity filters," *IEEE Trans. Microwave Theory Tech.,* vol. MTT-30, pp. 1311-1316, Sept. 1982.

[36] K. A. Zaki, C. Chen, and A. E. Atia, "Canonical and longitudinal dual-mode dielectric resonator filters," *IEEE Trans. Microwave Theory Tech.,* vol. MTT-35, pp. 1130-1134, Dec. 1987.

[37] Y. Kobayashi and K. Kubo, "Canonical bandpass filters using dual-mode dielectric resonators," *IEEE MTT-S. Microwave Symp. Dig.,* vol. 87, pp. 137-140, June 1987.

[38] J. P. Astier and P. Guillon, "Elliptic microwave filter using dual modes of dielectric resonators," *European Microwave Conf. Dig.,* pp. 335-340, Sept. 1985.

[39] J. Hattori, T. Wada, K. Kubo, and Y. Ishikawa, "2GHz band quadruple mode dielectric resonator filter for cellular base station," *IEEE MTT-S. Microwave Symp. Dig.,* vol. 2, pp. 933-936, June 2003.

[40] C. Wang, H. W. Yao, K. A. Zaki, and R. R. Mansour, "Mixed modes cylindrical planar dielectric resonator filters with rectangular enclosure," *IEEE Trans. Microwave Theory Tech.,* vol. 43, pp. 2817-2523, Dec. 1995.

[41] C. Wang, K. A. Zaki, and A. E. Atia, "Dual-mode conductor-loaded cavity filters," *IEEE Trans. Microwave Theory Tech.,* vol. 45, pp. 1240-1246, Aug. 1997.

[42] C. Wang, K. A. Zaki, and A. E. Atia, "Dual mode combined dielectric and conductor loaded cavity filters," *IEEE MTT-S. Microwave Symp. Dig.,* vol. 2, pp. 1103-1106, June 1997.

[43] C. Wang, K. A. Zaki, and A. E. Atia, "Conductor loaded resonator filters with wide spurious-free stopbands," *IEEE Trans. Microwave Theory Tech.,* vol. 45, pp. 2387-2392, Dec. 1997.

[44] I. C. Hunter, J. D. Rhodes, and V. Dassonville, "Dual-mode filters with conductor-loaded dielectric resonators," *IEEE Trans. Microwave Theory Tech.,* vol. 47, pp. 2304-2311, Dec. 1999.

[45] Y. Ishikawa, T. Hiratsuka, T. Sonoda, and S. Mikami, "V band planar type dielectric resonator filter fabricated in ceramic substrate," *1997 Topical Symp. on Millimeter Waves,* pp. 93-96, Jul. 1997.

[46] T. Kimura, Y. Kobayashi, N. Ohkoumyou, T. Nishikawa, T. Tamura, and T. Itoh, "Diplexer of earth station for the marine satellite communication systems," *J. Inst. Electron. Inf. Commun. Eng.,* vol. 96, p. 55, Nov. 1977.

[47] W. C. Tang, J. Sferrazza, B. Beggs, and D. Siu, "Dielectric resonator output multiplexer for C-band satellite applications," *IEEE MTT-S. Microwave Symp. Dig.,* vol. 85, pp. 343-345, June 1985.

[48] S. J. Fiedziuszko, J. A. Curtis, S. C. Holme, and R. S. Kwok, "Low loss multiplexers with planar dual mode HTS resonators," *IEEE Trans. Microwave Theory Tech.,* vol. 44, pp. 1248-1257, July 1996.

[49] I. Rumsey, M. Piket-May, and P. K. Kelly, "Photonic bandgap structures used as filters in microstrip circuits," *IEEE Microwave Guided Wave Lett.,* vol. 8, pp. 336-338, Oct. 1998.

[50] Agilent EEsof Momentum, version 2002.

[51] R. E. Collin, *Fundations for microwave engineering*: McGraw-Hill Book Company, New York, 1966.

[52] R. Sorrentino and T. Itoh, "Transverse resonance analysis of finline discontinuities," *IEEE Trans. Microwave Theory Tech.,* vol. 32, pp. 1633-1638, Dec. 1984.

[53] J. Bornemann, "A scattering-type transverse resonance technique for the calculation of (M)MIC transmission line characteristics," *IEEE Trans. Microwave Theory Tech.,* vol. 39, pp. 2083-2088, Dec. 1991.

[54] R. R. Mansour and R. H. Machphie, "A unified hybrid-mode analysis for planar transmission lines with multilayer isotropic/anisotropic substrates," *IEEE Trans. Microwave Theory Tech.,* vol. MTT-35, pp. 1382-1391, Dec. 1987.

[55] R. Safavi-Naini and R. H. Macphie, "Scattering at rectangular-to-rectangular waveguide junctions," *IEEE Trans. Microwave Theory Tech.,* vol. 30, pp. 2060-2063, Nov. 1982.

[56] R. R. Mansour and R. H. Macphie, "Scattering at an N-furcated parallel-plate waveguide junction," *IEEE Trans. Microwave Theory Tech.,* vol. 33, pp. 830-835, Sept. 1985.

[57] R. R. Mansour and R. H. Macphie, "An improved transmission matrix formulation of cascaded discontinuities and its application to E-plane circuits," *IEEE Trans. Microwave Theory Tech.,* vol. 34, pp. 1490-1498, Dec. 1986.

[58] Ansoft HFSS, version 8.5.

[59] C. O. Lee and C. C. Shin, "Optimized etched hole size for suppressing the periodicity in the frequency response in Photonic Bandgap microstrip structures," *IEEE MTT-S. Microwave Symp. Dig.,* vol. 3, pp. 1615-1618, June 2003.

[60] J. B. Knorr, "Slot-line transitions," *IEEE Trans. Microwave Theory Tech.,* vol. 22, pp. 548-554, May 1974.

[61] Y. H. Shu, J. A. Navarro, and K. Chang, "Electronically switchable and tunable coplanar waveguide-slotline band-pass filters," *IEEE Trans. Microwave Theory Tech.,* vol. 39, pp. 548-554, Mar. 1991.

[62] S. B. Cohn, "Slot-line field components," *IEEE Trans. Microwave Theory Tech.,* vol. 20, pp. 172-174, Feb. 1972.

[63] R. Garg and K. C. Gupta, "Expressions for wavelength and impedance of a slotline," *IEEE Trans. Microwave Theory Tech.,* vol. 24, p. 532, Aug. 1976.

[64] Y. M. M. Antar, Z. Fan, and A. Ittipiboon, "Analysis of an arbitrarily inclined slot on the ground plane of a microstrip line," *Electronics Lett.,* vol. 31, pp. 1966-1967, Nov. 1995.

[65] K. L. Wu, Map_Fit, version 2.1.

[66] C. C. Chang, C. Caloz, and T. Itoh, "Analysis of a compact slot resonator in the ground plane for microstrip structures," *2001 Asia-Pacific Microwave Conf.,* vol. 3, pp. 1100-1103, 2001.

[67] M. Fallah-Rad and L. Shafai, "Parametric study of PBG ground planes in microstrip transmission lines," *Antenna Technology Applied Electromagnetics Symp.,* pp. 156-159, Aug. 2002.

[68] J. S. G. Hong and M. J. Lancaster, *Microstrip Filters for RF/Microwave Applications,* John Wiley & Sons Inc., New York, 2001.

[69] D. M. Pozar, *Microwave Engineering,* John Wiley & Sons Inc., New York, 1998.

[70] I. C. Hunter and J. D. Rhodes, "Electronically tunable microwave bandpass filters," *IEEE Trans. Microwave Theory Tech.,* vol. MTT-30, pp. 1354-1360, Sept. 1982.

[71] M. Makimoto and M. Sagawa, "Varactor tuned bandpass filters using microstrip-line ring resonators," *IEEE MTT-S. Microwave Symp. Dig.,* vol. 86, pp. 411-414, June 1986.

[72] A. R. Brown and G. M. Rebeiz, "A varactor tuned RF filter," *IEEE Trans. Microwave Theory Tech.,* vol. 48, pp. 1157-1160, July 2000.

[73] K. Entesari and G. M. Rebeiz, "A 12-18-GHz three-pole RF MEMS tunable filter," *IEEE Trans. Microwave Theory Tech.,* vol. 53, pp. 2566-2571, Aug. 2005.

[74] X. P. Liang and Y. F. Zhu, "Hybrid resonator microstrip line electrically tunable filter," *IEEE MTT-S. Microwave Symp. Dig.,* vol. 3, pp. 1457-1460, May 2001.

[75] S. R. Chandler, I. C. Hunter, and J. G. Gardiner, "Active varactor tunable bandpass filter," *IEEE Microwave and Guided Wave Lett.,* vol. 3, pp. 70-71, Mar. 1993.

[76] E. Fourn, A. Pothier, C. Champeaux, P. Tristant, A. Catherinot, P. Blondy, G. Tanne, E. Rius, C. Person, and F. Huret, "MEMS switchable interdigital coplanar filter," *IEEE Trans. Microwave Theory Tech.,* vol. 51, pp. 320-324, Jan. 2003.

[77] D. Mercier, J. C. Orlianges, T. Delage, C. Champeaux, A. Catherinot, D. Cros, and P. Blondy, "Millimeter-wave tune-all bandpass filters," *IEEE Trans. Microwave Theory Tech.,* vol. 52, pp. 1175-1181, Apr. 2004.

[78] H. T. Kim, J. H. Park, Y. K. Kim, and Y. Kwon, "Low-loss and compact V-band MEMS-based analog tunable bandpass filters," *IEEE Microwave and Wireless Component Lett.,* vol. 12, pp. 432-434, Nov. 2002.

[79] A. Abbaspour-Tamijani, L. Dussopt, and G. M. Rebeiz, "Miniature and tunable filters using MEMS capacitors," *IEEE Trans. Microwave Theory Tech.,* vol. 51, pp. 1878-1885, July 2003.

[80] R. Zhang and R. R. Mansour, "A novel lowpass microstrip filter using metal-loaded slots in the ground plane," *IEEE MTT-S. Microwave Symp. Dig.,* pp. 1311-1314, June 2004.

[81] R. Zhang and R. R. Mansour, "Novel digital and analogue tunable lowpass filters," *IEE Proc. Microwave Antennas Propagat.,* accepted, 2007.

[82] R. Zhang and R. R. Mansour, "Novel tunable lowpass filters using folded slots etched in the ground plane," *IEEE MTT-S. Microwave Symp. Dig.,* pp. 775-778, June 2005.

[83] Radant MEMS, http://www.radantmems.com.

[84] http://www.ece.gatech.edu/research/labs/vc/theory/sheetRes.html.

[85] MDT, http://www.mdtcorp.com.

[86] I. C. Hunter, L. Billonet, B. Jarry, and P. Guillon, "Microwave filters-applications and technology," *IEEE Trans. Microwave Theory Tech.,* vol. 50, pp. 794-805, Mar. 2002.

[87] K. Wakino, T. Nishikawa, and Y. Ishikawa, "Miniaturization technologies of dielectric resonator filters for mobile communications," *IEEE Trans. Microwave Theory Tech.,* vol. 42, pp. 1295-1300, July 1994.

[88] R. R. Mansour, "Filter technologies for wireless base stations," *IEEE Microwave Magazine,* pp. 68-74, Mar. 2004.

[89] R. Vahldieck, "Design and development of high-Q microwave filters-past, present and future," *IEEE Africon,* vol. 2, pp. 1099-1104, Sept. 1999.

[90] R. Zhang and R. R. Mansour, "Dielectric resonator filters fabricated from high-K ceramic substrates," *IEEE MTT-S. Microwave Symp. Dig.,* pp. 234-237, June 2006.

[91] R. Zhang and R. R. Mansour, "Dielectric resonator filters fabricated from high-K ceramic substrates with improved spurious performance," *IEEE Trans. Microwave Theory Tech.,* submitted, Feb. 2007.

[92] Trans-Tech, http://www.trans-techinc.com.

[93] S. Hong and K. Chang, "Stub-tuned microstrip bandpass filters for millimeter-wave diplexer design," *IEEE Microwave and Wireless Components Lett.,* vol. 15, pp. 582-584, Sept. 2005.

[94] H. Liu, T. Yoshimasu, S. Kurachi, and J. Chen, "A novel microstrip diplexer design using defected ground structure," *2005 International Conference on Communications, Circuits and Systems,* vol. 2, pp. 1099-1100, May 2005.

[95] G. Tudosie, E. Ofli, and R. Vahldieck, "Hybrid EM-simulator based optimization of microwave and millimeter wave diplexers and multiplexers," *IEEE MTT-S. Microwave Symp. Dig.,* vol. 2, pp. 1219-1222, June 2003.

[96] J. R. Montejo-Garai, J. A. Ruiz-Cruz, and J. M. Rebollar, "Full-wave design of H-plane contiguous manifold output multiplexers using the fictitious reactive load concept," *IEEE Trans. Microwave Theory Tech.,* vol. 53, pp. 2628-2632, Aug. 2005.

[97] A. A. Kirilenko, S. L. Senkevich, V. I. Tkachenko, and B. G. Tysik, "Waveguide diplexer and multiplexer design," *IEEE Trans. Microwave Theory Tech.,* vol. 42, pp. 1393-1396, July 1994.

[98] F. M. Vanin, D. Schmitt, and R. Levy, "Dimensional synthesis for wide-band waveguide filters and diplexers," *IEEE Trans. Microwave Theory Tech.,* vol. 43, pp. 2817-2823, Dec. 1995.

[99] A. Morini, T. Rozzi, M. Farina, and G. Venanzoni, "A new look at the practical design of compact diplexers," *IEEE Trans. Microwave Theory Tech.,* vol. 54, pp. 3515-3520, Sept. 2006.

[100] M. A. Ismail, D. Smith, A. Panariello, Y. Wang, and M. Yu, "EM-based design of large-scale dielectric-resonator filters and multiplexers by space mapping," *IEEE Trans. Microwave Theory Tech.,* vol. 52, pp. 386-392, Jan. 2004.

[101] R. R. Mansour and R. Zhang, "Dielectric resonator filter assemblies and methods," US patent and European patent filed, Dec. 2006.